U.S. DEPARTMENT OF COMMERCE
National Technical Information Service

PB-257 164

# Spectroscopic Studies of Photochemical Smog Formation and Trace Pollutant Detection

Ohio State University Research Foundation

Prepared for

Environmental Sciences Research Lab, Research Triangle Park, N C

Jul 76

**TECHNICAL REPORT DATA**
*(Please read Instructions on the reverse before completing)*

| 1. REPORT NO. | 2. | 3. RECIPIENT'S ACCESSION NO. |
|---|---|---|
| EPA-600/3-76-084 | | |

| 4. TITLE AND SUBTITLE | 5. REPORT DATE |
|---|---|
| SPECTROSCOPIC STUDIES OF PHOTOCHEMICAL SMOG FORMATION AND TRACE POLLUTANT DETECTION | July 1976 |
| | 6. PERFORMING ORGANIZATION CODE |
| 7. AUTHOR(S) | 8. PERFORMING ORGANIZATION REPORT NO. |
| Jack G. Calvert, Walter H. Chan, Robert J. Nordstrom, and John H. Shaw | |
| 9. PERFORMING ORGANIZATION NAME AND ADDRESS | 10. PROGRAM ELEMENT NO. |
| The Ohio State University Research Foundation<br>1314 Kinnear Rd.<br>Columbus, Ohio 43212 | 1AA008 |
| | 11. CONTRACT/GRANT NO. |
| | R-803075 |
| 12. SPONSORING AGENCY NAME AND ADDRESS | 13. TYPE OF REPORT AND PERIOD COVERED |
| Environmental Sciences Research Laboratory<br>Office of Research and Development<br>U.S. Environmental Protection Agency<br>Research Triangle Park, North Carolina 27711 | Final 74/75 |
| | 14. SPONSORING AGENCY CODE |
| | EPA-ORD |

15. SUPPLEMENTARY NOTES

16. ABSTRACT

An infrared Fourier transform spectrometer has been used with a long path length, multiple traversal cell to study the infrared spectra of atmospheric gases and several pollutant gases. Solar spectra have also been obtained between 3 and 20 μm wavelength.

The kinetics of the formation and decay of nitrous acid have been followed by monitoring bands of nitric oxide, nitrogen dioxide, and both cis- and trans-nitrous acid. Rate constants and the equilibrium constant for the reactions have been derived. A mechanism accounting for the formation of nitrous acid in the atmosphere is proposed. These rate data have been used to speculate on the potential importance of nitrous acid formation in power plant and auto exhaust plumes.

A new technique involving the use of infrared spectroscopy and two cells of unequal length to study a two-component system in equilibrium is described.

A six-meter multiple traversal cell equipped with fluorescent tubes has been constructed. The cell irradiance closely simulates the solar irradiance at ground level in spectral distribution and intensity.

17. KEY WORDS AND DOCUMENT ANALYSIS

| a. DESCRIPTORS | b. IDENTIFIERS/OPEN ENDED TERMS | c. COSATI Field/Group |
|---|---|---|
| * Air pollution<br>* Infrared spectroscopy<br>* Optical equipment<br>Solar spectrum<br>* Nitrous acid<br>* Reaction kinetics<br>* Photochemical reactions | Fourier Transform Spectrometer | 13B<br>14B<br>20F<br>03B<br>07B<br>07D<br>07E |

| 18. DISTRIBUTION STATEMENT | 19. SECURITY CLASS *(This Report)* | 21. NO. OF PAGES |
|---|---|---|
| RELEASE TO PUBLIC | UNCLASSIFIED | 99 |
| | 20. SECURITY CLASS *(This page)* | 22. PRICE |
| | UNCLASSIFIED | 5.00 |

EPA Form 2220-1 (9-73)

PRICES SUBJECT TO CHANGE

252181

PB 257 164

EPA-600/3-76-084
July 1976

Ecological Research Series

REPRODUCED BY
NATIONAL TECHNICAL
INFORMATION SERVICE
U.S. DEPARTMENT OF COMMERCE
SPRINGFIELD, VA. 22161

## RESEARCH REPORTING SERIES

Research reports of the Office of Research and Development, U.S. Environmental Protection Agency, have been grouped into five series. These five broad categories were established to facilitate further development and application of environmental technology. Elimination of traditional grouping was consciously planned to foster technology transfer and a maximum interface in related fields. The five series are:

1. Environmental Health Effects Research
2. Environmental Protection Technology
3. Ecological Research
4. Environmental Monitoring
5. Socioeconomic Environmental Studies

This report has been assigned to the ECOLOGICAL RESEARCH series. This series describes research on the effects of pollution on humans, plant and animal species, and materials. Problems are assessed for their long- and short-term influences. Investigations include formation, transport, and pathway studies to determine the fate of pollutants and their effects. This work provides the technical basis for setting standards to minimize undesirable changes in living organisms in the aquatic, terrestrial, and atmospheric environments.

This document is available to the public through the National Technical Information Service, Springfield, Virginia 22161.

EPA-600/3-76-084
July 1976

# SPECTROSCOPIC STUDIES OF PHOTOCHEMICAL SMOG FORMATION AND TRACE POLLUTANT DETECTION

by

Jack G. Calvert
Walter H. Chan
Robert J. Nordstrom
John H. Shaw
The Ohio State University
Research Foundation
Columbus, Ohio 43212

Grant No. R-803075
ROAP No. 21AKC
Task 31
Program Element No. 1AA008

Project Officer
Philip Hanst
Atmospheric Chemistry and Physics Division
Environmental Sciences Research Laboratory
Research Triangle Park, North Carolina 27711

U.S. ENVIRONMENTAL PROTECTION AGENCY
OFFICE OF RESEARCH AND DEVELOPMENT
ENVIRONMENTAL SCIENCES RESEARCH LABORATORY
RESEARCH TRIANGLE PARK, NORTH CAROLINA 27711

ia

## DISCLAIMER

This report has been reviewed by the Environmental Sciences Research Laboratory, U.S. Environmental Protection Agency, and approved for publication. Approval does not signify that the contents necessarily reflect the views and policies of the U.S. Environmental Protection Agency, nor does mention of trade names or commercial products constitute endorsement or recommendation for use.

## ABSTRACT

An infrared Fourier transform spectrometer has been used with a long path length multiple traversal cell to study the infrared spectra of atmospheric gases and several pollutant gases. Solar spectra have also been obtained between 3 and 20 μm wavelength.

The kinetics of the formation and decay of nitrous acid have been followed by monitoring bands of nitric oxide, nitrogen dioxide, and both cis- and trans-nitrous acid. Rate constants and the equilibrium constant for the reactions have been derived. A mechanism accounting for the formation of nitrous acid in the atmosphere is proposed. These rate data have been used to speculate on the potential importance of nitrous acid formation in power plant and auto exhaust plumes.

A new technique involving the use of infrared spectroscopy and two cells of unequal length to study a two-component system in equilibrium is described.

A six-meter multiple traversal cell in which path lengths of up to 700 m can be obtained has been constructed. The cell is surrounded with fluorescent tubes with output in the region from 300 to 400 nm. The cell irradiance closely simulates the solar irradiance at ground level in spectral distribution and intensity.

CONTENTS


| | | |
|---|---|---|
| | ABSTRACT | iii |
| | FIGURES | vii |
| | TABLES | x |
| I | SUMMARY AND CONCLUSIONS | 1 |
| II | BACKGROUND AND INTRODUCTION | 3 |
| III | INSTRUMENTATION AND EXPERIMENTAL PROCEDURES | 5 |
| | A. Instrumentation | 5 |
| | 1. Introduction | 5 |
| | 2. Twenty-One Meter Stainless Steel Absorption Cell | 5 |
| | 3. Optical System | 7 |
| | 4. Six Meter Glass Cell | 10 |
| | 5. Fourier Transform Spectrometer and Transfer Optics | 23 |
| | 6. Coelostat | 28 |
| | 7. Gas Handling System | 28 |
| | B. Experimental Procedures | 31 |
| | 1. Spectroscopic Studies of Chemical Reactions | 31 |
| | 2. Calibration of NO and $NO_2$ Gases and HONO | 33 |
| | 3. Preparation of Nitrous Acid | 35 |
| | 4. Study of $HNO_2$ Decay 38 | |
| | 5. Study of $HNO_2$ Formation | 38 |
| IV | RESULTS AND DISCUSSION | 39 |
| | A. Collection of Gas Spectra | 39 |
| | B. Study of the $NO_2$ - $N_2O_4$ System | 41 |
| | 1. Introduction | 41 |
| | 2. Experimental | 42 |
| | 3. Theory | 44 |
| | 4. Results | 45 |
| | 5. Conclusions | 47 |
| | C. Study of the Kinetics and the Mechanism of the Reactions in the Gaseous System, HONO, NO, $NO_2$, $H_2O$ | 51 |
| | 1. Introduction | 51 |
| | 2. Experimental Methods and Techniques | 55 |
| | 3. Experimental Results and Discussion | 60 |
| REFERENCES | | 77 |

CONTENTS - (Continued)


| | | |
|---|---|---|
| APPENDIX A. | OPTICAL ALIGNMENT PROCEDURES | 79 |
| | Twenty-One Meter Absorption Cell | 79 |
| | Six Meter Cell | 79 |
| | Transfer System from the Interferometer to the Absorption Cell | 79 |
| | Interferometer and Source Optics | 80 |
| APPENDIX B. | FOURIER TRANSFORM SPECTROMETER | 81 |
| | Description of Operation | 81 |
| | Undersampling to Obtain High Resolution | 81 |
| APPENDIX C. | UNITS FOR MEASURING GAS CONCENTRATIONS | 87 |

FIGURES


| Number | | Page |
|---|---|---|
| 1 | Optical arrangement of the 21 m cell, (a) optical paths; (b) mirror shape | 6 |
| 2 | Image pattern on the field mirror $M_F$ | 8 |
| 3 | Six-meter glass cell construction details. Stainless steel spacers separate the tube and stainless steel end plates, E, are shown | 11 |
| 4 | Support system for 6 m cell | 12 |
| 5 | Cradle supports for 6 m cell | 13 |
| 6 | Gas inlet system to 6 m cell | 14 |
| 7 | Support system for fluorescent lamps around 6 m cell | 15 |
| 8 | (a) Fluorescent lamps arrangement for 6 m cell; (b) Wiring diagram for lamps. The ballasts $A_1$, $A_2$, $A_3$ and $A_4$ supply power for the lamps in Bank A of Fig. 8a. Switch $S_1$ controls the power to the lamps as shown in Fig. 8c | 17 |
| 9 | Reflector supports for 6 m cell | 18 |
| 10 | (a) Spectral distribution of fluorescent lamp output; (b) Spectral distribution of fluorescent lamp output after passing through glass walls of cell; (c) Relative spectral distribution of solar energy at ground level | 19 |
| 11 | Spectral transmittance of glass tubes of 6 m cell | 20 |
| 12 | Mirror system for 6 m cell. The numbers refer to consecutive reflections by the mirrors. The number of traversals is altered by turning $D_4$ | 21 |
| 13 | Optical diagram of interferometer | 24 |
| 14 | Optical transfer system from interferometer to absorption cell | 26 |
| 15 | Optical transfer system from absorption cell to InSb detector | 27 |
| 16 | Gas handling system | 29 |

FIGURES - (Continued)


| Number | | Page |
|---|---|---|
| 17 | Spectral ratioing, (a) Spectrum of detector profile and evacuated cell; (b) Spectrum with sample of $NO_2$ and $N_2O_4$ in cell; (c) Ratio of spectrum (b)/ spectrum (a). Spectral resolution 0.5 $cm^{-1}$ | 32 |
| 18 | Dependence of absorbance of NO Q-branch (1876 $cm^{-1}$) on the path length x NO concentration product. Total pressure 700 mmHg. Spectral resolution, 0.5 $cm^{-1}$ | 34 |
| 19 | Dependence of the absorbance of $NO_2$ Q-branch (823 $cm^{-1}$) on the path length x $NO_2$ concentration product. Total pressure 700 mmHg. Spectral resolution, 0.5 $cm^{-1}$. Temperature 23 $\pm$ 1°C | 36 |
| 20 | Apparatus for preparation of $HNO_2$ | 37 |
| 21 | (a) Spectrum of approximately 10 m of air at ambient pressure and temperature, spectral resolution 0.125 $cm^{-1}$; (b) Spectrum of approximately 100 m of air; (c) Spectrum of approximately 1000 m of air; (d) Solar spectrum, solar zenith angle ~ 60° | 40 |
| 22 | The experimental apparatus. Either of the two absorption cells can be aligned at the indicated position | 43 |
| 23 | Spectrum of $NO_2$ + $N_2O_4$ from 700 $cm^{-1}$ to 900 $cm^{-1}$, See text for experimental details | 46 |
| 24 | Plots of absorbance of 791 $cm^{-1}$ Q-branch of $NO_2$ as a function of total sample gas pressure in each absorption cell | 48 |
| 25 | Plot of absorbance of 791 $cm^{-1}$ Q-branch of $NO_2$ as a function of partial pressure of $NO_2$ times path length. The squares represent data taken through the 39.5 cm cell | 50 |
| 26 | Absorption spectrum of reacting mixture of HONO, NO, $NO_2$, and $H_2O$; note in (a) decrease in the $\nu_4$ bands of trans-HONO (791 $cm^{-1}$) and cis-HONO (853 $cm^{-1}$) and buildup of $NO_2$ transitions as time progresses in an originally HONO-rich mixture; note in (b) the growth of HONO peaks as time progresses in an originally HONO-poor mixture | 58-59 |

FIGURES - (Continued)


| Number | | Page |
|---|---|---|
| 27 | Absorbance versus time plot for the trans-HONO (1264 $cm^{-1}$) and cis-HONO (853 $cm^{-1}$) in a HONO-NO-$NO_2$-$H_2O$ mixture originally rich in HONO | 61 |
| 28 | Plot of the reciprocal of the absorbance of trans-HONO (1264 $cm^{-1}$) and cis-HONO (853 $cm^{-1}$) versus time for a HONO-NO-$NO_2$-$H_2O$ mixture originally rich in HONO | 62 |
| 29 | Plot of total HONO concentration versus time for an extended run of 1648 min duration using an initially HONO-rich mixture; initial concentrations, ppm: HONO, 2.14; NO, 2.37; $NO_2$, 3.53; $H_2O$, 4200; temperature, 23°C. Curves shown have been calculated relation 48 and the rate constant values indicated on the figure. | 64 |
| 30 | Plot of cis-HONO concentration versus time using an initially HONO-poor mixture; initial concentrations, ppm: HONO, 0.141; NO, 10.6; $NO_2$, 9.72; $H_2O$, 2240; temperature, 23°C. Curves shown have been calculated using relation 48 and the rate constant values indicated on the figure. | 68 |
| 31 | Plot of [HONO] and temperature within the reaction cell versus time for an HONO-NO-$NO_2$-$H_2O$ mixture near equilibrium; typical data used to determine the equilibrium constant for the reaction, NO + $NO_2$ + $H_2O$ = 2HONO, and to provide a qualitative test of the temperature dependence to the rate constants. | 71 |
| 32 | Plot of $\ln K(atm^{-1})$ versus 1/T for literature data and present results for the equilibrium, NO + $NO_2$ + $H_2O$ = 2HONO; open circles, Ashmore and Tyler[21]; square average of data of Wayne and Yost[15]; triangles, Waldorf and Babb[20]; closed circles, this work. JANAF suggested values are shown along with a squares fit of published data excluding present work | 73 |

TABLES


| Number | | Page |
|---|---|---|
| 1 | Data for Determination of the Equilibrium Constant for the $NO_2$ - $N_2O_4$ System | 48 |
| 2 | Summary of the Rate Constant Estimates for the Reactions | 66 |
| 3 | Equilibrium Data Derived from the Temperature Drift Experiments | 72 |
| 4 | Theoretical Development of HONO as a Function of Time for Mixtures of NO, $NO_2$, and $H_2O$ for Compositions Typical of Stack Gas Emissions and Ambient Conditions | 75 |
| 5 | IFTS Parameters to Achieve 0.125 $cm^{-1}$ Resolution | 84 |
| 6 | Characteristics of Optical Filters and Spectral Limits to Achieve 0.125 $cm^{-1}$ Resolution | 85 |
| 7 | Relations Between Units for Amount of Absorbing Gas in a Given Path Length | 88 |

## SECTION I

## SUMMARY AND CONCLUSIONS

This study has shown that an infrared Fourier transform spectrometer (IFTS), when used to observe infrared spectra of gases in long path length, multiple traversal cells, can detect trace amounts of some gases at the ppb to ppm level. This instrumentation can be used to determine accurate information of the kinetics of chemical reactions involving concentrations of gas samples similar to those of their atmospheric abundances.

In addition to adapting an IFTS for use with the multiple traversal cell and also with a coelostat to observe solar spectra, a 6 m glass-walled cell, suitable for photochemical studies, has been constructed.

With these systems, spectra of air samples ranging in length from 10 m to 1 km have been obtained between 400 $cm^{-1}$ and 3500 $cm^{-1}$ together with solar spectra at several zenith distances. All of these spectra were obtained at 0.125 $cm^{-1}$ resolution. Most of the lines observed in these spectra can be identified with transitions of $H_2O$, $O_3$, $CO_2$, $N_2O$ and $CH_4$ in the AFCRL line listing.[1] A program for collecting high resolution spectra of the principal bands of pure samples of the permanent atmospheric gases and of known and suspected pollutant gases has been initiated.

Among the advantages of the IFTS system over the more conventional grating spectrometers is its ability to acquire high resolution spectral information over wide spectral intervals in short time intervals. Since the information is generated in digital form it is suitable for storage on magnetic tape and for further computer processing. Thus, the spectra can be ratioed to remove spectral variations in detector sensitivity and source radiance, and absorption bands of other molecular species can be removed. The system has been shown to be stable, linear in output, and to give highly reproducible spectra, essential requirements for quantitative analysis of gas concentrations.

The IFTS system has been used to determine the equilibrium constant of the reaction

$$N_2O_4 \rightleftharpoons 2NO_2$$

A value of 0.14 ± 0.02 atm was obtained.

The system has also been used to measure the extinction coefficients of bands of NO, $NO_2$, and cis- and trans-HONO and to make a detailed study of the kinetics, equilibrium constant, and the temperature dependence of the thermal reactions.

$$H_2O + NO + NO_2 \overset{k_1}{\rightleftharpoons} 2HONO \quad (1)$$

$$2HONO \overset{k_2}{\rightarrow} H_2O + NO + NO_2 \quad (2)$$

Using infrared spectroscopy, it is possible to observe cis-HONO and trans-HONO separately. We have found that the kinetics of the decay (second order in nitrous acid) are the same for both isomers. This result supports the fact that

$$\text{cis-HONO} \approx \text{trans-HONO}$$

proceeds much faster than either reactions in Eqs. (1) and (2)

The rate $k_2$ in Eq. (2) has been determined to be $k_2 = 1.4 \pm 0.4 \times 10^{-3}$ $ppm^{-1}min^{-1}$ at 23°C. This rate is strongly temperature dependent. A value of $2.2 \pm 0.7 \times 10^{-9}$ $ppm^{-2}min^{-1}$ was obtained for rate constant $k_1$.

Based on estimates of the typical concentrations of NO, $NO_2$ and $H_2O$ in car exhausts and the effluent from electrical generator stacks wher. fossil fuels are consumed, the measured reaction rates, and typical values for the rate of dilution and cooling of these emissions as they enter the atmosphere, it is estimated that there is sufficient HONO present in urban atmospheres during the early morning hours to be an important source of the OH radical.

## SECTION II

## BACKGROUND AND INTRODUCTION

The concentrations of gaseous pollutants in the free atmosphere are typically in the range $10^{-6}$ to $10^{-12}$ by volume. Even at these low concentrations many pollutants affect the environment and the air quality. They can also undergo reactions with other atmospheric molecular species to form new products. Many of these reactions which occur at ground level are initiated by solar radiation at wavelengths between 300 and 500 nm.

To understand the nature of these reactions and to determine which are of importance to air pollution, it is necessary to study gaseous systems which contain the reactants at concentrations which approximate those found in ambient air and which can be irradiated at levels corresponding to daytime solar radiant energy levels.

Although many techniques have been proposed for monitoring low levels of gases in gas samples and some have been useful in particular situations, infrared spectroscopic studies of long optical paths through the samples remain among the more specific, sensitive, and accurate methods for the detection of many molecular species.

The detectivity of infrared spectroscopic techniques increases with the path length and spectral resolution available. It may be decreased if there is interference caused by more than one constituent absorbing in the spectral region of interest.

The instrumentation available for the present study include a stainless steel multiple traversal absorption cell in which path lengths in excess of 1 km can be obtained. A glass-walled cell has also been constructed in which path lengths in excess of 500 m are possible. The cell can be irradiated to give an irradiance which is similar in spectral distribution and magnitude to ground level solar radiant energy between 300 and 400 nm.

The length of time required to collect an infrared spectrum typically increases as the power of the incoming signal decreases, as the spectral resolution is increased and as the width of the spectral interval surveyed increases. The slow response typical of other types of infrared systems has been largely overcome by IFTS, which can collect spectral information over wide spectral regions in relatively short times. The system in use has obtained a solar spectrum of the region from 2400 to 3500 $cm^{-1}$ with a spectral resolution of 0.125 $cm^{-1}$ in less than 2 minutes. This rapid collective speed allows chemical reactions to be monitored rapidly so that rate constants can be determined.

From a large number of possible reactions which could be studied we have chosen to investigate the reaction between $H_2O$, NO, and $NO_2$ which

leads to the formation of HONO. The presence of this transient species in the atmosphere has been suggested although it has not so far been observed. The present investigation has shown that this molecule will not only be formed in power plant plumes and in car exhausts, but that it may exist in the ambient atmosphere under suitable conditions.

## SECTION III

## INSTRUMENTATION AND EXPERIMENTAL PROCEDURES

### A. INSTRUMENTATION

#### 1. Introduction

One of the objectives of this study was to investigate the application of infrared Fourier transform spectrometers (IFTS) to air pollution problems. We have been concerned with the ability of such a spectrometer, used in conjunction with long path length absorption cells, to identify and monitor trace gases in the atmosphere and to study reactions among gases at concentrations in the ppm range by measuring their infrared bands. The intensities of the infrared bands of most gases are such that, if a gas is present in ppm quantities in air at atmospheric pressure, path lengths in the range of 100 m to 1 km are required for accurate measurement.

We have carried out investigations with a 21 m stainless steel cell already constructed. During the past year a 6 m glass cell suitable for photochemical studies has been built. The design of these cells and their adaptation for use with the IFTS are described.

#### 2. Twenty-one Meter Stainless Steel Absorption Cell

Most of the investigations made under this grant employed a 21 m stainless steel absorption cell containing a White multiple traversal optical arrangement.[2] With this system useful absorption measurements can be carried out with path lengths in excess of 1 km.

The cell body is a cylinder, 21 m long, with an internal diameter of 76 cm, made of 6 mm stainless steel, type 304. It is designed for a pressure range of 0 to 4 atm and for a temperature range of -60 to 250°C. The temperature control system has not yet been installed.

A diagram of the optical system is shown in Fig. 1. The mirrors, $D_1$ and $D_2$, were cut from 40 cm diameter blanks so that they could be placed side by side inside the cell. Their horizontal width is 33 cm. The field mirror, $M_F$, has the shape shown in Fig. 1.

The mounts for the mirrors are made from stainless steel and mechanical feedthroughs allow mirrors $D_1$ and $D_2$ to be adjusted from outside the cell. Thus, the number of traversals and the optical path in the cell can be altered without disturbing the gas sample. The cell is evacuated with a Kinney high vacuum booster pump, Series KMBD. Pump down time from atmospheric pressure to a few microns Hg is approximately one hour. Leakage rates of less than 1 mmHg/day are typically observed.

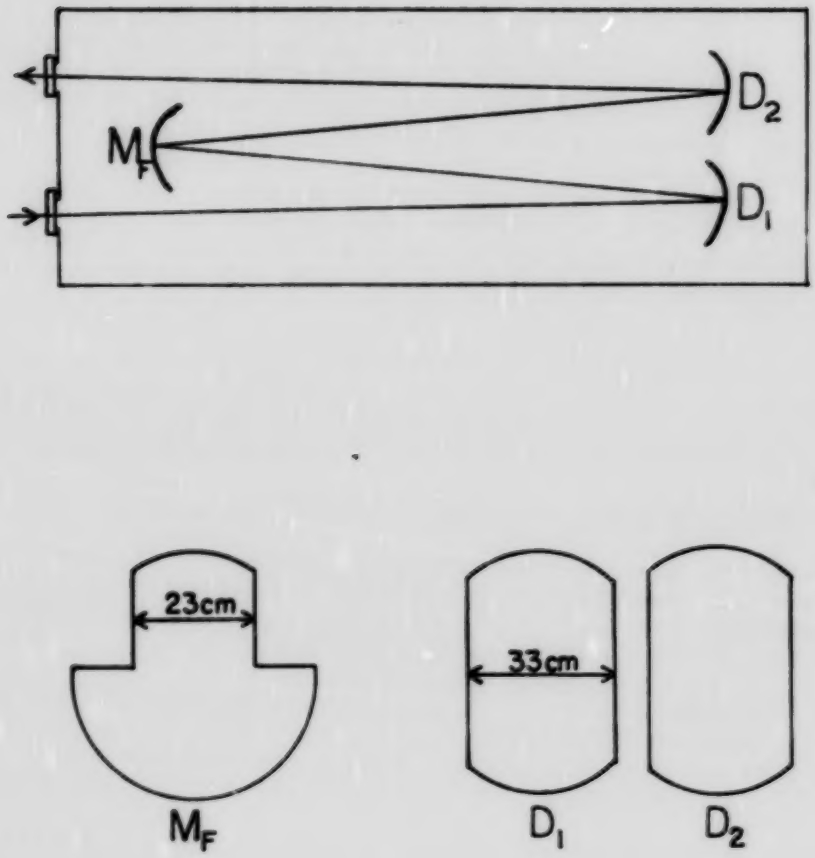


Figure 1. Optical arrangement of the 21 m cell, (a) optical paths; (b) mirror shape

## 3. Optical System

All of the three mirrors in Fig. 1 have the same radius of curvature (20.5 m) and are placed a distance apart of 20.5 m. Radiant energy enters the cell through a window near $M_F$ and forms an image of the source in the plane of $M_F$ close to one of its vertical edges. The energy is reflected by $D_1$ back to $M_F$ and from there to $D_2$. The number of traversals of the cell made by the radiant energy before it passes the opposite side of $M_F$ and leaves the cell is altered by adjusting the mirrors $D_1$ and $D_2$.

Two rows of images of the source are formed on $M_F$, as shown in Fig. 2, when the numbers identify successive images. As each image is formed, the radiant energy makes two additional traversals of the cell. The maximum number of images in the top row of images

$$N_{max} = \frac{D}{d} \tag{3}$$

where

$D$ = width of the upper half of $M_F$ (23 cm), and

$d$ = width of the entering beam in the plane of $M_F$.

The total number of images on $M_F$ is then $(2N_{max} + 1)$, and the corresponding number of traversals of the cell is $4N_{max}$. Thus the maximum path length

$$L_{max} = 4N_{max}R \tag{4}$$

where $R = 20.5$ m is the distance between the mirrors.

If $d = 10$ mm, then the maximum path length $L_{max}$ is approximately 1.9 km.

If the entering beam has a spectral radiance $B_\nu$ [$\nu$ = wavenumber ($cm^{-1}$)], forms an image of area $A_c$ of the source in the plane of $M_F$, and completely fills the mirror $D_1$ the spectral radiant power in the frequency interval $\nu$ to $\nu + d\nu$ leaving the cell is

$$P_\nu d\nu = B_\nu A_c \omega_c T_c d\nu \tag{5}$$

where

$\omega_c$ = solid angle subtended by $D_1$ at $M_F$, and

$T_c$ = transmission coefficient of the cell.

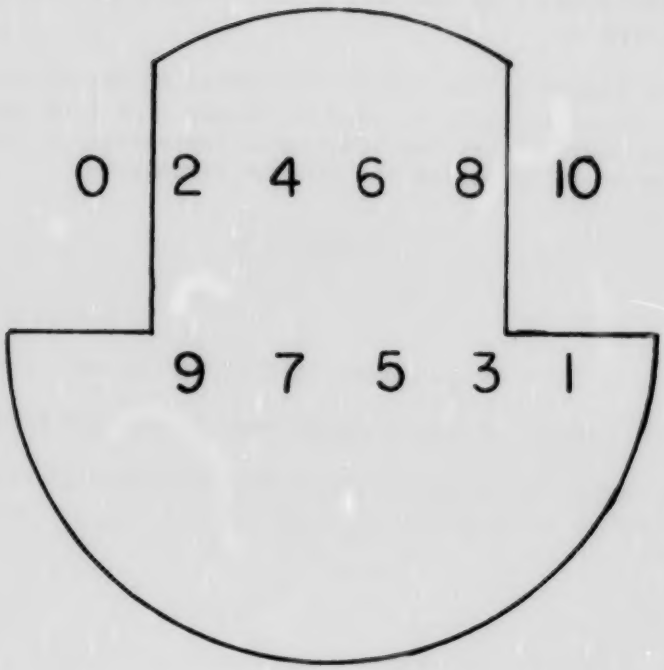


Figure 2. Image pattern on the field mirror $M_F$

The solid angle

$$\omega_c = \frac{A_{D_1}}{R^2} \tag{6}$$

where

$A_{D_1}$ = area of $D_1 \approx \pi r_{D_1}^2$,

$r_{D_1} \approx 17$ cm, and

R = distance between $M_F$ and $D_1$

= 20.5 m

Thus $\omega_c = 2.2 \times 10^{-4}$ sr. The shape of $M_F$, shown in Fig. 2, is well suited for use with a grating spectrometer. The narrow entrance and exit slits of such instruments are filled by forming an image of a line source such as a Nernst glower on them. An IFTS typically has a much larger "throughput" since there are no slits and radiant beams with circular symmetry are used. Thus, the area $A_c$ of the beam, matching an IFTS, in the plane of $M_F$ is typically given by

$$A_c = \pi r_b^2 \tag{7}$$

where $2r_b = d$, the diameter of the beam.

To obtain long path lengths (Eq. (4)) $2r_b \approx 10$ mm thus, $A_c \approx 0.79$ cm$^2$ and the product for this cell,

$$A_c\omega_c \approx 1.74 \times 10^{-4} \text{cm}^2\text{sr}. \tag{8}$$

The transmission coefficient $T_c$ in Eq. (5) depends on the reflection coefficient of the mirrors as well as on the absorption and scattering effects of the windows, aerosols, and gases in the optical path. More specifically, each traversal of the cell requires a reflection at a mirror. If the reflection coefficients, r, are the same for each mirror and the total number of traversals is n, the transmission coefficient due to the mirror reflectivity alone

$$T_m = r^n \tag{9}$$

The mirrors are gold coated and if $r = 0.98$, a reasonable value for the infrared, $T_m \approx 0.20$ for $n = 80$ and an optical path of 1.5 km. The observed value of $T_{cell}$ for $n = 80$ is smaller than this and is attributed to aberrations caused by the mirrors. Excellent spectra of path lengths of 1 km of air are obtained with the IFTS using this cell.

## 4. Six-Meter Glass Cell

Although the stainless steel cell allows long absorbing paths to be obtained, it is not readily adapted for photochemical studies since the walls are opaque. During the past year, a 6 m multiple traversal cell has been constructed with glass walls. As shown in Fig. 3, the main body of the cell consists of four 1.5 m lengths of Corning low expansion borosilicate glass with an internal diameter of approximately 29 cm. The ends of these tubes are ground flat and butted against stainless steel spacers, 25 mm thick, with teflon gaskets. Vacuum tight joints are made by bolting the glass tubes together by means of flanges on each side of the joints. Stainless steel end plates E are attached to the ends of the cell in a similar manner. Windows to allow infrared radiation to enter and leave the cell have been placed in one end plate. The other end plate has an outlet to the vacuum pump and mechanical feed throughs to adjust the mirrors.

Tables, 2.8 m long, were constructed from 5 x 5 cm angle iron to support each pair of tubes. For ease in moving, castors were attached to each table. When the tube was in its final position the two tables were rigidly bolted together and the castor wheels were lifted off the floor by levelling screws attached to the base of each table.

The tubes were mounted on the tables by attaching 2.5 cm diameter steel rods, which extend horizontally, to spacers $S_1$ and $S_3$, as shown in Fig. 4. These rods pass through holes in vertical blocks of aluminum mounted on bases with levelling screws which rest on the horizontal lengths of angle iron forming the table top. These blocks carry the main weight of the glass tubes. To prevent rotation of tubes about the rod axis, angle iron cradles were placed about 1 m from the spacers $S_1$ and $S_3$. Details of these cradles are shown in Fig. 5. The cradles are also supported on the same angle iron as the spacers and can be adjusted by levelling screws.

The pairs of tubes on each table were adjusted to be in the same horizontal plane before the entire assembly was bolted together at $S_2$.

The system has been evacuated to a pressure of less than 1 Torr and a leak rate of less than 1 Torr/wk has been measured. With the system evacuated a strain gauge consisting of a pair of crossed polaroids was used to investigate the strain in the glass tubes. Although some strain was observed it is fairly evenly distributed around the tubes.

A gas inlet has been provided in each of the spacers and also in the endplates, as shown in Fig. 6, to help ensure a uniform distribution of gases throughout the cell.

The entire length of the cell can be irradiated by banks of fluorescent lamps. The holders for these lamps are attached to lengths of 2 cm wide aluminum channel mounted to metal frames surrounding the tube as shown in Fig. 7. These frames also rest on the horizontal angle iron of the mounting table.

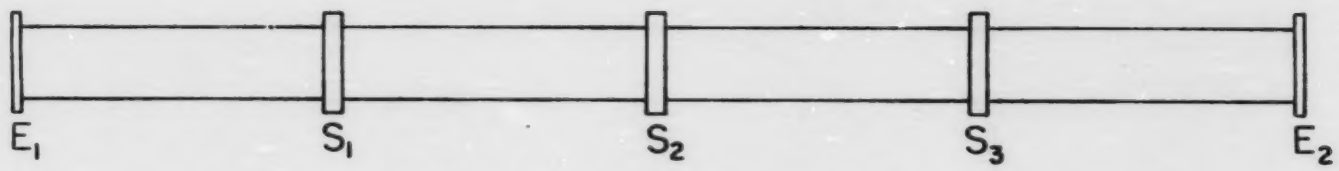


Figure 3. Six-meter glass cell construction details. Stainless steel spacers separate the tube and stainless steel end plates, E, are shown.

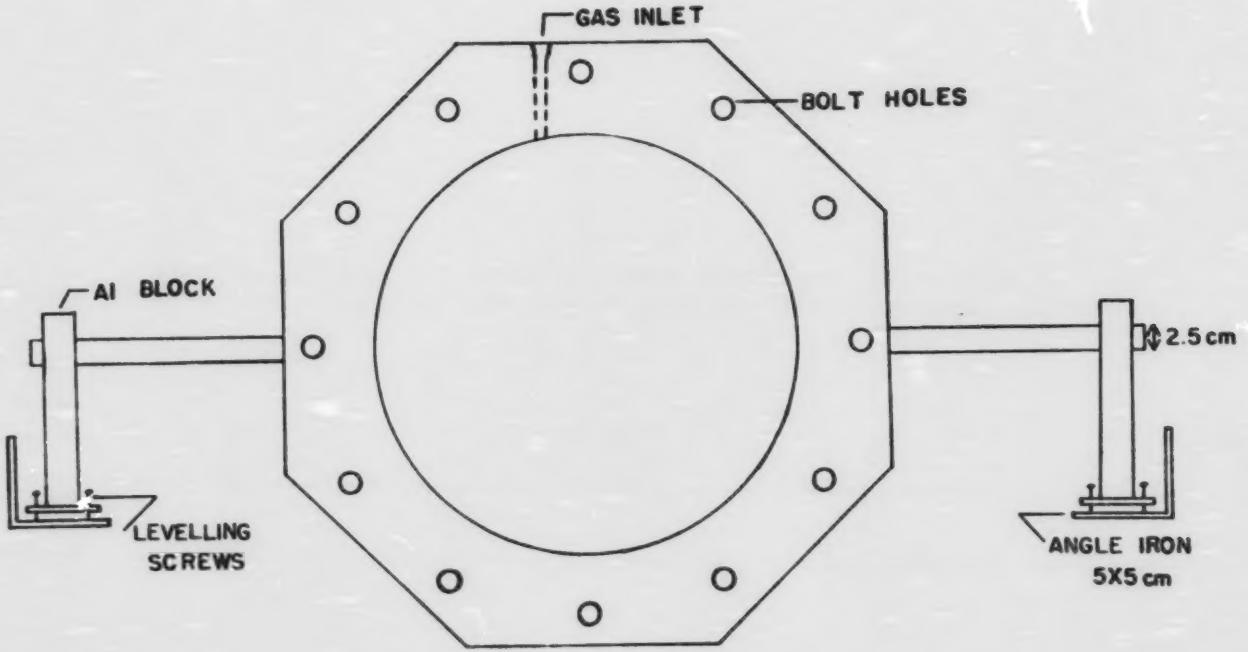


Figure 4. Support system for 6 m cell

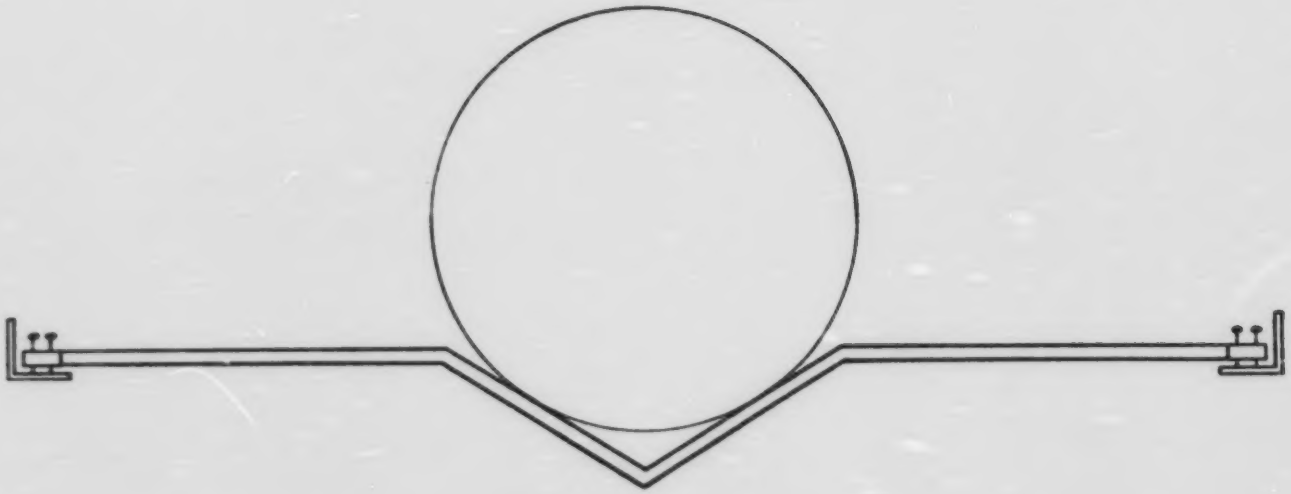

Figure 5. Cradle supports for 6 m cell

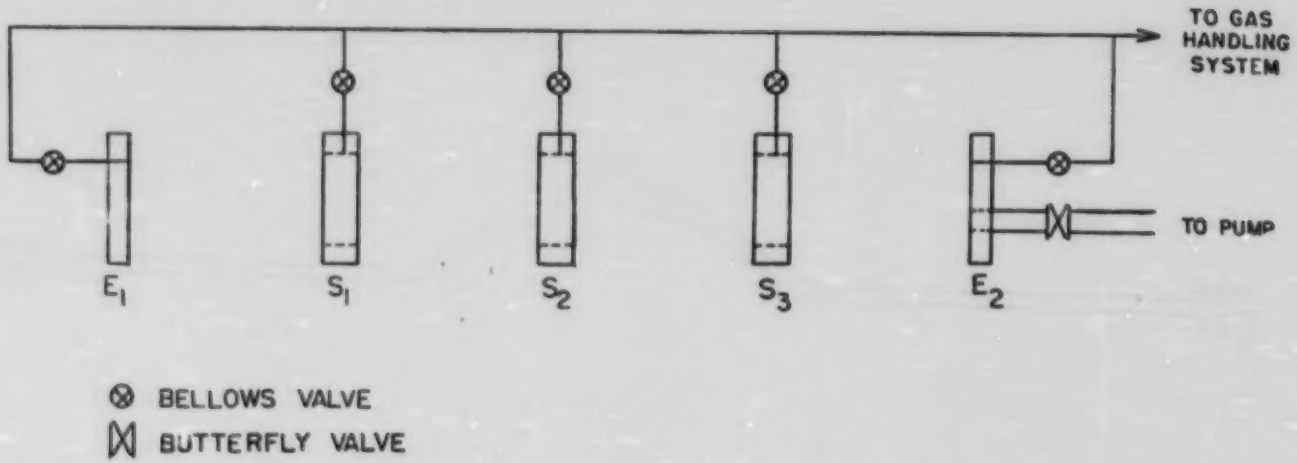


Figure 6. Gas inlet system to 6 m cell

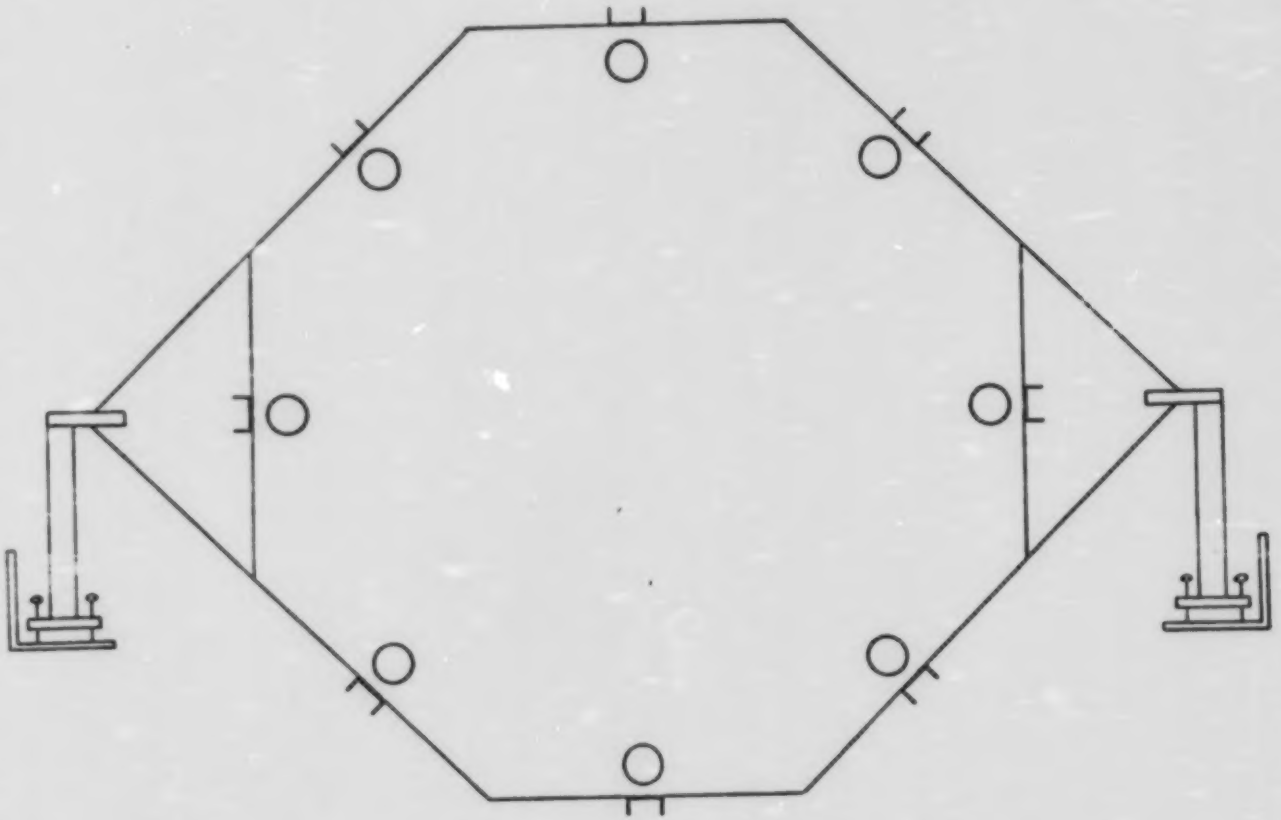

Figure 7. Support system for fluorescent lamps around 6 m cell

Four banks of lamps have been installed along the length of the tubes as shown in Fig. 8a. Three of the banks consist of eight 1.8 m long tubes arranged symmetrically around the glass cell. The individual banks are overlapped by about 15 cm to improve the uniformity of irradiation. A bank of ten lamps 1.2 m long was placed at one end of the cell. The two extra lamps were included since the spectral radiance of these shorter tubes is about 20% lower than that of the 1.8 m tubes.

The electrical wiring diagram is shown in Figs. 8b and c. The irradiation of the cell can be varied by switching 2, 4, 6, or 8 lamps in each bank. Based on the manufacturers literature it is estimated that, with all the lamps on, the irradiation in the cell is approximately equal to the solar irradiance of the lower atmosphere.

The fluorescent lamp assembly is surrounded by an aluminum foil reflector. The foil is supported by a flexible plastic backing as shown in Fig. 9.

The lower reflector is held in position by cords attached to the horizontal angle iron of the table top. The upper reflector is held in position by a 2 x 2 cm aluminum angle iron frame, which also rests on the horizontal angle iron of the table top. The foil is attached to the plastic backing by rubber cement.

The fluorescent lamps installed in the system are GE FT2T12/BL/HO and F40BL black lights. The spectral radiance of these lamps, as described by the manufacturer, shows that the greater part of the output lies in the spectral region from 3000-4000 Å. The emission of a 1.2 m lamp was measured with a Turner spectrophotometer and the spectrum obtained is shown in Fig. 10a. A similar spectrum, obtained after the radiant energy had passed through the wall of the glass cell is also shown together with the estimated relative spectral distribution of solar radiation[3] for a solar altitude of 45°. The spectral transmittance of the glass tube is shown in Fig. 11.

The uniformity of the irradiance inside the cell due to the fluorescent lamps has been measured with a Hewlett Packard 8330A radiant flux meter. The measurements indicate uniform irradiance along the length of the glass cell and variations of less than a factor of three radially from the cell center to the walls.

It is planned to observe changes in the concentrations of the gases in the cell by monitoring their infrared absorption bands. The multiple traversal optical system is a modified White arrangement and has been described by Hanst.[4] Figure 12 shows that the single mirror $M_P$ in Fig. 1 has been replaced by four rectangular mirrors, $M_a$, $M_b$, $M_c$, and $M_d$, and the pair of mirrors $D_1$ and $D_2$ have been replaced by four quadrant shaped mirrors. After the system has been aligned, an image of the source is formed in the place of the mirrors M near $M_b$. Rows of images are formed on $M_a$, $M_b$, $M_c$, and $M_d$ after reflections by the mirrors $D_1$,

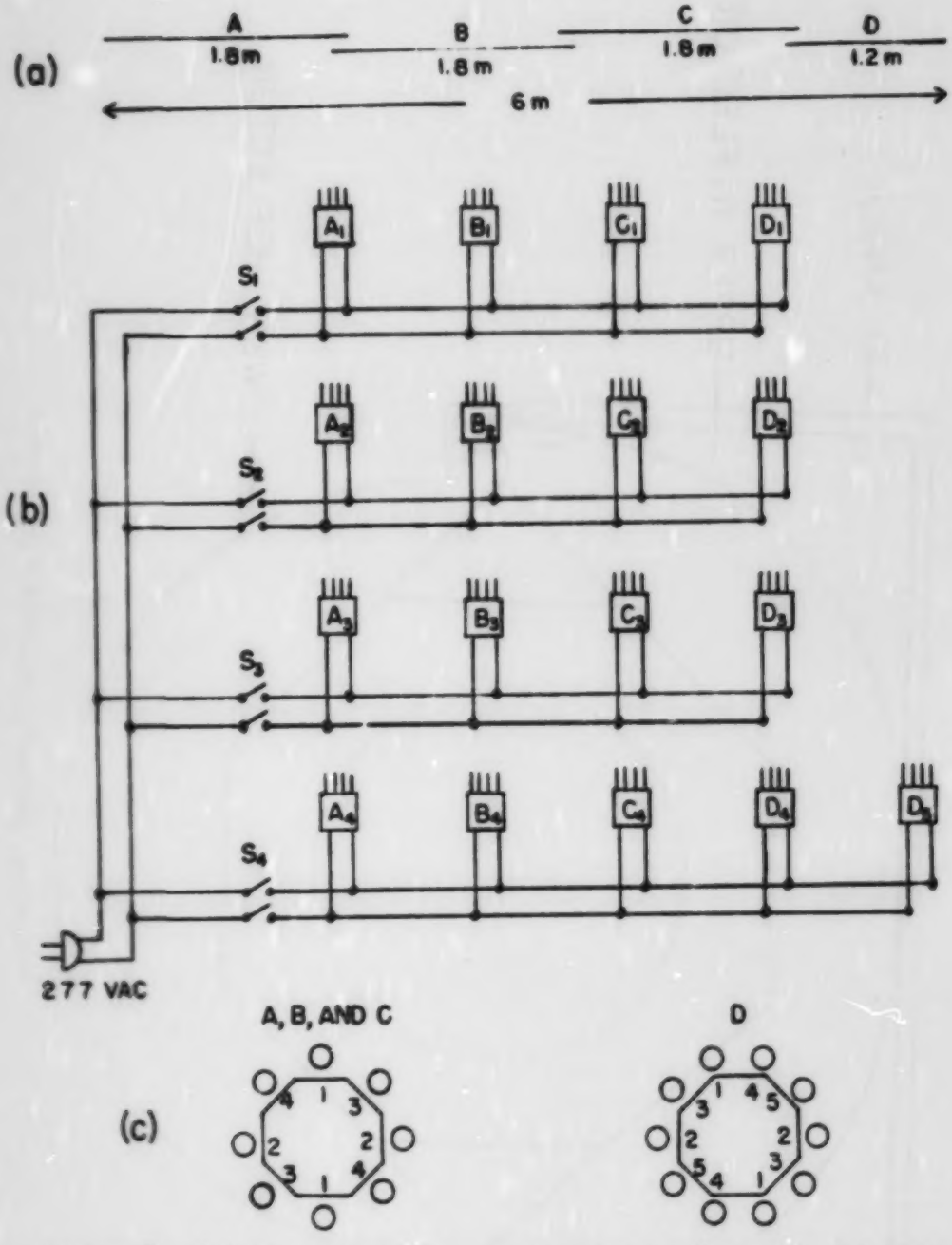


Figure 8. (a) Fluorescent lamp arrangement for 6 m cell; (b) Wiring diagram for lamps. The ballasts $A_1$, $A_2$, $A_3$, and $A_4$ supply power for the lamps in Bank A of Fig. 8a. Switch $S_1$ trols the power to the lamps as shown in Fig. 8c

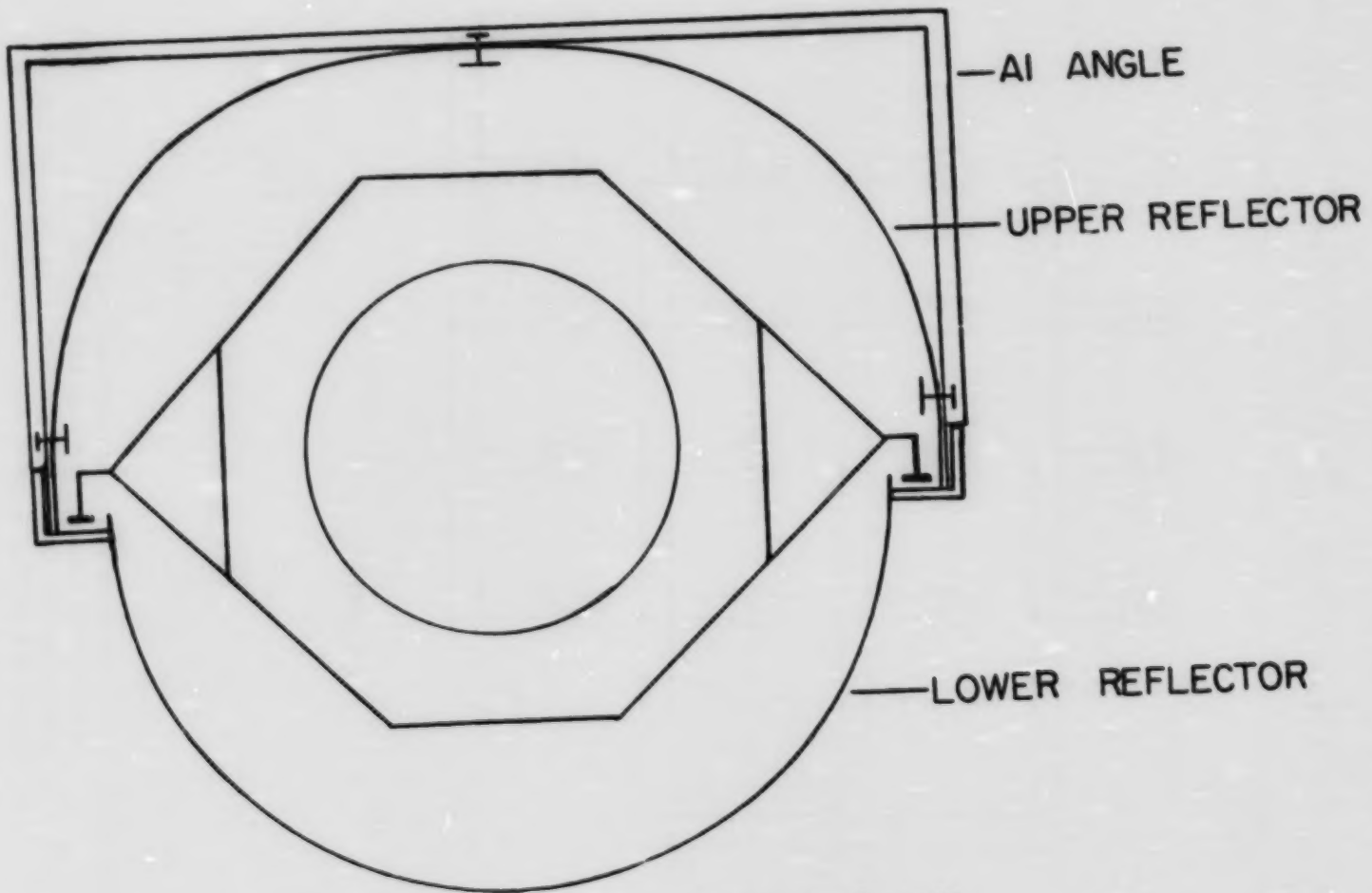


Figure 9. Reflector supports for 6 m cell

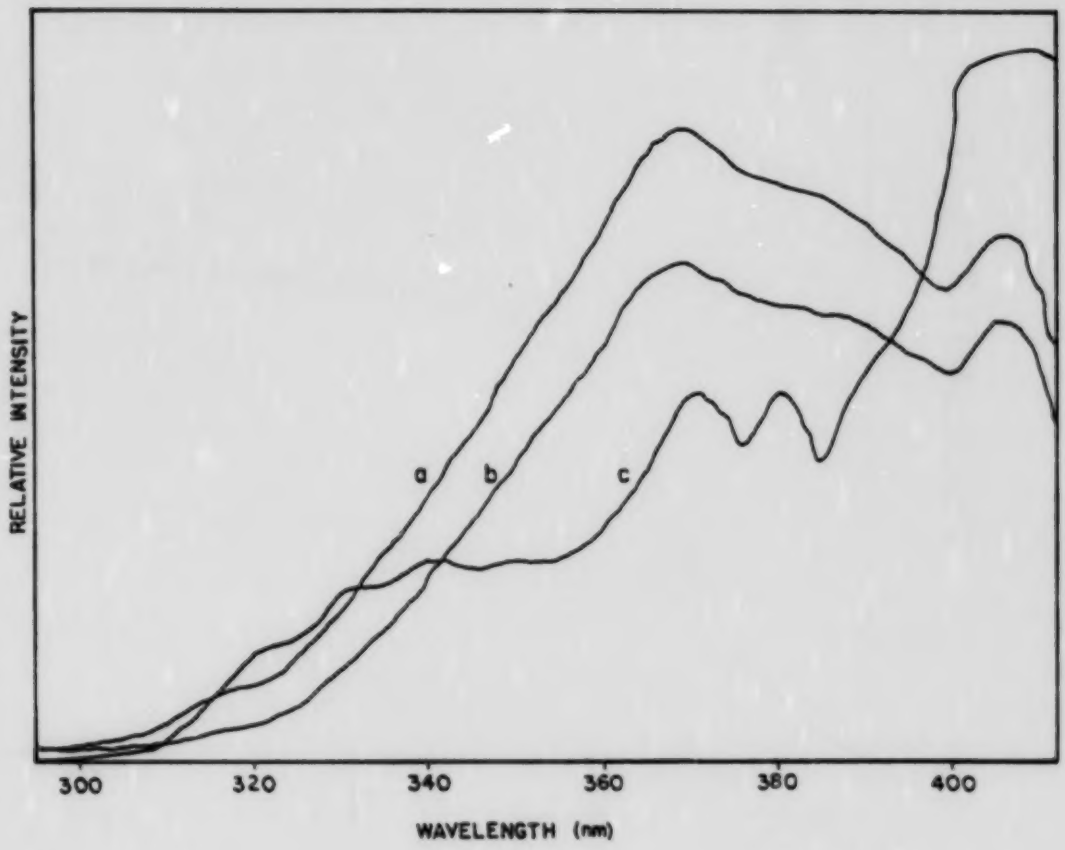


Figure 10. (a) Spectral distribution of fluorescent lamp output;
(b) Spectral distribution of fluorescent lamp output after passing through glass walls of cell;
(c) Relative spectral distribution of solar energy at ground level

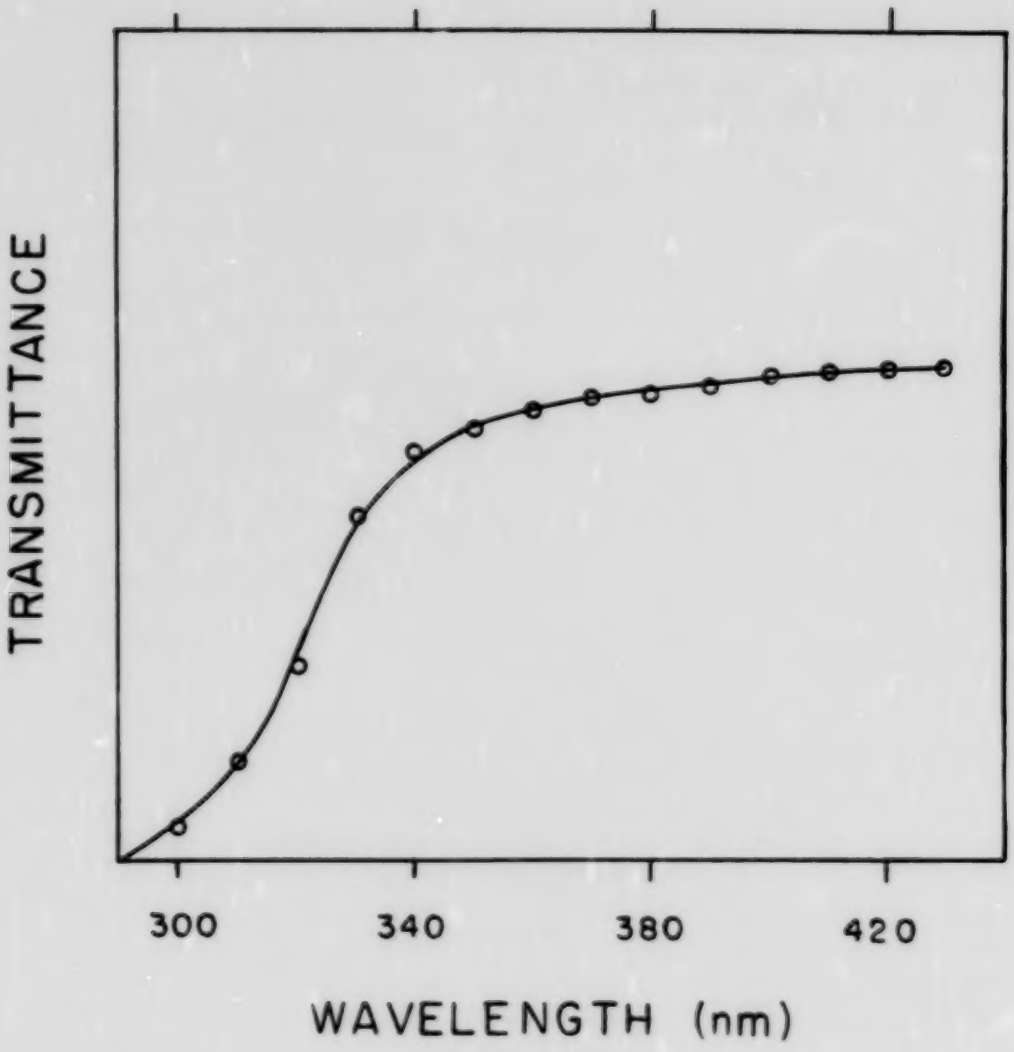


Figure 11. Spectral transmittance of glass tubes of 6 m cell

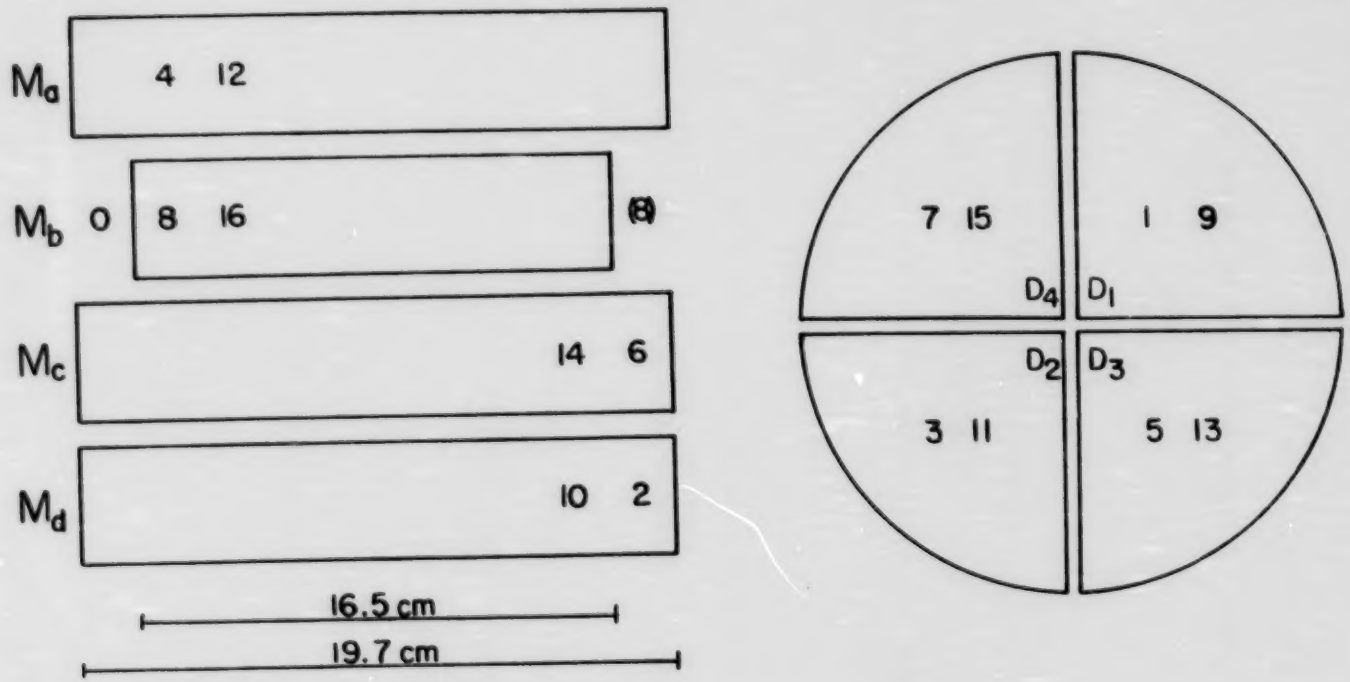


Figure 12. Mirror system for 6 m cell. The numbers refer to consecutive reflections by the mirros. The number of traversals is altered by turning $D_4$

$D_2$, $D_3$, and $D_4$. The radiant energy leaves the cell on the opposite side of $M_b$. In order to form each image on the mirrors M the radiant energy has to make two traversals of the cell.

The maximum number of images which can be formed on $M_b$

$$N_{max} = \frac{D_{M_b}}{d} \tag{10}$$

where

$D_{M_b}$ = length of $M_b$ (16.5 cm), and

d = width of entering beam at $M_b$.

When used with an IFTS instrument this beam will typically have a circular cross section of area A where

$$A = \pi r^2 = \pi\left(\frac{d}{2}\right)^2 \tag{11}$$

Since there are four rows of images, one on each of the mirrors $M_a$, $M_b$, $M_c$, and $M_d$, the total number of images is $\simeq 4N_{max}$, and since each image results from two traversals of the cell, the maximum path length

$$L_{max}(\text{meters}) = 8\ RN_{max} = 44\ N_{max}$$

where the distance between the mirrors R = 5.55 m.

Assuming d $\simeq$ 10 mm then, from Eq. (9)

$$N_{max} = 16$$

and

$$L_{max} \simeq 700 \text{ m.}$$

It is now possible to calculate the $A_g\omega_g$ product for this cell as in Eq. (7)

$$A_g\omega_g = \pi\left(\frac{d}{2}\right)^2 \frac{A_D}{R^2} \tag{12}$$

where

$$d = 10 \text{ mm}$$

$$A_D \simeq \pi r^2$$

$$r \simeq 5 \text{ cm}$$

$$R = 5.5 \text{ m}$$

$$A_g\omega_g = 2.0 \times 10^{-4} \text{ cm}^2\text{sr}. \tag{13}$$

This $A_g\omega_g$ product is approximately the same as that for the stainless steel cell.

## 5. Fourier Transform Spectrometer and Transfer Optics

The IFTS available for this study is a Digilab Model FTS 20. It is capable of achieving 0.125 $cm^{-1}$ resolution. The principle of operation is based on the Michelson interferometer and is well known. An essentially parallel beam of radiant energy falls on the germanium beam splitter B-S, shown in Fig. 13. Here part of the beam is reflected to the fixed mirror $M_4$ and some fraction of the beam reflected by $M_4$ is transmitted through the beam splitter. Part of the incident beam is also transmitted by the beam splitter to $M_5$ when it is reflected back to the beam splitter and is then reflected. The emerging beam is a combination of energy from $M_4$ and $M_5$. This beam then passes through the absorption cell to a detector.

In operation, the detector output is sampled as the mirror $M_5$ moves from a position of zero path difference between the beam splitter and $M_4$ and $M_5$ through a maximum distance of 4 cm. This output is computer processed to provide a spectrum of the source modified by absorption in the path.

It is well known that the maximum resolution in this spectrum is given by

$$\Delta\nu = \frac{1}{2d} \tag{14}$$

when d = distance travelled by $M_5$ from the position of zero retardation. If d = 4 cm, $\Delta\nu$ = 0.125 $cm^{-1}$. In order to achieve this resolution, which is independent of frequency, the divergence of the beam falling on the beam splitter (and which consequently reaches the detector) must be such that

$$R = \frac{\nu}{\Delta\nu} \leq \frac{2\pi}{\omega_I} \tag{15}$$

when R is the resolving power of the instrument at frequency $\nu$, and $\omega_I$ is the solid angle containing the radiation falling on the beam splitter.

When a germanium beam splitter is used the maximum practical spectral frequency which can be observed is ~ 4000 $cm^{-1}$. Thus, for $\Delta\nu$ equal to 0.125 $cm^{-1}$

$$\omega_I \leq 1.96 \times 10^{-4} \text{ sr}. \tag{16}$$

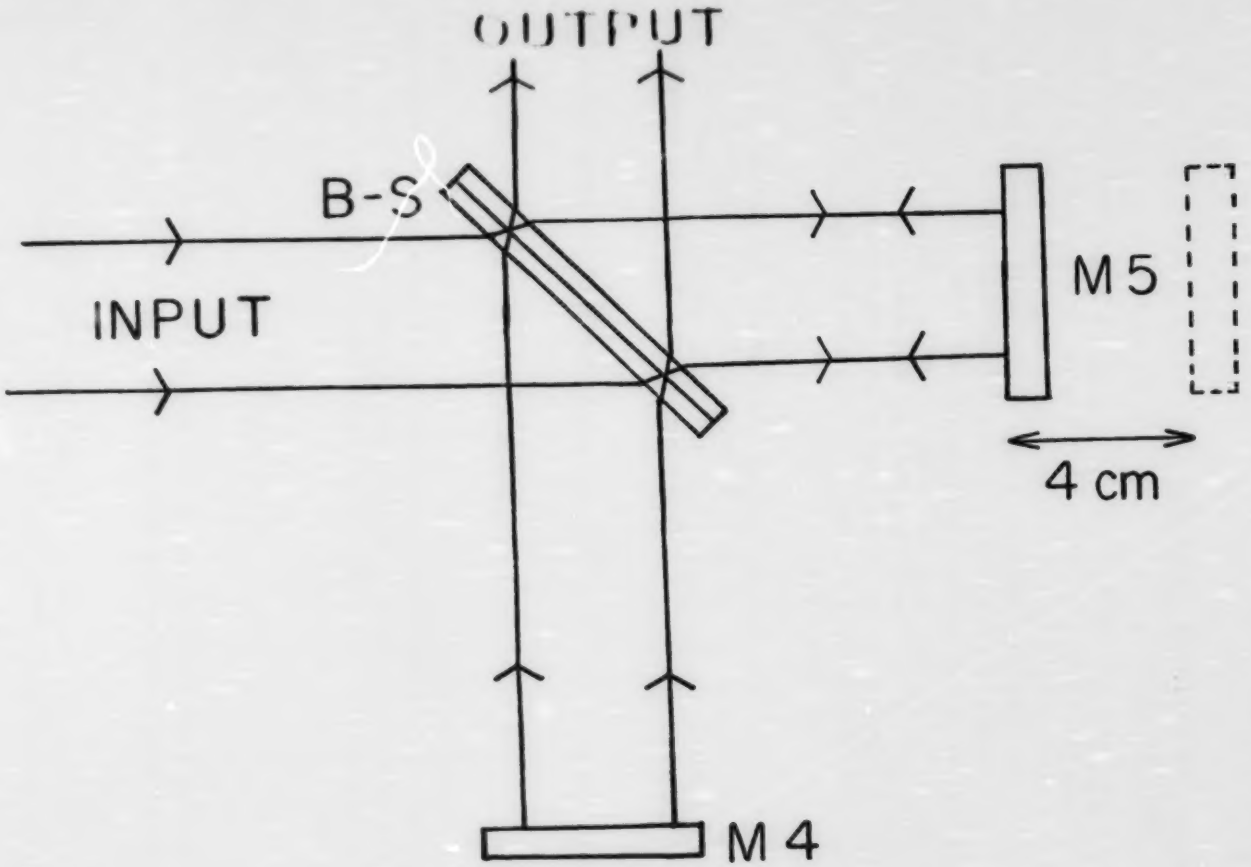


Figure 13. Optical diagram of interferometer

According to the manufacturer's specifications, the maximum allowable diameter of the beam falling on the beam splitter to obtain this resolution is 1 inch. Thus the cross-sectional area of the beam

$$A_I = \pi r^2$$

$$\approx 5.0 \text{ cm}^2$$

and

$$A_I \omega_I \leq 10^{-3} \text{ sr cm}^2$$

This value is that required to obtain 0.125 $cm^{-1}$ resolution at 4000 $cm^{-1}$. Larger values are allowed if measurements are made at lower wavenumbers or lower resolution. The minimum value of $A_I\omega_I$ is, however, approximately five times larger than the $A\omega$ products of the multiple traversal cells previously described when they are aligned for the maximum usable path lengths.

Since the absorption cells are the limiting factors in determining the power transmitted by the system, the optical transfer systems from the source through the interferometer to the cells must be designed to make the actual $A\omega$ products for the beams passing through the cells as close to those which have been calculated. This requires that the optical systems form: (1) images of the source approximately 10 mm in diameter at the field mirrors of the cells. If a Nernst glower, with a diameter of about 1.6 mm and a length of 25 mm is the source, a magnification of a factor of 6 is required to produce images of this width; (2) the aperture stop of the interferometer system and the aperture stop of the absorption cell should be conjugate points. The former is the 1 inch diameter beam allowed at the beam splitter and the latter are the mirrors $D_1$ in Figs. 1 and 12.

Based on these considerations, the optical transfer system shown in Fig. 14 has been used with the 21 m cell. This system can also be used with the 6 m cell with minor modifications since the $A\omega$ products are similar.

Energy from the source N is reflected by the spherical mirror $M_1$ ($f_1$ = 15 cm) to product an enlarged image $N_1$ on the plane mirror $M_2$. Since most of the energy from the elongated image of the source cannot be usefully collected if high resolution is required, all of $M_2$ except a horizontal strip approximately 3 mm wide was covered so that $N_1$ was nearly square. $N_1$ is at the focal point of the off axis paraboloid $M_3$ ($f_3$ = 27 cm) so that collimated radiation falls on the interferometer. After passing through the interferometer the energy is reflected by the plane mirror $M_6$ to the spherical mirror $M_7$ ($f_7$ = 60 cm) which produces a further enlarged image $N_2$ between $M_7$ and $M_8$. An image $B_1$ of the beam splitter is also produced between $M_7$ and $N_2$. After striking the spherical mirror $M_8$ ($f_8$ = 91 cm) the beam passes through the entrance window of the absorption cell and forms an image $N_3$, approximately

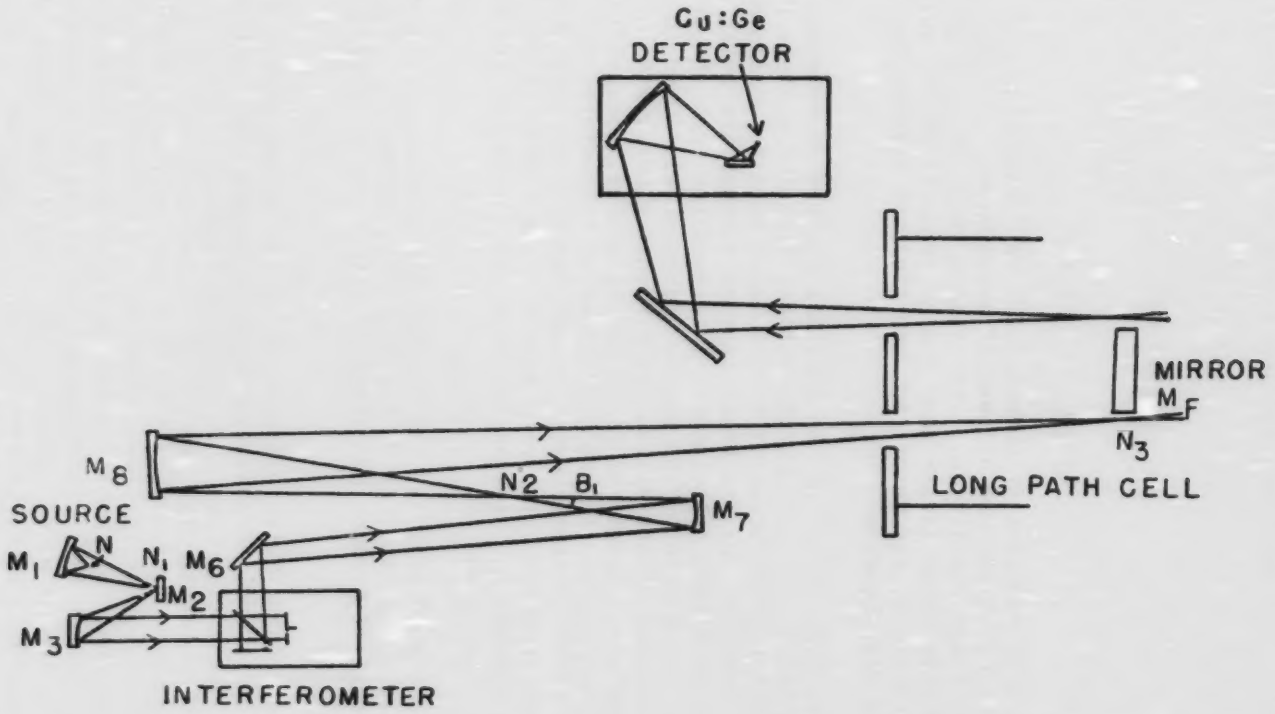


Figure 14. Optical transfer system from interferometer to absorption cell

10 mm wide, in the plane of the field mirror $M_F$ (in Fig. 1) and an image $B_2$ of the beam splitter on the mirror $D_1$ in Fig. 1.

The beam energing from the exit window of the cell is then collected by a detector. The two detectors available include a liquid nitrogen cooled InSb detector for use in the region from 1800 to 4000 $cm^{-1}$ and a liquid helium-cooled, copper-doped germanium detector whose useful range is from 300 to 3500 $cm^{-1}$. Both detectors have sensitive elements approximately 1 mm x 1 mm and can accept radiant energy over a solid angle of about one steradian.

The optical transfer system from the cell to the InSb detector is shown in Fig. 15. This system was designed to produce a 1 mm diameter image N" of the 10 mm diameter image N at M at the detector. The beam from the absorption cell strikes the spherical mirror $M_7$ ($f_9$ = 28 cm) and forms an intermediate image of N at N' and of the mirror $D_2$ at D'. After reflection from the spherical mirror $M_{10}$ ($f_{10}$ = 15 cm) the beam strikes a plane mirror (not shown in the diagram) which directs the beam upwards to the detector at the base of the $LN_2$ dewar. It was found that, when the detector was placed at N", the vibrations of the cell picked up from the surroundings were magnified by the long optical lever arm (equal to the entire optical path in the absorption cell) and caused the image N" to move with an amplitude of 1-2 mm around a fixed position. These excursions seriously perturbed the signal from the detector. A considerable improvement in the signal-to-noise ratio was obtained by placing the detector at D". This image, about 2 mm diameter, overfills the detector but has much less jitter than N" because the optical path $DM_9$ ~ 22 m is smaller than the optical path in the cell. Because the detector is now overfilled and is at a conjugate point to both D and the beam splitter B, it acts as the effective aperture stop of the entire system.

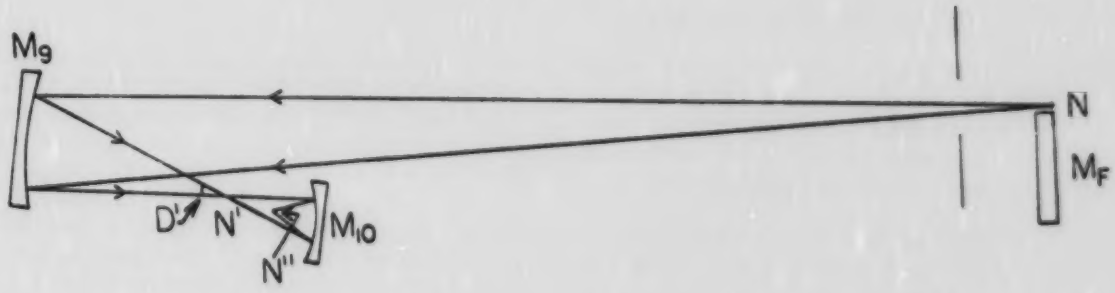


Figure 15. Optical transfer system from absorption cell to InSb detector

The Cu:Ge detector has an associated optical system for use with a conventional Digilab IFTS spectrometer. It is designed to accept a collimated beam and condense it to the detector. This instrument has been placed to receive energy emerging from the cell after reflection by a plane mirror as shown in Fig. 14. This mirror can be adjusted to give maximum detector output. At this point an image of the mirror D is formed on the detector element. As with the InSb detector, the element is overfilled and acts as the aperture stop of the system.

When this detector was received the vacuum in the dewar was poor. The system was modified so that the vacuum chamber is continuously pumped with a cryopump line. After transferring liquid helium to the 0.75 $\ell$ capacity dewar the detector stays cold for 8-10 hours.

6. Coelostat

A coelostat consisting of two plane, 25 cm diameter mirrors is mounted on the roof of the laboratory. One mirror rotates at a constant angular speed about an axis lying in the plane of the mirror and parallel to the earth's polar axis. This mirror reflects solar energy to the second mirror which directs the beam into the laboratory. This instrument has been used with the interferometer to obtain solar spectra.

The solid angle subtended by the sun at the earth, $\omega_s = 6.8 \times 10^{-5}$ sr, is smaller than the minimum solid angle required to fill the interferometer, $\omega_{f,min} = 1.96 \times 10^{-4}$ sr. Although a higher energy throughput through the interferometer could be achieved by using a mirror telescope, the spectral radiance of the sun is so great that the improvement in signal-to-noise ratio gained by its use is not significant, and excellent spectra are obtained by directing the beam from the coelostat directly onto the interferometer. The angular diameter of the sun, $\alpha_s = 9.4 \times 10^{-3}$ rad, requires a 10 cm focal length mirror to condense the energy onto a 1 x 1 mm$^2$ detector.

7. Gas Handling System

The gas handling system shown in Fig. 16 was constructed to inject premeasured amounts of gas into the 21 m stainless steel absorption cell. This gas handling system was made entirely of glass and stainless steel and was fitted with teflon stopcocks. Samples of up to five gases can be stored in this system at one time.

Before the system is used, the entire volume is evacuated by a Sargent-Welsh duo-seal pump, Model 1405 H. Ultimate vacuum in the gas handling system is about 10 mmHg. After pumping, the stopcock to the pump is closed and a sample gas is expanded into the glassware. One of the five storage bulbs is opened and the pressure of the sample gas is measured on Wallace-Tiernan gauges which are isolated from the sample gas by a quartz spiral gauge. One Wallace-Tiernan gauge has a range of 0-20 Torr, the second gauge covers the range 0-50 Torr, and the third

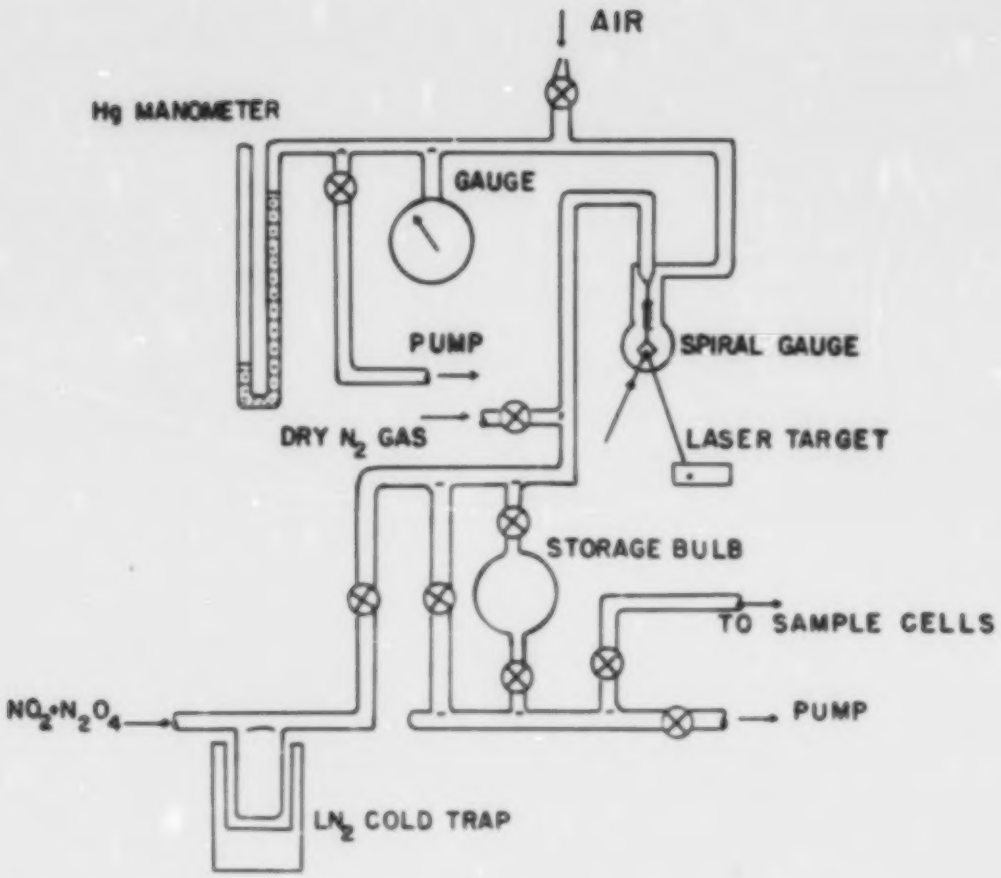


Figure 16. Gas handling system

gauge covers the range 0-800 Torr. These gauges were calibrated against a mercury manometer. It is estimated that pressures above 100 mm can be measured to a precision of better than ± 0.1% and an absolute accuracy of ± 0.2% standard deviation.

When the desired amount of gas has been injected into the gas handling system, the stopcock to the storage bulb is closed, and the excess sample gas is pumped out of the glassware by the pump. The gas is exhausted out of the laboratory through a ventilator. Nitrogen is flushed through the glassware to remove any residual sample gas, and the glassware is again evacuated.

The entire filling process is repeated if it is necessary to measure out another gas. The gas handling system has five gas storage bulbs. Each storage bulb is approximately 1 $\ell$ in volume. The volumes of these cells were obtained from the observed pressure changes when a gas sample contained in a known calibrated volume was successively expanded into the gas lines and then into each storage bulb. A series of independent measurements of the individual volumes gave a reproducibility of ± 0.3% (standard deviation). When the gas handling system is connected to the 21 m stainless steel cell, which has a volume of $9.53 \times 10^{-3}$ $\ell$, the pressure of sample gas in the cell can be computed from the pressure of sample gas in the 1 $\ell$ bulb. Assuming the ideal gas law

$$P_1 V_1 = P_2 V_2$$

$$P_1 = P_2 \frac{V_2}{V_1}$$

$$P_1 = \frac{P_2}{9.53 \times 10^{-3}}$$

Pressure and volume in cell and bulb are designated respectively by subscripts 1 and 2. Thus, there is a reduction in pressure by a factor $\sim 10^4$ when the gas is expanded into the cell. If a storage bulb is filled to one atmosphere with a sample gas, the concentration of gas in the cell will be ~ 100 ppm when the gas is expanded into the cell.

Because of the large difference in volumes between the cell and the bulb it can be assumed that a complete transfer of gas in its sample bulb to the cell occurs provided the cell is initially evacuated so that $P_2 \ll P_1$. To ensure complete injection, the sample system is first filled with nitrogen to an atmosphere and then opened to the cell and flushed with nitrogen. The procedure is repeated four to six times to transfer the gas sample into the cell. The concentrations of gases introduced into the absorption are obtained from measurements of the volumes of the storage bulbs, the volume of the cell and sample pressure measurement. It is estimated that the maximum error of the amount of gas transferred to the cell is on the order of ± 2%. The actual amount of gas in the absorbing path depends on the degree of mixing in the cell and adsorption/desorption effects of the walls.

## B. EXPERIMENTAL PROCEDURES

### 1. Spectroscopic Studies of Chemical Reactions

In order to follow chemical kinetics of reactions, an accurate knowledge of the concentrations of reactants and products as functions of time are required. Not infrequently, direct measures of these quantities are impossible and they can only be inferred from other related properties. In this work, absorbance measurements of selected transitions of various molecules are employed to relate to their corresponding concentrations according to the Beer-Lambert law:

$$a = \epsilon c \ell \tag{17}$$

where

$a$ = absorbance

$\epsilon$ = absorption coefficient

$c$ = concentration (see Appendix C) and

$\ell$ = path length.

In the regime where the above relationship holds, monitoring the absorbance of an infrared band of the molecule of which $\epsilon$ and $\ell$ are known gives the corresponding concentration of that compound. Although integrated band absorbance data were not measured in this study, nevertheless, the monitoring of peak absorbances of selected transitions at constant spectral resolution can give an unambiguous measure of the concentrations.

The spectrometer system employed is a single beam instrument and, in order to obtain the absorbance of a sample of a given compound, a background spectrum of the detector profile and the evacuated cell must first be recorded to be ratioed against the sample spectrum taken at a later time. An illustration of the ratioing process is shown in Fig. 17. The top spectrum is a single beam spectrum of the detector profile and an evacuated cell; the middle one is a single beam spectrum obtained of a sample mixture of $NO_2$ and $N_2O_4$ in the same cell. The profile of the background makes it difficult to determine accurately the concentration of the gases. In addition, absorbance caused by atmospheric $CO_2$ and $H_2O$ also appears in the spectrum which overlaps the $NO_2$-$N_2O_4$ absorption bands. The bottom spectrum corresponds to a ratioed spectrum of the sample spectrum against that of the background. The unwanted $CO_2$ and $H_2O$ absorptions are almost completely ratioed out and a well-defined baseline is obtained which makes the determination of absorbance unambiguous.

Since the optical system is not purged, atmospheric $CO_2$ and $H_2O$ absorbance may overlap infrared bands of other compounds of interest.

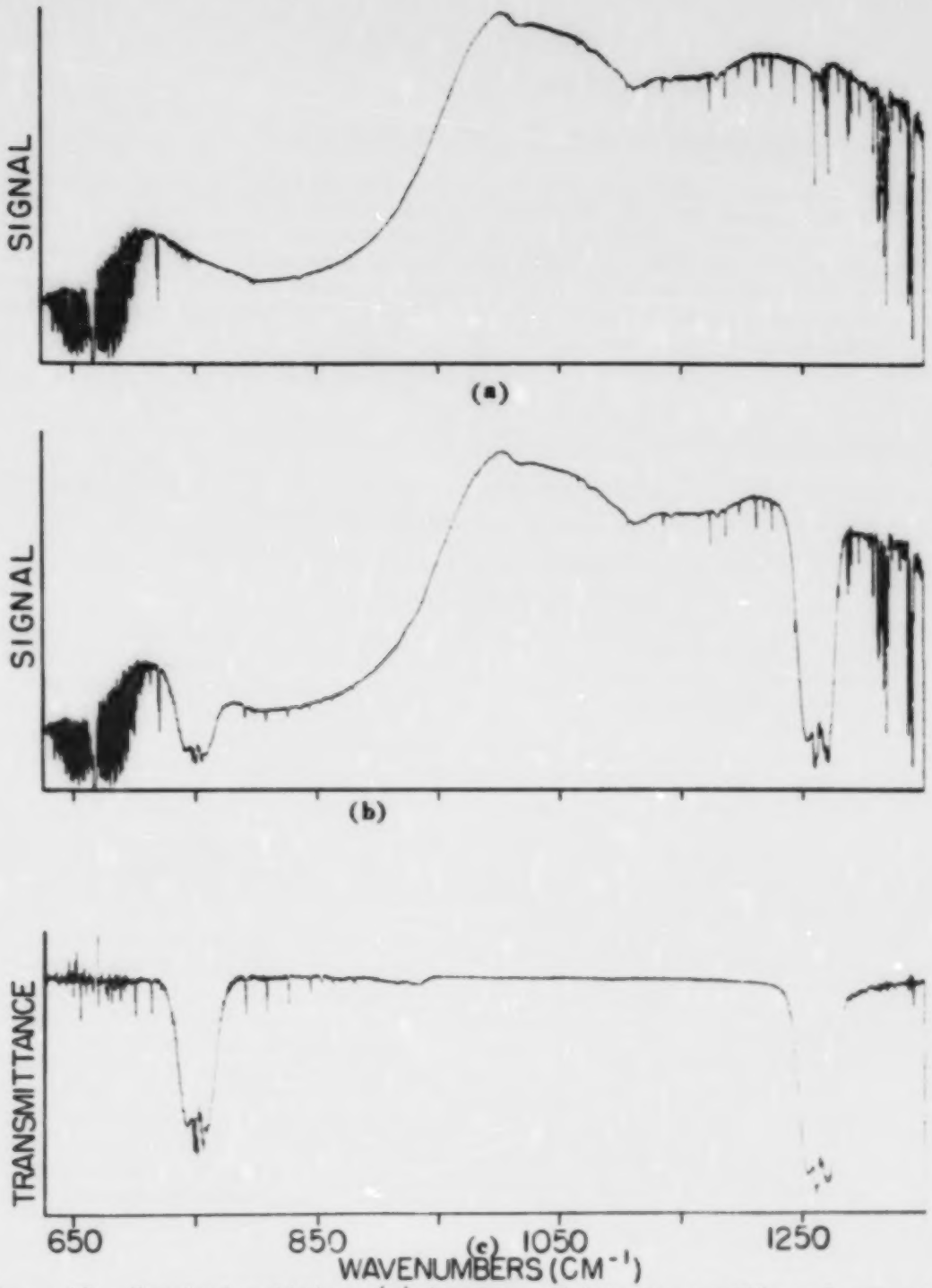


Figure 17. Spectral ratioing, (c) Spectrum of detector profile and evacuated cell; (b) Spectrum with sample of $NO_2$ and $N_2O_4$ in cell; (c) Ratio of spectrum (b)/spectrum (a). Spectral resolution 0.5 $cm^{-1}$

Although there are many bands of NO, $NO_2$, and $HNO_2$ in the mid-infrared region, they are not all used for concentration monitoring purposes because they are either interfered by $CO_2$ and $H_2O$ or by mutual interference. The bands that are monitored to obtain concentration information are for $NO_2$, the $\nu_2$ band, Q-branch transition at 823 $cm^{-1}$; for NO, the fundamental band Q-branch transition at 1876 $cm^{-1}$; for cis-HONO; the $\nu_4$ band Q-branch transition at 853 $cm^{-1}$, and for trans-HONO, the $\nu_3$ band Q-branch transition at 1264 $cm^{-1}$. All absorbance measurements were made at a total pressure of 700 mm.

## 2. Calibration of NO and $NO_2$ Gases and HONO

To apply the concept discussed in Section B.1 a number of correlation curves of absorbance and concentration was generated. Both NO and $NO_2$ gases are stable at room temperature and their concentration can be easily measured. However, the $HNO_2$ molecules are rather unstable and correlation curves cannot be generated directly. The method used to determine the $HNO_2$ concentration will be described later.

### a. Calibration of NO and $NO_2$

The calibration of NO and $NO_2$ gases has been carried out in three cells of 7.5 cm, 39.5 cm and 21 m path lengths, respectively. Known pressures (mmHg) of NO (99%, Matheson Co.) were measured and injected into these cells. High purity nitrogen gas was used to bring the total pressure to 700 mmHg. Then the spectrum of the sample gas was taken and ratioed against the proper background spectrum of the cell filled with high-purity nitrogen to a total pressure of 700 mm. A series of spectra taken at room temperature (23 ± 1°C) with varied path length concentrations products allowed the absorbance (a) vs. path concentration ($P \cdot \ell$) plot shown in Fig. 18 to be obtained. The band used is the fundamental rotation vibration band of NO which has an isolated and distinct Q-branch absorption at 1876 $cm^{-1}$.

Because $NO_2$ is always in dynamic equilibrium with $N_2O_4$, the total pressure of $NO_2$ measured corresponds to the sum of the partial pressures of $NO_2$ and $N_2O_4$. $NO_2$ ($+N_2O_4$) with a purity of 99.5% was obtained from Matheson Co. and before using, it was trapped with a $LN_2$ cold trap and pumped to remove volatile residual impurities such as NO, $N_2O_3$, $N_2O$, etc. The equilibrium constant for the reaction:

$$N_2O_4 \rightleftharpoons 2NO_2$$

is defined by

$$K = \frac{(P_{NO_2})^2}{P_T - P_{NO_2}}$$

where

$P_{NO_2}$ = partial pressure of $NO_2$

$P_T = P_{NO_2} + P_{N_2O_4}$.

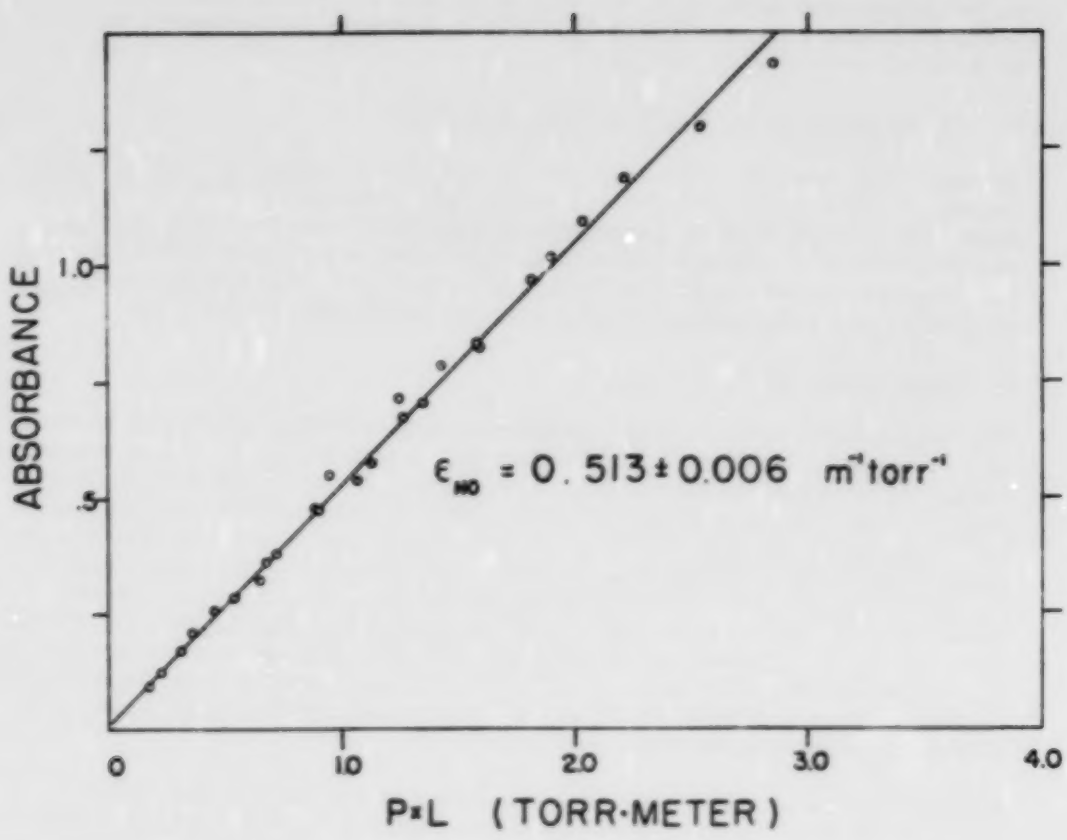


Figure 18. Dependence of absorbance of NO Q-branch (1876 $cm^{-1}$) on the path length x NO concentration product. Total pressure 700 mmHg. Spectral resolution, 0.5 $cm^{-1}$

Hence

$$P_{NO_2}^2 + KP_{NO_2} - P_TK = 0$$

and by solving this quadratic equation, partial pressures of $NO_2$ and $N_2O_4$ can be determined according to

$$\left.\begin{aligned} P_{NO_2} &= (-1 + \sqrt{1 + 4P_T/K})K/2 \\ P_{N_2O_4} &= \frac{(2P_T + K) - \sqrt{K^2 + 4KP_T}}{2} \end{aligned}\right\} \qquad (18)$$

By using the reported equilibrium constant at room temperature for the $NO_2$ - $N_2O_4$ system,[5] and the above equations, partial pressures of $NO_2$ and $N_2O_4$ were determined. Once the $NO_2$ partial pressure is known and the absorbance determined, the calibration curve for $NO_2$ is generated essentially the same way as that for NO gas. A correlation curve for the $NO_2$ Q-branch transition at 823 $cm^{-1}$ at room temperature (23 ± 1°C) is shown in Fig. 19. From these curves, the absorption coefficients for NO at 1876 $cm^{-1}$ and $NO_2$ at 823 $cm^{-1}$ are found to be 0.513 ± 0.006 $mm^{-1}m^{-1}$ and 0.0807 ± 0.0012 $mm^{-1}m^{-1}$, respectively, from least square fits of the data. These results are for a spectral estimation of 0.5 $cm^{-1}$.

b. Calibration of $HNO_2$

Because $HNO_2$ is unstable at room temperature, it was not possible to generate known amounts of this gas. However, absorption coefficients of both cis- and trans-$HNO_2$ can be obtained by either comparing the decrease of $HNO_2$ absorbance to the formation of total $NO_x$ (NO and $NO_2$) in the study of $HNO_2$ decay and formation reactions, or comparing the equilibrium absorbances and concentrations of this system with those expected from the equilibrium constant quoted in the literature. Based on the results of the HONO study reported in Section IV.C, absorption extinction coefficients for the cis-HONO Q-branch at 853 $cm^{-1}$ and the trans-HONO Q-branch at 1264 $cm^{-1}$ are found to be 9.36 ± 0.94 $mm^{-1}m^{-1}$ and 5.20 ± 0.52 $mm^{-1}m^{-1}$, respectively for a spectral resolution of 0.5 $cm^{-1}$.

3. Preparation of Nitrous Acid

Nitrous acid (HONO) was produced by reacting sodium nitrite with dilute sulfuric acid at room temperature. Three methods were attempted: (i) A dilute $H_2SO_4$ solution was added to a dilute solution of $NaNO_2$; (ii) A dilute solution of $H_2SO_4$ was added to $NaNO_2$ solids, and (iii) A dilute $NaNO_2$ solution was added to a dilute $H_2SO_4$ solution. It was found that the first two methods, besides generating $HNO_2$, also generate rather large amounts of NO and $NO_2$. The second method gave a slightly better yield of HONO than the first. The third method gave the highest $HNO_2$ to $NO_x$($NO + NO_2$) ratio and was used in our study. Cooling of the apparatus for the preparation of $HNO_2$ gave no significant improvement in yield of $HNO_2$. The apparatus used is shown in Fig. 20.

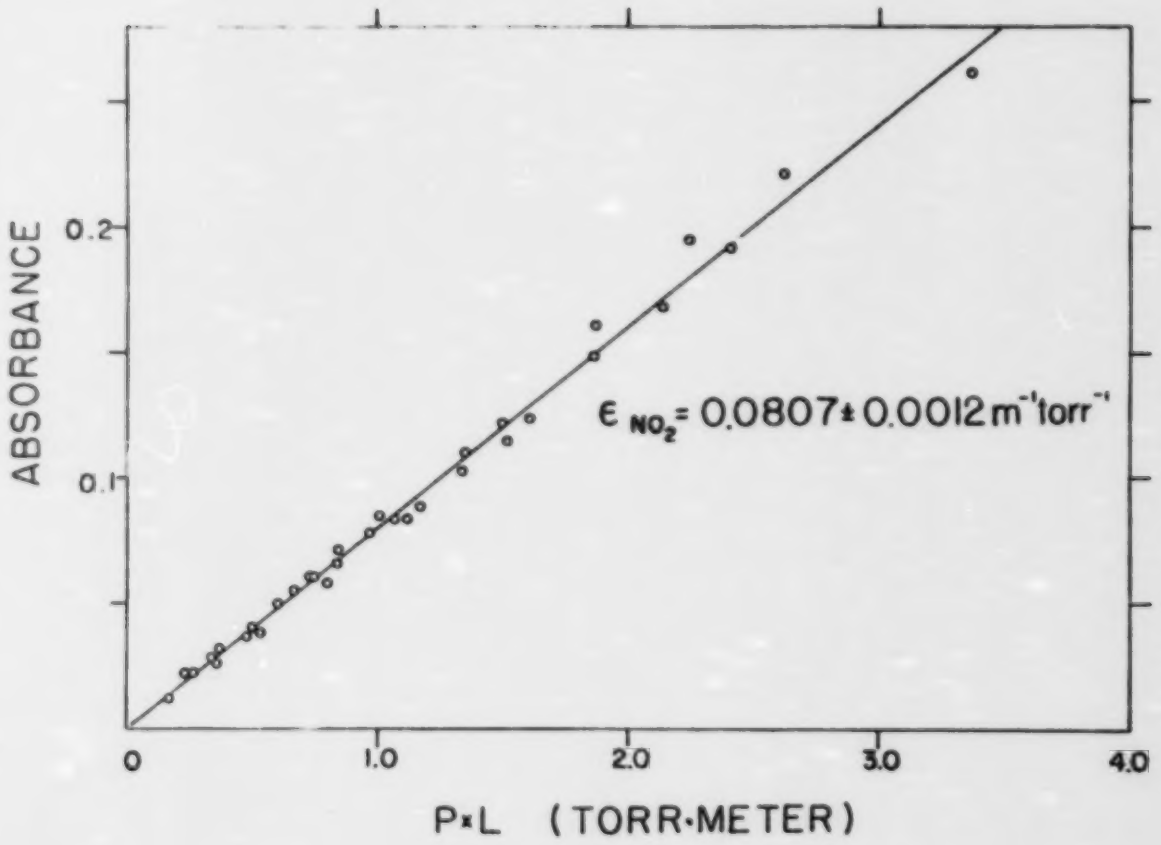


Figure 19. Dependence of the absorbance of $NO_2$ Q-branch (823 $cm^{-1}$) on the path length x $NO_2$ concentration product. Total pressure 700 mmHg. Spectral resolution, 0.5 $cm^{-1}$. Temperature 23 ± 1°C

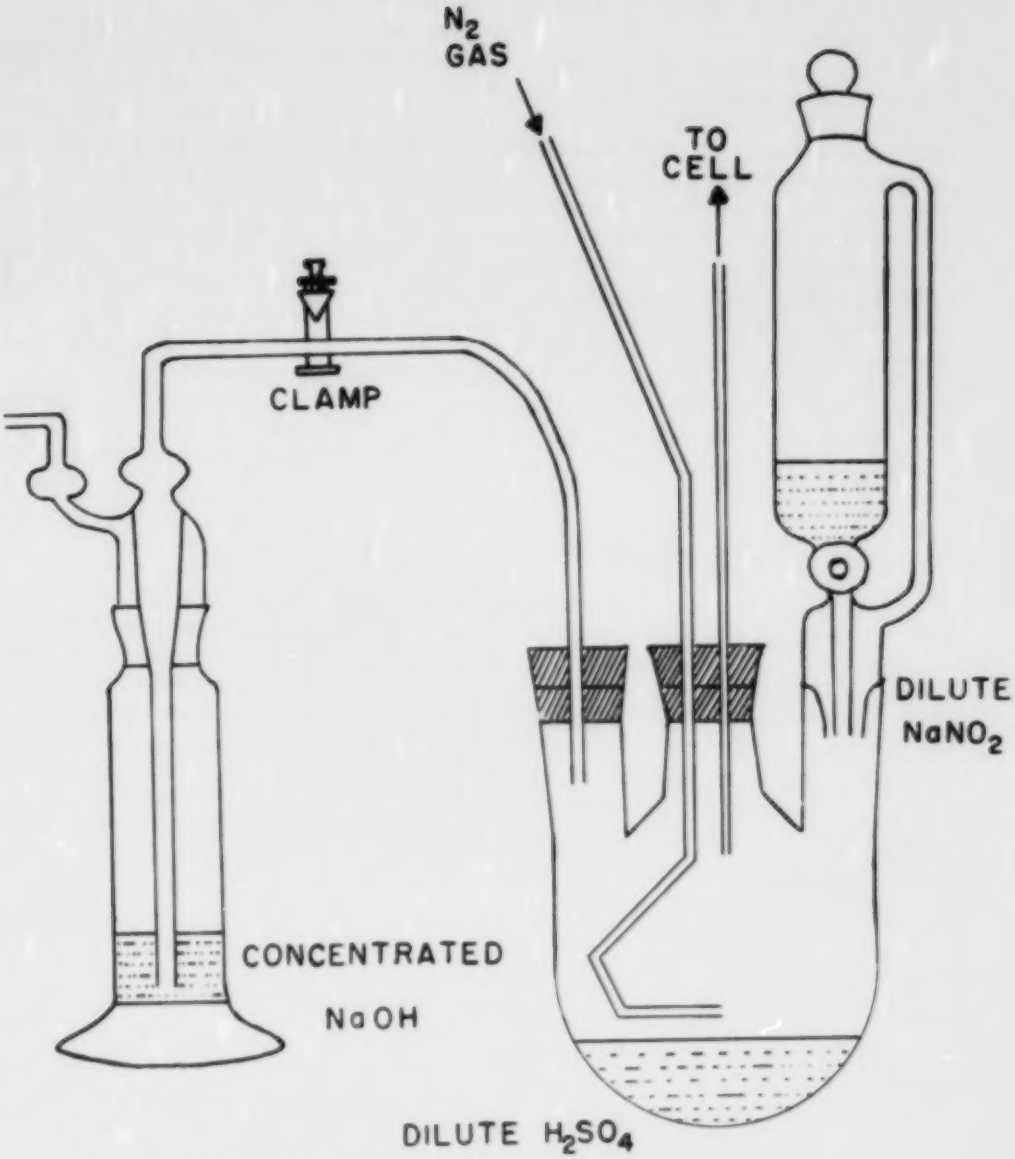


Figure 20. Apparatus for preparation of $HNO_2$

4. Study of $HNO_2$ Decay

Before injection of $HNO_2$ into the reaction cell, a known amount of water was evaporated into the evacuated cell and the cell was then filled to a pressure of 400-500 mm with high-purity nitrogen. The 3-neck flask in Fig. 20 was first flushed and filled with nitrogen. In the process of producing $HNO_2$, the passage to the concentrated NaOH trap is blocked off and that to the absorption cell is open. Dilute $NaNO_2$ solution (~ 0.3 M) was added dropwise to the dilute $H_2SO_4$ solution (~ 2.5 M) in the 3-neck flash. The system was flushed with nitrogen to aid the $HNO_2$ injection into the absorption cell. At the end of the preparation (or 5 minutes after start of reaction), the passage to the cell was closed and the remainder of $HNO_2$-NO-$NO_2$ was trapped in the concentrated NaOH solution. Through another valve with a much bigger opening, high-purity nitrogen gas was injected (in a time of ~ 5-10 min) into the cell to a final pressure of 700 mm. Spectra, each of which took 4 minutes to collect and compute were taken at regular time intervals varying from 4 minutes to 10 minutes and they were ratioed against the background of the evacuated cell recorded before the run of the experiment to obtain absorbances of NO, $NO_2$ and $HNO_2$. $H_2O$ absorbance was not monitored because of interference from atmospheric $H_2O$ in the path external to the cell. All the runs were carried out with a path length in the cell of 250 m. Temperature inside the cell was recorded during the run period by a chromel-alumel thermocouple installed inside the cell.

5. Study of $HNO_2$ Formation

A known amount of $H_2O$ was measured and evaporated into the evacuated cell. This was followed by injection of NO gas before the pressure inside the cell was brought up to ~ 400-500 mmHg. Then $NO_2$ of measured quantity was injected and the cell pressure was increased to 700 mmHg filling it with high-purity nitrogen gas. Spectra were then recorded at regular intervals (~ 10 min) and they were ratioed against a previously recorded background to obtain absorbance data on NO, $NO_2$ and $HNO_2$. All experiments were carried out with a path length of 490 meters. Temperature inside the cell was recorded at intervals.

## SECTION IV

## RESULTS AND DISCUSSION

### A. COLLECTION OF GAS SPECTRA

The investigations which have been undertaken during the past year show the complexity of the spectra of apparently simple gas systems. For example, spectra of $NO_2$, even when well diluted, show evidence of $N_2O_4$ bands, spectra of mixtures of NO and $NO_2$ show evidence of additional bands which may be due to $N_2O_3$; spectra of long air paths show a complex structure due to the permanent atmospheric gases $H_2O$, $CO_2$, $CH_4$ CO, and $N_2O$. In order to make qualitative analyses of any of these spectra it is desirable to have spectra of the individual gases which may be present in a given sample.

The IFTS system available has the ability to collect spectra with 0.125 $cm^{-1}$ resolution over the spectral region from 400 to 4000 $cm^{-1}$. While this resolution is not as high as can be achieved by some instruments, it is nevertheless capable of resolving most of the fine structures of bands of atmospheric gases at ambient temperature and pressure since the half width at half height of the absorption coefficients of lines of most gases is about 0.12 to 0.16 $cm^{-1}$ under these conditions.

One of the advantages of the IFTS over more conventional spectrometers is its ability to store the observed spectra in digital form on magnetic tape; these spectra can be recalled and further processed by the computer to produce spectra with a degraded resolution. At the present time spectra of NO, $NO_2$, $N_2O_4$, $H_2O$, $HNO_2$, and CO have been obtained for a limited range of concentrations and spectral regions.

In addition to obtaining spectra of individual gases we have also initiated a program to collect typical air spectra for a number of different path lengths. These include paths of approximately 10, 100, and 1000 m. The 10 m path includes the air in the optical system from the source to the detector excluding the absorption cell. Four traversals of the absorption cell increases the path to approximately 90 m and 48 traversals of the cell gives a total path length of about 990 m. Typical spectra between 700 and 725 $cm^{-1}$ are shown in Fig. 21 for these paths. Most of the absorption in this spectra region is due to $CO_2$. Also shown in this figure is a solar spectrum obtained with a solar altitude of about 40°. The effective path traversed by the solar radiation is equivalent to about 10 km at surface pressure. By making observations with a solar altitude of less than 5° path lengths equivalent to 50 km at surface pressure have been obtained in some spectral regions. At the present time, spectra of 10, 100, and 100 m have been generated for the region from 400 to 2500 $cm^{-1}$ and solar spectra from 400 to 4000 $cm^{-1}$ for high sun. Solar spectra from 2500 to 3500 $cm^{-1}$ have been obtained for solar altitudes of 2-3°.

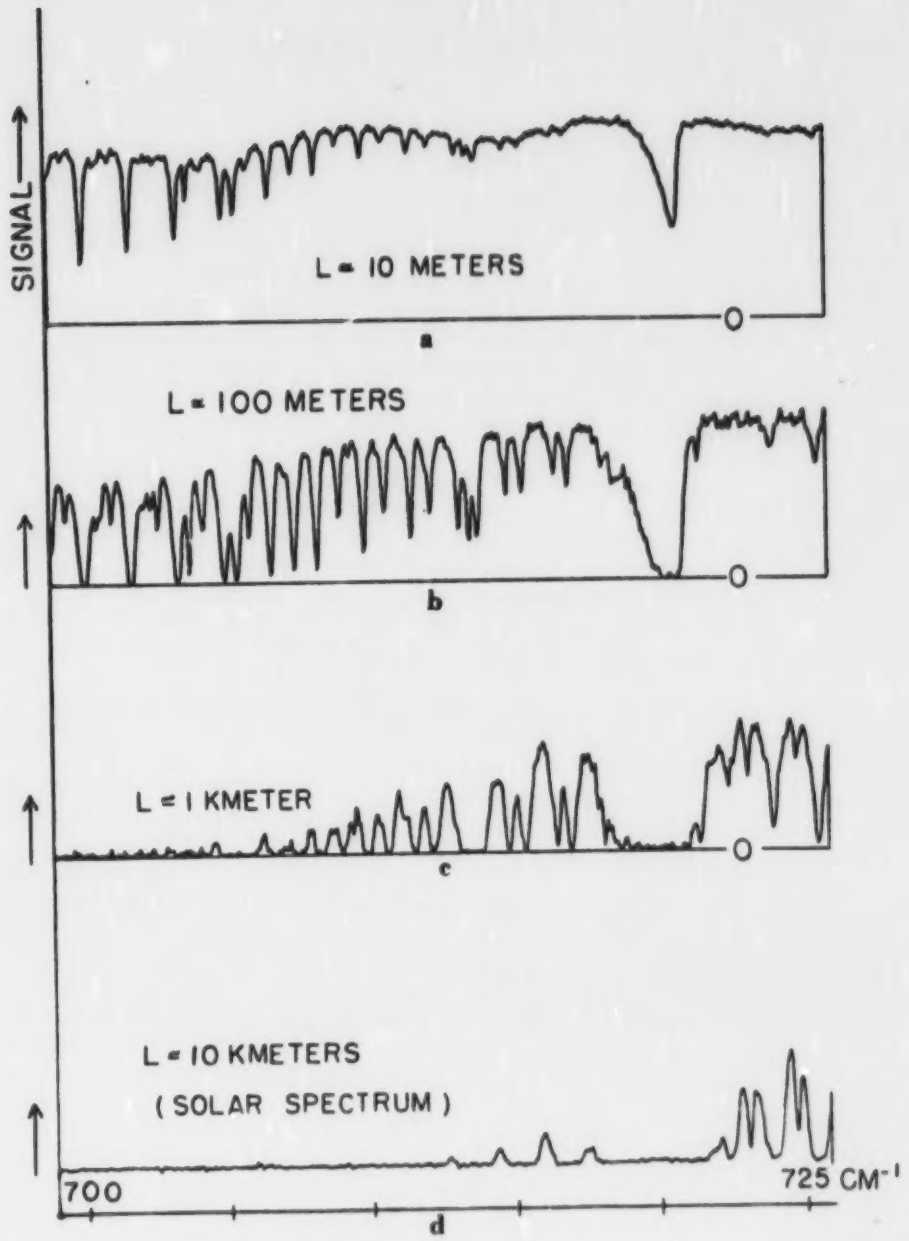


Figure 21. (a) Spectrum of approximately 10 m of air at ambient pressure and temperature, spectral resolution 0.125 $cm^{-1}$; (b) Spectrum of approximately 100 m of air; (c) Spectrum of approximately 1000 m of air; (d) Solar spectrum, solar zenith angle ~ 60°

It is planned to continue adding to this collection and to prepare reports describing the results as appropriate.

## B. STUDY OF THE $NO_2$ - $N_2O_4$ SYSTEM

### 1. Introduction

During the past few years, nitrogen dioxide has become the subject of an increasing number of studies. This interest stems largely from attempts to monitor $NO_2$ effluents in the troposphere and from attempts to follow photochemical processes involving $NO_2$ in the stratosphere.[6]

Laboratory studies of pure $NO_2$, are often compromised by the presence of dinitrogen tetroxide in the sample. This $N_2O_4$ interference can be eliminated either by heating the sample chamber[7,8] to dissociate the $N_2O_4$, or by using extremely low partial pressures of $NO_2$ to reduce the quantity of $N_2O_4$ to a negligible amount. Both of these techniques suffer from possible shortcomings. They force the experimenter to investigate properties of $NO_2$ in a temperature or pressure region which might not be feasible or relevant. For studies of $NO_2$ at temperatures and pressures at which $N_2O_4$ is present, it is necessary to know the equilibrium constant for the association-dissociation reactions $2\ NO_2 \rightleftharpoons N_2O_4$.

The work reported here is the result of preliminary steps of an investigation of gas kinetics involving $NO_2$ and other gases at room temperature, using Fourier transform spectroscopy. The concentrations of the components in a reaction can be monitored by observing their various infrared absorption bands if the spectral information as a function of concentration is known for each reactant and product. For our work, the spectral information which was used to monitor gas concentrations was the peak absorbance of an infrared band of the gas. Measurement of peak absorbance provides an adequate technique for determining concentration if all spectra are recorded at the same resolution.

To obtain a meaningful calibration curve of absorbance versus a wide range of concentration for $NO_2$, it was necessary to record spectra of known concentrations of $NO_2$ under conditions similar to those of an actual kinetic experimental run. Elimination of $N_2O_4$ from the sample gas was not feasible. For these conditions of temperature and pressure (296 K and 2 to 600 Torr) it became apparent that $N_2O_4$ would cause appreciable interference to the calibration of $NO_2$. Thus, it was necessary to know the equilibrium constant for the $NO_2$ - $N_2O_4$ system.

This work reports our results on the determination of this equilibrium constant. Our value for the equilibrium constant is in good agreement with values previously reported, and the emphasis here is on the technique used to investigate the equilibrium. A method has been developed using infrared spectroscopy and two absorption cells of different lengths to study this system at a single temperature. This method is

significantly different from the method of Vosper[9] who reported the use of two absorption cells to study the equilibrium constant. This differs from other methods[10] which rely on data taken at higher temperatures for the evaluation of the equilibrium constant at room temperature.

## 2. Experimental

The apparatus used to measure the equilibrium constant of the $NO_2 + N_2O_4$ system is shown in Fig. 22. Radiant energy from the Nernst glower is collimated and passes through the interferometer. The beam exits the interferometer and passes through one of the two absorption cells. The radiation is then focused on the Cu:Ge detector.

The output from the detector is called the interferogram and is the auto-correlation function of the electric field. This interferogram signal is digitized by the analog-to-digital converter and is stored by the computer. The computer used is a Nova 1200 mini-computer with 4k (4096) words of core and 128k words additional data storage on a fixed head disc. The entire apparatus, including the interferometer, was built by Digilab Inc.

Once the interferogram has been stored in the computer, it is transformed to produce the spectrum. The usable spectral region is defined by the response of the Cu:Ge detector which is from about 400 $cm^{-1}$ to 3500 $cm^{-1}$.

Both absorption cells were constructed of stainless steel and were fitted with sodium chloride windows. The lengths of the cells were $L_1$ = 39.5 cm and $L_2$ = 7.5 cm, which gives a ratio $L_1/L_2$ = 5.27.

The $NO_2$ (+ $N_2O_4$) (nominal purity, 99.5%) was obtained from Matheson Gas Company. The gas was expanded into a gas handling system which was connected to the absorption cells and pressure gauges. The gas handling system was built entirely of glass and stainless steel and is fitted with teflon stopcocks. A line sketch of this apparatus is shown in Fig. 20. The gas was first collected in a liquid nitrogen cooled trap and the volatile gases pumped off. When the cold trap was warmed to room temperature, the sample gas was expanded into an evacuated storage bulb. From this storage bulb, the gas was injected into the two sample cells simultaneously. The pressure of $NO_2 + N_2O_4$ was measured on a calibrated Wallace-Tiernan gauge and a mercury manometer which were isolated from the reactive gas by a glass spiral gauge. Typical sample gas pressures ranged from 2 to 600 Torr.

After the absorption cells were filled to the desired pressure of sample gas, the valves on the cells were closed. The $NO_2 + N_2O_4$ in the glass tubing of the gas handling system was pumped out, and the system was flushed with high purity nitrogen gas. The valves on the absorption cells were again opened and nitrogen was injected into the cells until the total pressure in both cells was 740 Torr. The valves on the cells were finally closed and the two absorption cells were removed from the

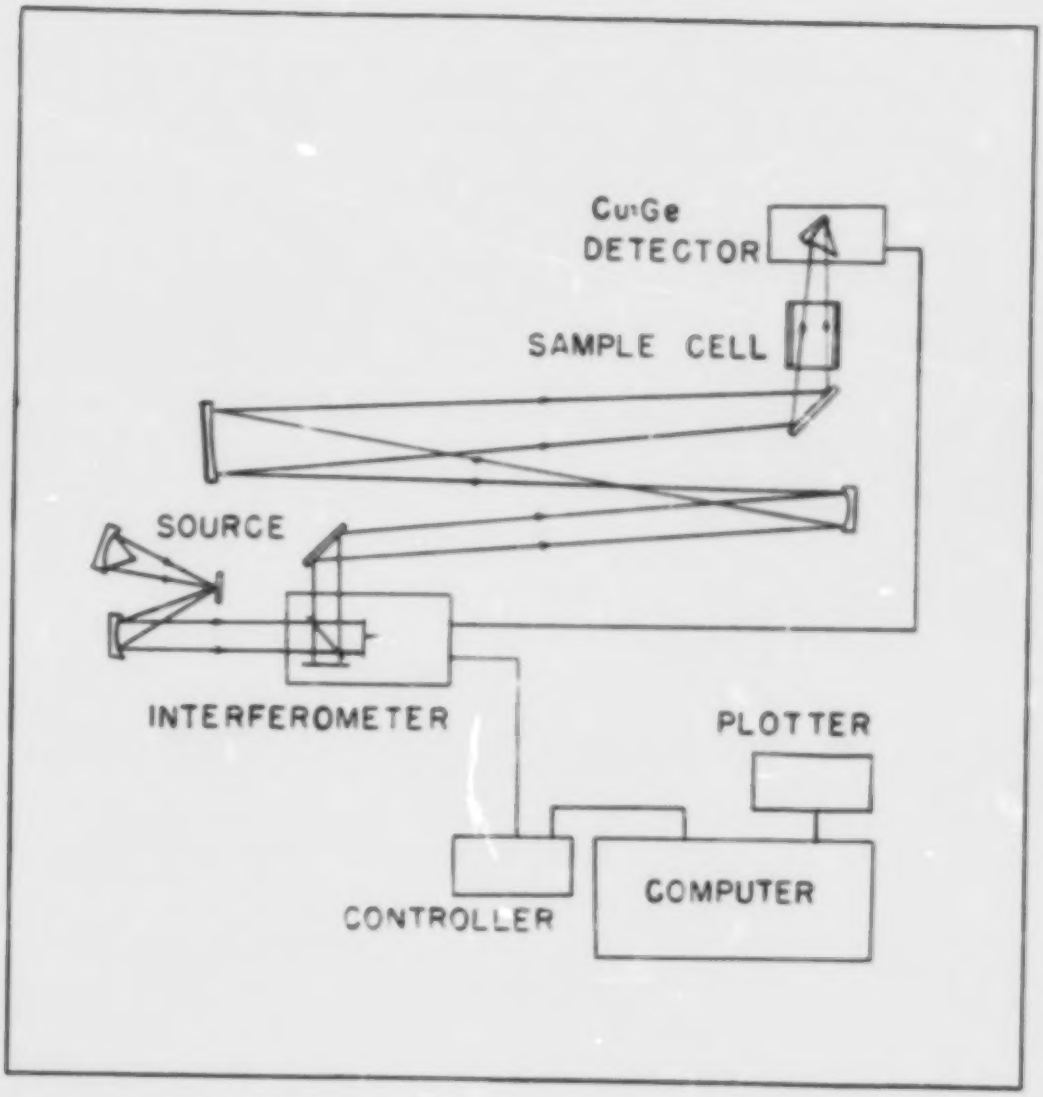


Figure 22. The experimental apparatus. Either of the two absorption cells can be aligned at the indicated position

gas handling system, and each cell in turn was positioned in the optical path.

Single beam spectra were recorded through each cell. All spectra taken through the 39.5 cm cell were ratioed against a background spectrum through the same cell. Similarly, all spectra taken through the 7.5 cm cell were ratioed against a background spectrum recorded through that cell. These two background spectra were prepared by filling each absorption cell to 740 Torr with nitrogen and recording a spectrum through each cell. These background spectra were stored in the computer and could be recalled when needed. This ratioing procedure gave transmission spectra of $NO_2 + N_2O_4$ from which absorbance data could be obtained.

3. Theory

The equilibrium constant for the reactions $N_2O_4 \rightleftharpoons 2NO_2$

$$K = \frac{P^2_{NO_2}}{P_{N_2O_4}} , \tag{19}$$

where $P_{NO_2}$ and $P_{N_2O_4}$ are the partial pressures of the two gases. Expressing the equilibrium constant in terms of the total sample gas pressure

$$P = P_{NO_2} + P_{N_2O_4} , \tag{20}$$

the equilibrium constant can be written

$$K = \frac{P^2_{NO_2}}{P - P_{NO_2}} , \tag{21}$$

The only directly measurable quantity in this expression is the total gas pressure P. The partial pressure of $NO_2$ can be monitored indirectly by infrared absorption measurements.

When infrared radiation passes through a cell of length L which is filled with $NO_2$ to a partial pressure $P_{NO_2}$, the absorbance can be written

$$a_{NO_2}(\nu) = -\ln \frac{I_{NO_2}(\nu)}{I_0(\nu)} = \alpha_{NO_2}(\nu) P_{NO_2} L \tag{22}$$

This equation is referred to as the Beer-Lambert law of absorption of radiation. Here, $a_{NO_2}(\nu)$ is the spectral absorbance due to the presence of $NO_2$, $I_{NO_2}(\nu)/I_0(\nu)$ is the spectral transmittance at frequency $\nu$, and $\alpha_{NO_2}(\nu)$ is the absorption coefficient of $NO_2$.

The use of the Beer-Lambert law is valid when the absorbance, which is the negative of the natural logarithm of the spectral transmittance is proportional to the product of pressure times length. When the product of pressure times length becomes too large, the resulting absorbance is no longer linear with this product. For cells of fixed length, there is an upper limit to the pressure which can be used if the Beer-Lambert law is to apply.

sing two cells of different lengths, the $NO_2$ absorbances at a given frequency $\nu_0$ are equal in the two cells when

$$(a_{NO_2}(\nu_0))_1 = \alpha_{NO_2}(\nu_0)(P_{NO_2})_1 L_1 =$$

$$\alpha_{NO_2}(\nu_0)(P_{NO_2})_2 L_2 = (a_{NO_2}(\nu_0))_2 \qquad (23)$$

where the subscript 1 refers to the first cell and subscript 2 refers to the second cell. From Eq. (23)

$$(P_{NO_2})_1 L_1 = (P_{NO_2})_2 L_2 \qquad (24)$$

When this condition applies, the absorbances in the two cells are equal. If the slight correction due to pressure is ignored,[11] the equilibrium constant for the two cells can be written,

$$K = \frac{(P_{NO_2})_1^2}{P_1 - (P_{NO_2})_1} = \frac{(P_{NO_2})_2^2}{P_2 - (P_{NO_2})_2} \qquad (25)$$

where $P_1$ and $P_2$ are the total pressures of sample gas in cell 1 and cell 2, respectively. Combining Eqs. (24) and (25),

$$(P_{NO_2})_1 = \frac{P_1\sigma^2 - P_2}{\sigma(\sigma - 1)} \qquad (26)$$

where $\sigma = L_1/L_2$. By substituting this equation into the expression for K in Eq. (25),

$$K = \frac{(P_1\sigma)^2 - P_2)^2}{\sigma(\sigma - 1)(P_2 - \sigma P_1)} \qquad (27)$$

Thus, the value of the equilibrium constant K for the $NO_2 \rightleftharpoons N_2O_4$ system can be determined at a single temperature by measuring the total sample gas pressures $P_1$ and $P_2$ in cells of length $L_1$ and $L_2$ which give equal absorbances.

## 4. Results

The infrared absorption band of $NO_2$ which was chosen to study the equilibrium constant expressed in Eq. (27) was the $\nu_2$ band near 13.3 μm. Only the abundant isotope $^{14}N^{16}O_2$ was investigated.[7] This band is partially overlapped by the $\nu_{12}$ band of $N_2O_4$. Figure 23 shows

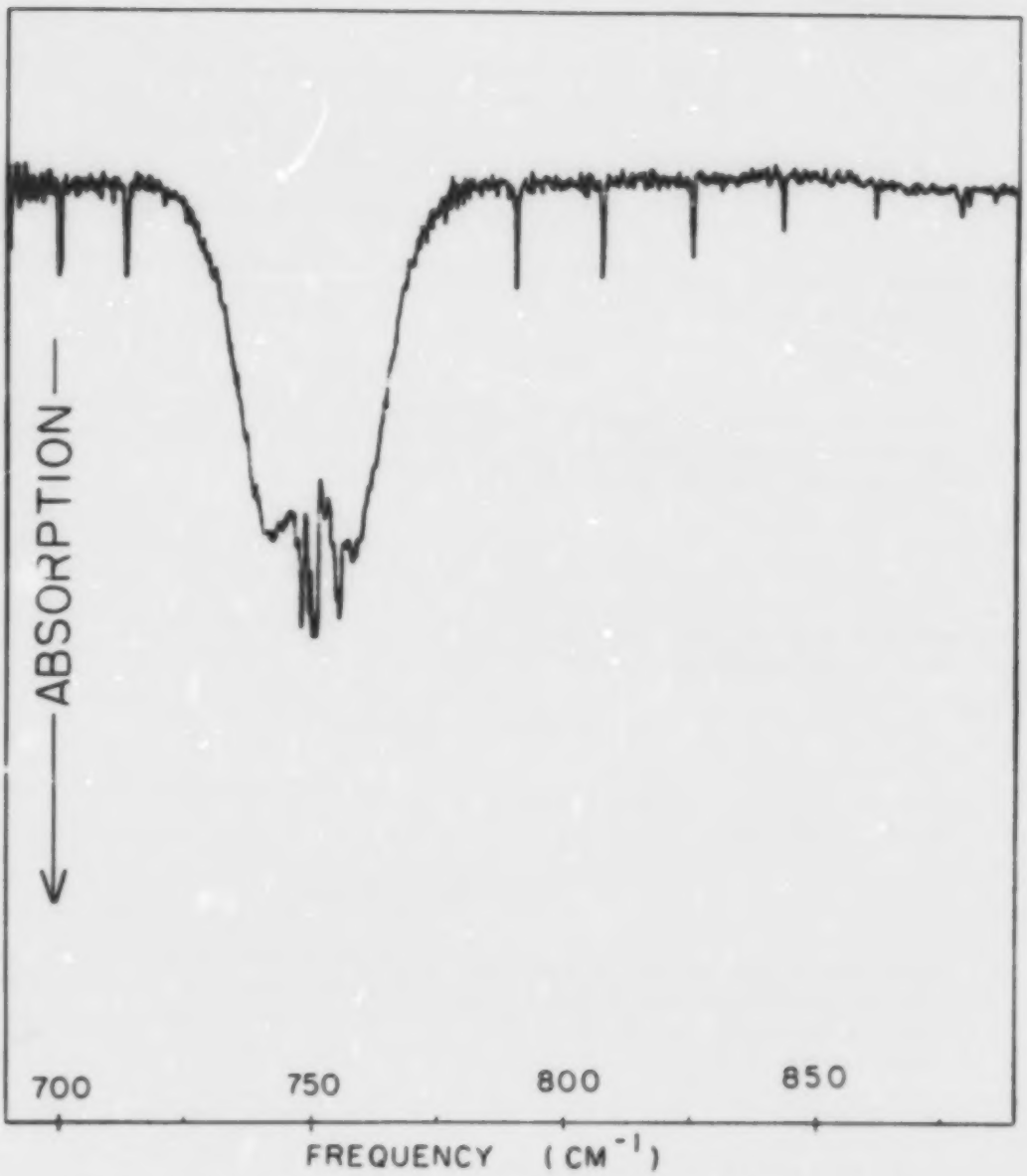


Figure 23. Spectrum of $NO_2 + N_2O_4$ from 700 $cm^{-1}$ to 900 $cm^{-1}$. See text for experimental details

a spectrum of this region recorded through the 7.5 cm cell at a nominal resolution of 0.5 $cm^{-1}$. The pressure of $NO_2 + N_2O_4$ was 12 Torr and the cell was filled with nitrogen to 740 Torr. The regularly spaced absorption spikes are due to $NO_2$ Q-branch transitions, while the broad central feature is mostly due to $N_2O_4$ and partially due to $NO_2$.

All spectra were recorded at 0.5 $cm^{-1}$ resolution. The absorbances at several $NO_2$ Q-branch center frequencies were chosen as monitors of the $NO_2$ concentration. Although peak absorbance in a spectrum is dependent on the resolution used to record the spectrum, nevertheless, the peak absorbance provides an unambiguous measure of concentration if all spectra are recorded at the same resolution.

From the recorded spectra, the absorbances of the $NO_2$ Q-branches near 791 $cm^{-1}$, 807 $cm^{-1}$, and 823 $cm^{-1}$ were measured. Plots of the absorbances as a function of sample gas pressure in both cells were made. Figure 24 shows absorbance plots for the 791 $cm^{-1}$ Q-branch obtained by using the 7.5 cm cell and the 39.5 cm cell. Using these plots and similar plots for the other Q-branch absorbances, a pair of pressures, $P_1$ and $P_2$, can be determined for any chosen absorbance on a particular Q-branch. From these pressures, values of the equilibrium constant were calculated using Eq. (27). A region of linear dependence of absorbance on pressure is not apparent in these plots because the independent variable is the total sample gas pressure, not the $NO_2$ partial pressure. The absorbance values used to calculate the equilibrium constant were chosen to be sufficiently small to assure that we were well within the pressure limits defined by the validity of the Beer-Lambert law for both cells.

Table 1 shows the results of these calculations for the three $NO_2$ Q-branches which were studied. The average of the calculated equilibrium constants is 0.140 atm at 296 K ± 1 K and is in good agreement with values reported previously.

## 5. Conclusions

The results in Table 1 show that the two cell technique provides a reasonable method for the determination of the equilibrium constant for the $NO_2 - N_2O_4$ system. Using the average value of the equilibrium constant determined by this technique, the partial pressure of $NO_2$ can be evaluated for all data points on Fig. 23. Plotting the absorbance versus $P_{NO_2} \cdot L$ for both cells shows a linear dependence of absorbance on the product $P_{NO_2} \cdot L$ as shown in Fig. 25. This linear dependence extends to about 0.3 on the absorbance scale for all Q-branch absorptions which indicates that the data were recorded within the limits of the validity of the Beer-Lambert law.

The major source of experimental error comes from inaccuracies in measuring the pressures $P_1$ and $P_2$. Differentiating Eq. (27) gives

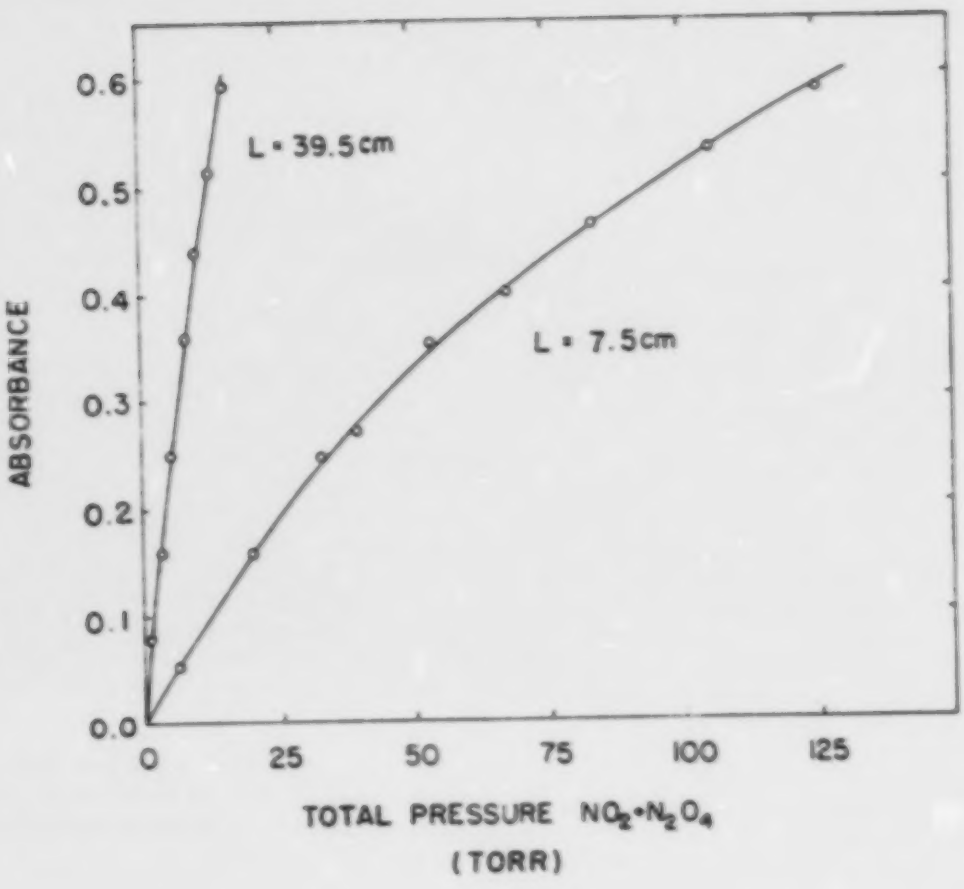


Figure 24. Plots of absorbance of 791 $cm^{-1}$ Q-branch of $NO_2$ as a function of total sample gas pressure in each absorption cell

Table 1. Data for Determination of the Equilibrium Constant for the $NO_2$ - $N_2O_4$ System

| Q-Branch ($cm^{-1}$) | Absorbance | $P_1$ (mmHg) | $P_2$ (mmHg) | K (mmHg) |
|---|---|---|---|---|
| 791 | 0.05 | 1.00 | 5.47 | 111.5 |
| 791 | 0.10 | 2.10 | 12.00 | 102.2 |
| 791 | 0.15 | 3.15 | 18.65 | 102.7 |
| 807 | 0.05 | 1.22 | 6.75 | 102.0 |
| 807 | 0.10 | 2.50 | 14.40 | 109.9 |
| 807 | 0.15 | 3.72 | 22.40 | 104.8 |
| 823 | 0.05 | 1.44 | 8.00 | 110.6 |
| 823 | 0.10 | 2.70 | 15.70 | 106.2 |
| 823 | 0.15 | 3.94 | 23.90 | 103.6 |
| | | | | 105.68 |
| | | | | (0.140 ± 0.020 atm) |

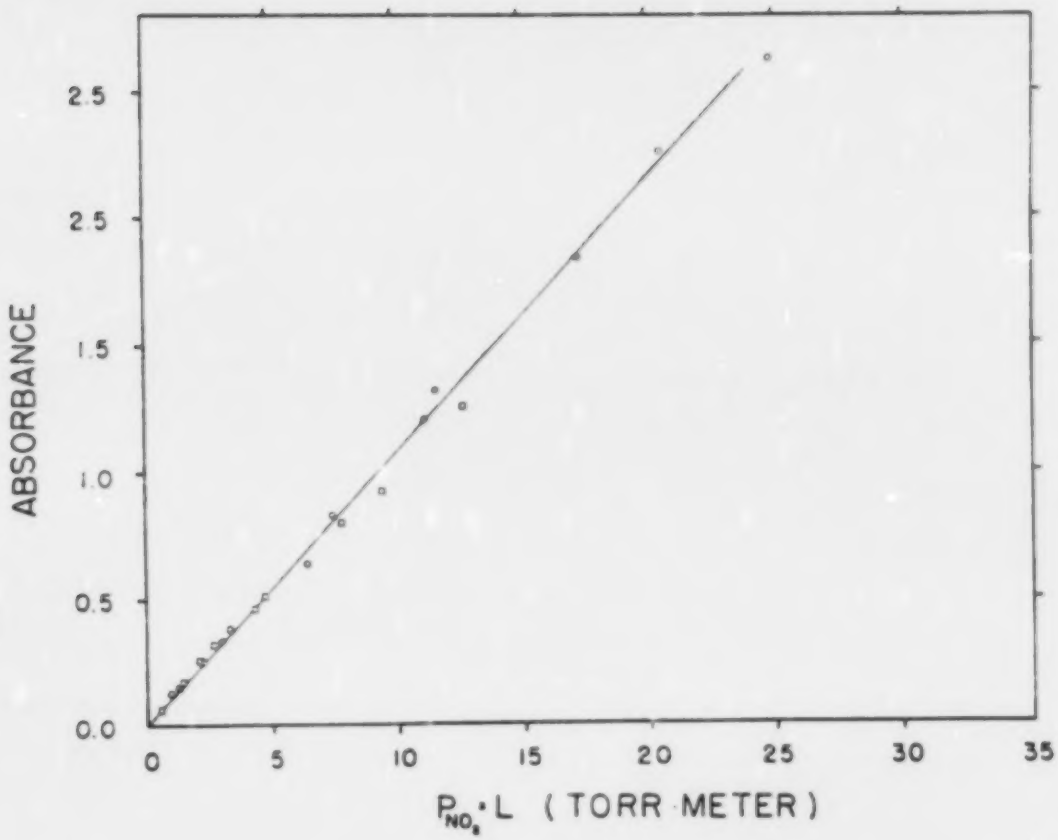


Figure 25. Plot of absorbance of 791 $cm^{-1}$ Q-branch of $NO_2$ as a function of partial pressure of $NO_2$ times path length. The squares represent data taken through the 7.5 cm cell and the circles represent data taken through the 39.5 cm cell

$$\frac{dK}{K} = \frac{\partial K}{\partial P_1}\frac{P_1}{K}\frac{dP_1}{P_1} + \frac{\partial K}{\partial P_2}\frac{P_2}{K}\frac{dP_2}{P_2} \qquad (28)$$

where $dK/K$, $dP_1/P_1$, and $dP_2/P_2$ represent fractional errors in K, $P_1$, and $P_2$, respectively. Using Eq. (27), it is found that

$$\frac{\partial K}{\partial P_1}\frac{P_1}{K} = \frac{\sigma(\sigma - 1)P_1P_2}{(P_2 - \sigma P_1)(P_1\sigma^2 - P_2)} \qquad (29a)$$

and

$$\frac{\partial K}{\partial P_2}\frac{P_2}{K} = -\frac{\sigma(\sigma - 1)P_1P_2}{(P_2 - \sigma P_1)(P_1\sigma^2 - P_2)} \qquad (29b)$$

For the pressures measured in this experiment and $\sigma = 5.27$, these expressions are approximately equal to 10. Thus

$$\frac{dK}{K} = 10\frac{dP_1}{P_1} - 10\frac{dP_2}{P_2} \qquad (30)$$

Our error in measuring the pressure was estimated to be about 1%. Summing the squares of these errors and taking the square root yields a theoretical error of about 15%. Thus, by this technique, we estimate the value of the equilibrium constant for the reactions $N_2O_4 \rightleftharpoons 2NO_2$ at room temperature to be 0.14 ± 0.02 atm.

This result is to be compared with the results of Verhock and Daniels[5] who found K = 0.1426 atm at room temperature using a nonspectroscopic technique which assumed the validity of the ideal gas law. Dunn, Wark, and Agnew[10] used an infrared spectroscopic technique to find K = 0.130 atm at room temperature. Harris and Churney[3] used ultraviolet spectroscopy to study the equilibrium constant at several temperatures. They found K = 0.1624 atm at 299.71 K, which was the closest temperature to our 296 K study.

## C. STUDY OF THE KINETICS AND THE MECHANISM OF THE REACTIONS IN THE GASEOUS SYSTEMS, HONO, NO, $NO_2$, $H_2O$

### 1. Introduction

Many of the general aspects of the mechanism of photochemical smog formation are reasonably well understood today.[11] The chemical transformation of the atmospheric mixture of hydrocarbons, carbon monoxide, and the oxides of nitrogen to the notorious blend of irritants present in photochemical smog, ozone, peroxyacylnitrates, acids, aldehydes, and the other oxidation products of the hydrocarbons, is believed to occur by way of a series of chain reactions which involve various active free radical species as chain carriers. In theory, one of the most important of the active species is the HO-radical. The nitrous acid molecule is one of several potential primary sources of this radical. Nitrous acid may build up in the atmosphere through the occurrence of reactions 1 and 2:

$$NO + NO_2 + H_2O \xrightarrow{k_1} 2HONO \quad (1)$$

$$2HONO \xrightarrow{k_2} NO + NO_2 + H_2O \quad (2)$$

In turn the photolysis of nitrous acid in sunlight may generate HO-radicals:

$$HONO + h\nu(\lambda < 4000\ \text{Å}) \rightarrow HO + NO \quad (31)$$

It is believed that the HO-radical reacts readily with the hydrocarbons (RH), aldehydes (RCHO), carbon monoxide (CO), and other species, to initiate the sequence of reactions which result in the oxidation of NO to $NO_2$ and the ultimate generation of ozone. The HO-radical reaction with each of these types of compounds in the atmosphere leads to the formation of alkyl peroxy ($RO_2$), acyl peroxy ($RCOO_2$) and/or hydroperoxy ($HO_2$) radicals:

$$HO + RH \rightarrow H_2O + R \quad (32)$$

$$R + O_2 \rightarrow RO_2 \quad (33)$$

$$HO + RCHO \rightarrow H_2O + RCO \quad (34)$$

$$RCO + O_2 \rightarrow RCOO_2 \quad (35)$$

$$HO + CO \rightarrow H + CO_2 \quad (36)$$

$$H + O_2\ (+M) \rightarrow HO_2\ (+M) \quad (37)$$

These peroxy radicals are thought to oxidize NO to $NO_2$ and, subsequently regenerate additional HO-radicals:

$$RO_2 + NO \rightarrow RO + NO_2 \quad (38)$$

$$RO + O_2 \rightarrow HO_2 + R'O \quad (39)$$
$$(\text{e.g., } CH_3O + O_2 \rightarrow HO_2 + CH_2O)$$

$$RCOO_2 + NO \rightarrow RCO_2 + NO_2 \quad (40)$$

$$RCO_2 \rightarrow R + CO_2 \quad (41)$$

$$H_2O + NO \rightarrow HO + NO_2 \quad (42)$$

Thus, a single primary HO-radical may initiate a sequence of reactions involving many cycles which may result in the oxidation of several molecules of hydrocarbon, CO, and NO. The oxidation of NO to $NO_2$ is a particularly significant event in that it controls the ozone level through the following reactions:

$$NO_2 + h\nu(\lambda < 4300\ \text{Å}) \rightarrow O(^3P) + NO \quad (43)$$

$$O(^3P) + O_2\ (+M) \rightarrow O_3\ (+M) \quad (44)$$

$$O_3 + NO \rightarrow O_2 + NO_2 \quad (45)$$

The rates of reactions 43-45 are sufficiently fast in a sunlight irradiated atmosphere that a photostationary state of $O_3$ develops which is determined largely by the $[NO_2]/[NO]$ ratio and the solar irradiance in the ultraviolet region effective for reaction 43. Thus, it can be seen that the primary rate of generation of the HO-radical in a polluted atmosphere is an important key to the concentration of ozone, the rate of the generation of the other manifestations of photochemical smog, and the severity of the smog episode.

There has been much speculation on the nature of the primary sources of the HO-radical in the sunlight-irradiated, polluted atmosphere, and it is not clear even today to what extent reactions 1, 2, and 31 generate HO. Although Calvert and McQuigg[12] concluded from smog simulation studies that the nitrous acid molecule is a major primary source of HO through nitrous acid photolysis in sunlight, in their reaction mechanism the major source of HONO was the reaction of $HO_2$ with $NO_2$:

$$HO_2 + NO_2 \rightarrow HONO + O_2 \quad (46)$$

Although the reactions 1 and 2 may in theory also control the nitrous acid levels in the atmosphere, their importance in the atmosphere is uncertain. The existing kinetic information on these reactions apparently does not apply to the homogeneous reactions. In the first detailed study of the $NO$-$NO_2$-$H_2O$-$HONO$ system, Wayne and Yost[13] followed $NO_2$ disappearance in a mixture rich in $NO$ and $H_2O$. The rates were reasonably fast. Leighton[14] derived from these data $k_1 \approx 4.3 \times 10^{-6}$ $ppm^{-2}min^{-1}$, assuming that the kinetics of the reaction followed those of the elementary reaction 1. However, in the subsequent study by Graham and Tyler,[15] much smaller values for $k_1$ were observed: $k_1 \approx (1.2 \pm 0.6) \times 10^{-9}$ $ppm^{-2}min^{-1}$. As in the Wayne and Yost results, the kinetics at high water concentration did not follow the order with respect to the reactants predicted by the elementary step 1. The large difference between the rate constants observed in the two studies was attributed to the large difference in surface-to-volume ratio of the reaction vessels used (factor of 40). Hence, the observed reaction was thought to be controlled entirely by heterogeneous wall reactions. Recently England and Corcoran[16] have invoked the occurrence of reactions 1 and 2 to rationalize their observed kinetic effects of water vapor on the rate of oxidation of $NO$ to $NO_2$ in the $NO$, $NO_2$, $O_2$, $H_2O$ system. They concluded from very indirect evidence that reaction 1 did occur homogeneously at temperatures of 40°C and above with $k_1 \approx 1.5 \times 10^{-8}$ $ppm^{-2}min^{-1}$.

Reaction 2 has not been observed in kinetic studies, but if the homogeneous reaction 1 is slow, as the present evidence suggests, then one

expects the reverse reaction 2 to be slow as well, since the ratio of the two rate constants is equal to the equilibrium constant for reaction 1. Indeed qualitative evidence for the slowness of reaction 2 has been suggested in the studies of Asquith and Tyler,[17] Nash,[18] and Cos and co-workers.[19] They have observed that HONO vapor is seemingly quite stable at concentrations well above its equilibrium level.

All present evidence suggests that the rate constants for the homogeneous reactions 1 and 2 are small, and there is some question as to whether these reactions occur measurably at all in the gas phase. Demerjian, Kerr, and Calvert[11a] also came to this conclusion in their review of the mechanism of photochemical smog formation. However, they noted that if HONO was present in an auto exhaust polluted atmosphere of typical composition at a concentration near those for equilibrium with the NO, $NO_2$, and $H_2O$ present in the early morning hours, the predicted rate of conversion of NO to $NO_2$ would be enhanced by a factor of two over that expected in the absence of HONO. Then it is clearly important to evaluate the rate constants for the homogeneous reactions 1 and 2 in order to define the initial rates of smog formation. Since the heterogeneity of the system was evident in previous studies of the $H_2O$-NO-$NO_2$-HONO system, existing data can give no information as to the desired homogeneous rate constants.

In all of the previous kinetic studies of the nitrous acid system no direct measurement of nitrous acid itself was made. Previous workers depended upon either the determination of changes in visible light absorption due to the reactant $NO_2$ alone, or on chemiluminescence detection of NO and $NO_x$ coupled with the selective chemical removal of HONO vapors. Obviously, rate information based on the direct measurement of HONO vapor is necessary to test the hypotheses formulated from the indirect experiments and to derive meaningful values of $k_1$ and $k_2$. This has been possible in the work described here in which an infrared Fourier transform spectroscopic analysis of the NO, $NO_2$, $H_2O$, HONO system allowed essentially continuous monitoring of all the reactants and products. The relatively large reaction vessel employed in this work ensured a low surface-to-volume ratio and the minimization of wall effects. The cell size and the pressure of added nitrogen gas (700 Torr) favored the homogeneous reaction paths for reactants. The multiple pass White optical system allowed path lengths from 82 m to 1.5 km and measurements of very low reactant and product concentrations in the ppm range of major interest in the atmospheric reactions. We believe that this work provides the first direct measurement of the rate constants of the homogeneous reactions 1 and 2. In terms of these results reasonable speculation is made about the potential role of these reactions in the atmosphere.

## 2. Experimental Methods and Techniques

### a. Reaction vessel and the associated optical system

The reactions between NO, $NO_2$, $H_2O$, HONO mixtures were studied in a large stainless steel (Type 304) tank, 21 m in length and 76 cm in internal diameter. It could be evacuated using its associated Kinney high vacuum booster pump (KMBD) to a pressure of a few microns in about one hour when starting at atmospheric pressure within the cell. The cell housed a White optical system composed of three mirrors (20.5 m radius of curvature) with a base path length of 20.5 m. Two of the mirrors could be adjusted through external controls to allow alignment and variation in the number of optical traversals employed. Path lengths from 82 m up to 1.5 km could be employed. A Digilab FTS 20 system, a Nernst glower, and associated transfer optics provided the infrared beam which entered and exited the cell through NaCl windows. The exit beam was collected by a detector. In this study a liquid helium cooled, copper-doped germanium detector was employed; its useful range extended from 300 to 3500 $cm^{-1}$.

### b. Gas handling system

The gas handling system was constructed from bulbs and tubing made of glass and stainless steel, and all stopcocks were made of Teflon. The introduction of measured quantities of the standard reactant gases, NO and $NO_2$, was accomplished by filling calibrated 1 $\ell$ bulbs to some measured pressure and expanding these into the tank. About a $10^4$ to 1 dilution of reactant concentrations occurred on expansion. Pressures were measured on one of three calibrated Wallace and Tiernan gauges (0-20, 0-50, 0-800 Torr) appropriate for the measurement. The gauges were isolated from the sample by a quartz spiral gauge which was used as a null instrument.

### c. Calibration of reactant gas absorptance data

Although there are several infrared absorption bands characteristic of NO, $NO_2$, and the isomers of HONO in the mid-infrared region, all of them could not be employed for concentration monitoring purposes since some are either overlapping those of atmospheric $CO_2$ and $H_2O$ or they mutually interfere. These interferences were reduced by obtaining all spectra with a spectral resolution of 0.5 $cm^{-1}$. Those unambiguous absorption peaks which were employed in this work are: $NO_2$, $\nu_2$ band, Q-branch transition at 823 $cm^{-1}$; NO, fundamental Q-branch at 1876 $cm^{-1}$; cis-HONO, $\nu_4$ band, Q-branch transition at 853 $cm^{-1}$; trans-HONO, $\nu_3$ band, Q-branch transition at 1264 $cm^{-1}$. All absorbances were measured after adjusting the total pressure of the gaseous mixture to 700 Torr with added nitrogen gas. The single beam spectrometric system employed required that a background spectrum of the detector profile and the cell filled with high purity nitrogen (700 Torr) be recorded first and then ratioed against the sample spectrum. Through the use of this procedure the unwanted interferences from the absorption due to atmospheric water

vapor and $CO_2$ were minimized. Calibration was carried out in three cells of varied path length, 7.5 cm, 39.5 cm, and 20.5 m, respectively. In the case of the reactant nitric oxide (Matheson Co., 99% NO), a measured pressure of the gas was introduced into one of the three cells, and then the mixture was pressurized to 700 Torr with high purity nitrogen. The absorbance at the distinctive Q-branch of NO at 1876 $cm^{-1}$ was then measured. Plots of absorbance versus path length-concentration product were linear over the wide range of concentrations investigated here. The calibration procedure with nitrogen dioxide gas was necessarily more complicated because of the dynamic equilibrium, $2NO_2 \rightleftharpoons N_2O_4$. The $NO_2$-$N_2O_4$ sample (Matheson Co., 99.5% $N_xO_{2x}$) was purified further before use by condensation at liquid $N_2$ temperature and degassed to remove any volatile impurities (NO, $N_2O$, $N_2$, $O_2$, etc.). The degassed sample was then allowed to expand into the desired cell for calibration and the pressure of the $NO_2$-$N_2O_4$ mixture was measured. The corresponding partial pressure of the $NO_2$ gas was then calculated using the known equilibrium constant for the temperature employed (23°C). Again the mixture was pressurized to 700 Torr with added high purity nitrogen gas. The absorbance of the $NO_2$ was measured at the characteristic Q-branch transition at 823 $cm^{-1}$.

The calibration of nitrous acid vapor spectra is complicated because pure samples of HONO vapor cannot be prepared at some desired pressure since it is relatively unstable at concentrations above those corresponding to its rather low equilibrium pressure in NO, $NO_2$, $H_2O$ mixtures. Thus, measurements were made on equilibrium mixtures at 23°C to establish our HONO calibrations. We have calculated the extinction coefficient of the HONO isomers using the known equilibrium ratio of [<u>trans</u>-HONO]/[<u>cis</u>-HONO] = 2.29, and $K_1 = 1.51 \times 10^{-3}$ $ppm^{-1}$ at 25°C (least squares fit of published data),[19,20,21] together with measured absorbances of <u>trans</u>- and <u>cis</u>-HONO, NO, and $NO_2$ in mixtures of known pressure of water vapor. The extinction coefficients ($\epsilon = [\ln(I_0/I)]/pl$) which we have determined and employed in this study (spectral resolution of 0.5 $cm^{-1}$, temp., 23°C) are as follows: NO (1876 $cm^{-1}$), $\epsilon = 0.513 \pm 0.006$ $Torr^{-1}m^{-1}$; $NO_2$ (823 $cm^{-1}$), $0.0807 \pm 0.0012$ $Torr^{-1}m^{-1}$; <u>cis</u>-HONO (853 $cm^{-1}$), $9.36 \pm 0.94$ $Torr^{-1}m^{-1}$; <u>trans</u>-HONO (1264 $cm^{-1}$), $5.20 \pm 0.52$ $Torr^{-1}m^{-1}$.

In kinetic studies of the HONO decomposition reaction, samples of nitrous acid much in excess of the equilibrium pressure were introduced into the large reaction cell following a procedure modified somewhat from that used in the studies of Nash[18] and Cox and co-workers.[17] Three methods were attempted: (1) dilute $H_2SO_4$ was added to dilute $NaNO_2$ solution; (2) dilute $H_2SO_4$ was added to solid $NaNO_2$; and (3) dilute $NaNO_2$ was added to dilute $H_2SO_4$ solution. The third method proved to be the best for our conditions because it gave the maximum ratio of [HONO]/([NO] + [$NO_2$]). The gaseous nitrous acid was produced in the apparatus shown in Fig. 20. A dilute $NaNO_2$ solution (~ 0.3 M) was added slowly to a dilute $H_2SO_4$ solution (~ 2.5 M) by means of the dropping funnel shown. Nitrogen gas was allowed to flow through the entering tube which was directed upward at the solution-gas interface. The

vapors containing HONO were swept into the tubing leading to the cell by the flow of nitrogen gas. The entire apparatus was flushed with nitrogen before use. The trap containing concentrated NaOH solution prevented the entry of air during the preparation and served as a sink for the excess of reactants after HONO preparation. The passage to the NaOH trap was closed by the clamp as HONO was prepared and flushed into the tank.

4. Experimental procedure in absorption

(1) HONO decomposition reaction. Before each run a carefully measured quantity of liquid water was allowed to evaporate and enter the evacuated reaction cell. The transfer was facilitated through the use of a nitrogen carrier gas. Water sufficient to provide in the tank 600-4200 ppm in $H_2O$ concentration was used so that $H_2O$ which was formed in the reactions was always a negligible fraction of the total water present. Then the cell was filled to a pressure of 400-500 Torr of high purity nitrogen gas. During a five-minute period the HONO was added by means of the nitrogen carrier and the apparatus shown in Fig. 20. Finally the passage to the cell was blocked off, and the remainder of the HONO-NO-$NO_2$ mixture was trapped in the concentrated NaOH solution. During a 5-10 minute period, a very fast flow of nitrogen gas was used to mix the gaseous reactants turbulently and to achieve a final pressure of 700 Torr. Spectra were taken (2 min collection period) at regular time intervals (4-10 min), stored on magnetic tape, and the absorption spectra were computed automatically by ratioing against the previously recorded background cell spectrum. In these runs a 246 m path was normally employed. Typical spectra for several time periods can be seen in Fig. 26a. The absorption due to the vibrational transitions of trans-HONO (791 $cm^{-1}$) and cis-HONO (853 $cm^{-1}$) are seen to decrease as the decomposition of HONO occurs, and absorption due to $NO_2$ transitions appear at 823 $cm^{-1}$ and at several other wavelengths between the two HONO $\nu_4$ bands. One $NO_2$ absorption peak overlaps that of trans-HONO so that the 791 $cm^{-1}$ band was not used as a quantitative measure of trans-HONO. The 1264 $cm^{-1}$ absorption band of this isomer showed no such interference and was used for quantitative trans-HONO estimates.
(2) HONO formation reaction. Water was introduced to the evacuated cell as before, then NO gas, followed by $N_2$ gas to bring the total pressure to 400-500 Torr. $NO_2$ was then added and the cell pressurized to 700 Torr with a very rapid flow of nitrogen gas. Spectra were recorded as before, but, in this case, a path of 492 m was employed. Absorbances of NO, $NO_2$, cis-HONO, and trans-HONO were then calculated from plots of the ratioed absorption spectra for each measured time period. Typical absorptance changes in one spectral region can be seen in Fig. 26b. The spike absorptances due to the $NO_2$ Q-branch transitions at 823 $cm^{-1}$ and several other spectral positions occur as prominant features while growth of the trans-HONO and cis-HONO bands is observed at the longer run times.

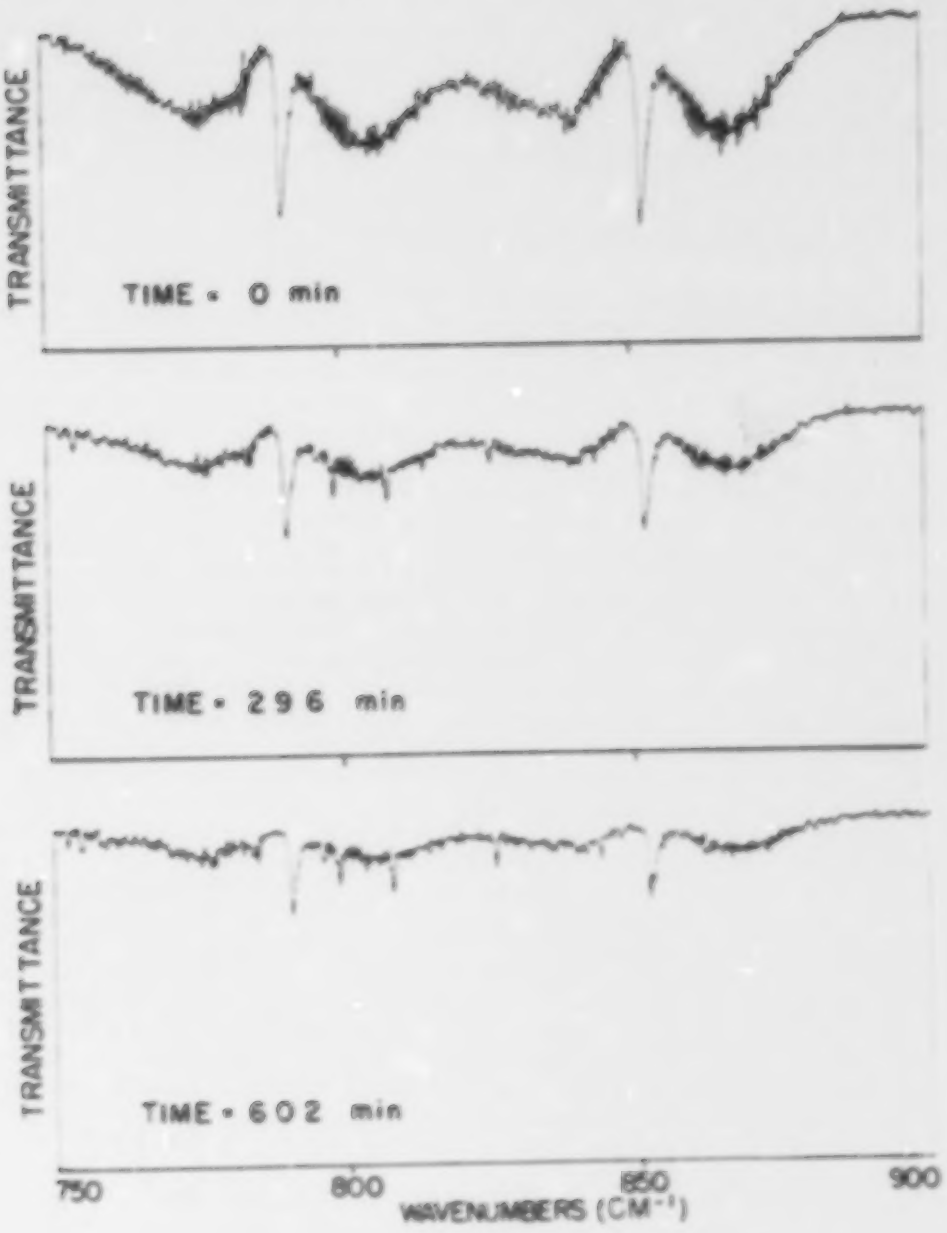


(a)

Figure 26. Absorption spectrum of reacting mixture of HONO, NO, $NO_2$, and $H_2O$; note in (a) decrease in the $\nu_4$ bands of trans-HONO (791 $cm^{-1}$) and cis-HONO (853 $cm^{-1}$) and buildup of $NO_2$ transitions as time progresses in an originally HONO-poor mixture

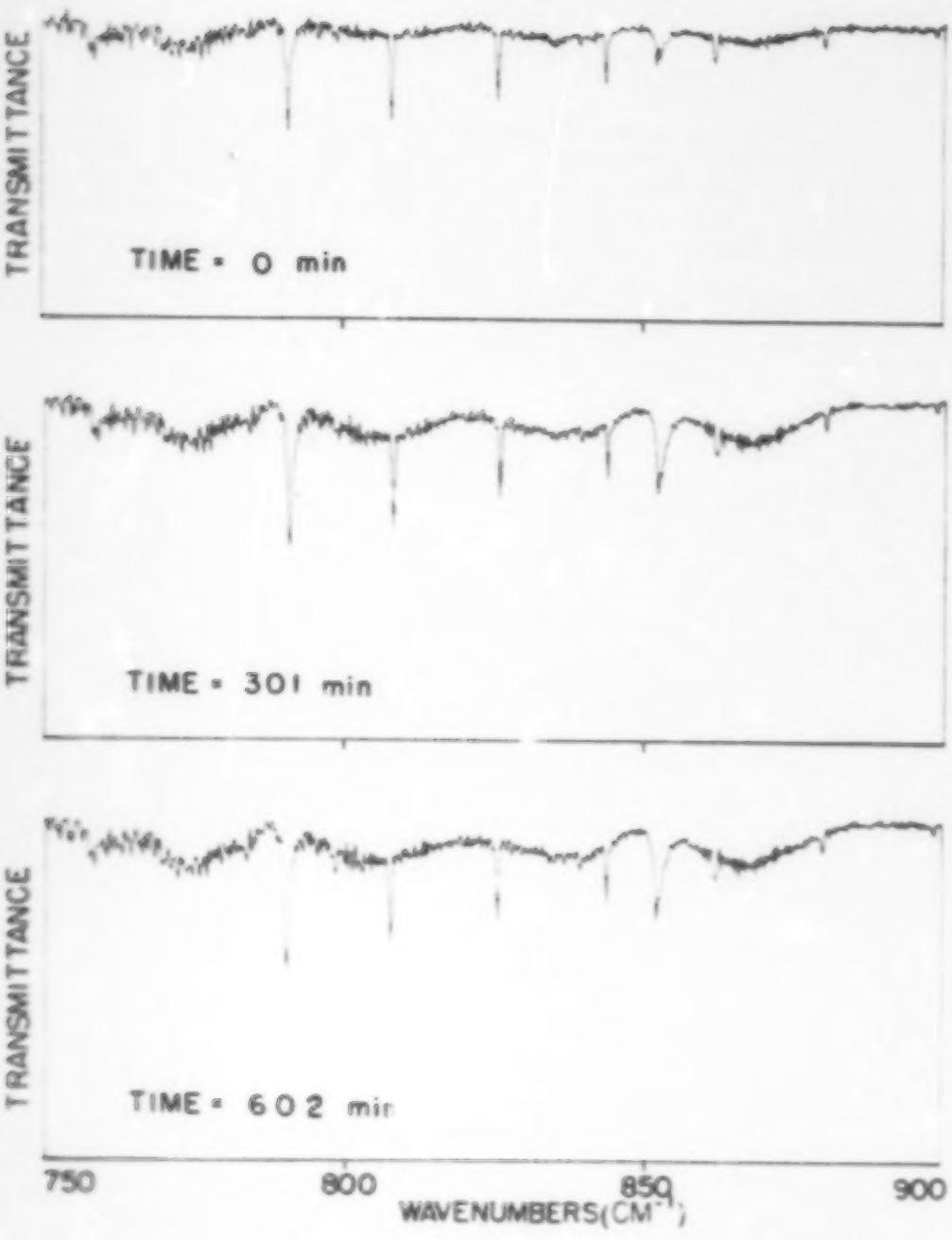


(b)

Figure 26. Continued

## 3. Experimental Results and Discussion

### a. The kinetics of HONO decomposition in the gas phase

In the present work we have introduced gaseous HONO into the reaction cell at concentrations well in excess of its equilibrium values and observed by infrared Fourier transform spectroscopy the kinetics of its return to equilibrium with NO, $NO_2$, and $H_2O$ vapors presumably through the occurrence of reactions 1 and 2.

$$2HONO \rightarrow NO + NO_2 + H_2O \qquad (2)$$

$$NO + NO_2 + H_2O \rightarrow 2HONO \qquad (1)$$

The data given in Fig. 27 show the time dependence of the absorbance measured at the maximum in the Q-branch of the trans-HONO $\nu_3$ band at 1264 $cm^{-1}$ and the cis-HONO $\nu_4$ band at 853 $cm^{-1}$. Note that the two isomers decay essentially in tandem, and, that the rate is very slow; for the concentrations employed here, somewhat less than one-half of the HONO has disappeared in about 200 minutes. The ratio of the two absorbances ($a_{cis}/a_{trans}$) stays nearly constant although it may increase very slightly with time. For example, in the data shown in Fig. 27, the linear least squares fit of the dependence of the absorbance ratio on time follows the equation, $(a_{cis}/a_{trans}) = 0.724 \pm 0.012 + (7.2 \pm 3.8) \times 10^{-5} t(min)$, through 575 min of the reaction. The absorbance ratios noted during the reaction appear to be somewhat lower than those observed for mixtures near equilibrium at room temperature. From 172 different determinations in runs with temperatures from 21.4 to 30.0°C, the average value of $a_{cis}/a_{trans} = 0.790 \pm 0.040$; no significant trend with temperature over this relatively small temperature interval was obtained. Thus there is some suggestion that in the decomposition reaction 2 the cis-HONO isomer is depleted more rapidly than the trans-HONO isomer. However, our data provides no convincing evidence of this; in fact, one would not expect such an effect in theory since the relatively small barrier to isomerization of the HONO isomers, 8.7 ± 1 kcal/mole,[22] should allow equilibration of the isomers to occur very rapidly even if one of the isomers were removed preferentially. Thus, if the isomerization reaction is in the first order region at 700 Torr and it has a "normal" pre-exponential factor ($\sim 10^{13}$ $s^{-1}$), then $t_{1/2} \approx 1.6 \times 10^{-7}$ s at 23°C.

A clue as to the nature of the kinetics of the decay of nitrous acid can be obtained from the plot of $1/a_{cis}$ and $1/a_{trans}$ versus time data for the early times in a typical run shown in Fig. 28. Note that the data follow well a second order decay for both isomers over the time range employed. The least squares slopes of the lines, $(5.03 \pm 0.04) \times 10^{-3}$ and $(3.86 \pm 0.08) \times 10^{-3}$ $min^{-1}$ for the cis- and trans-HONO data, respectively, may be used to derive an estimate of the second order rate constant for total HONO loss.

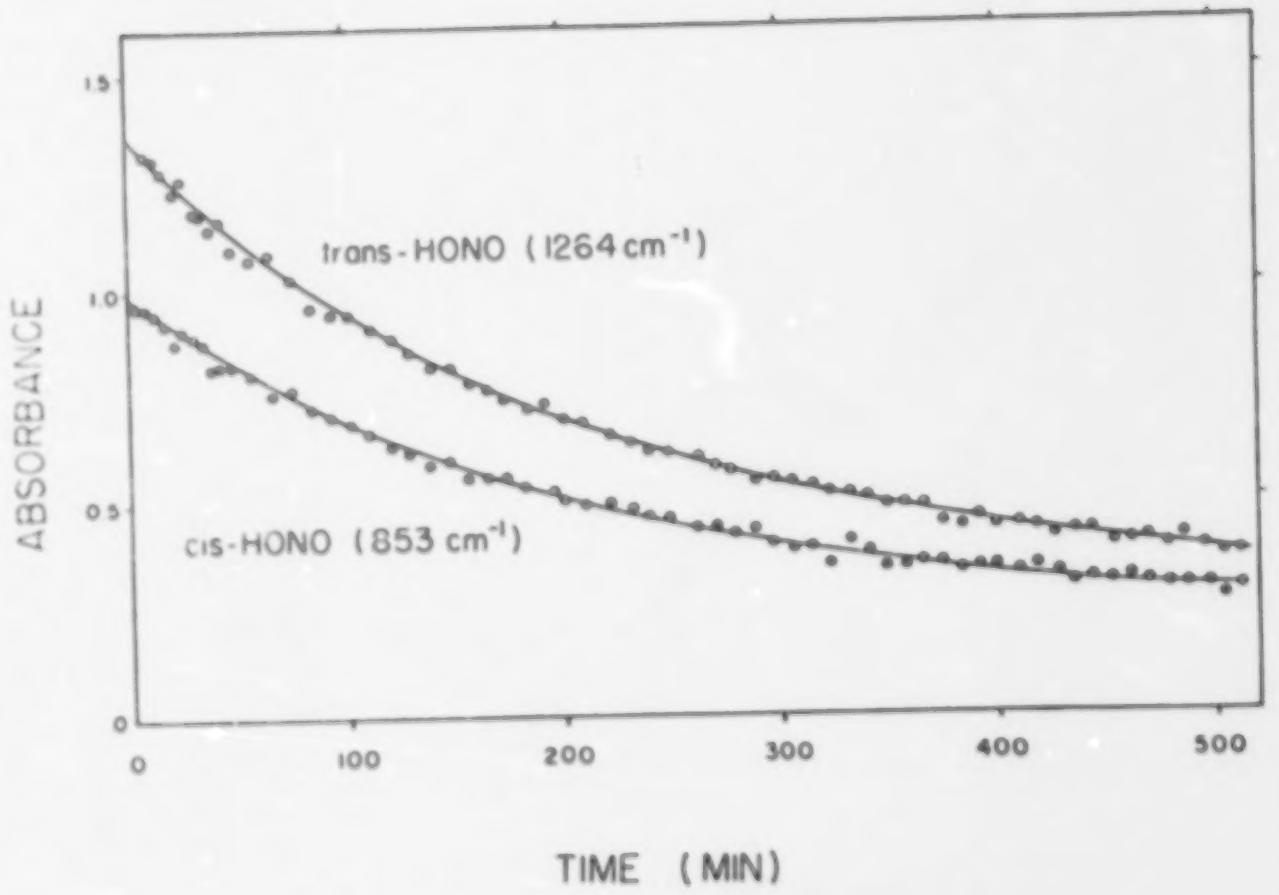


Figure 27. Absorbance versus time plot for the trans-HONO (1264 $cm^{-1}$) and cis-HONO (853 $cm^{-1}$) in a HONO-NO-$NO_2$-$H_2O$ mixture originally rich in HONO

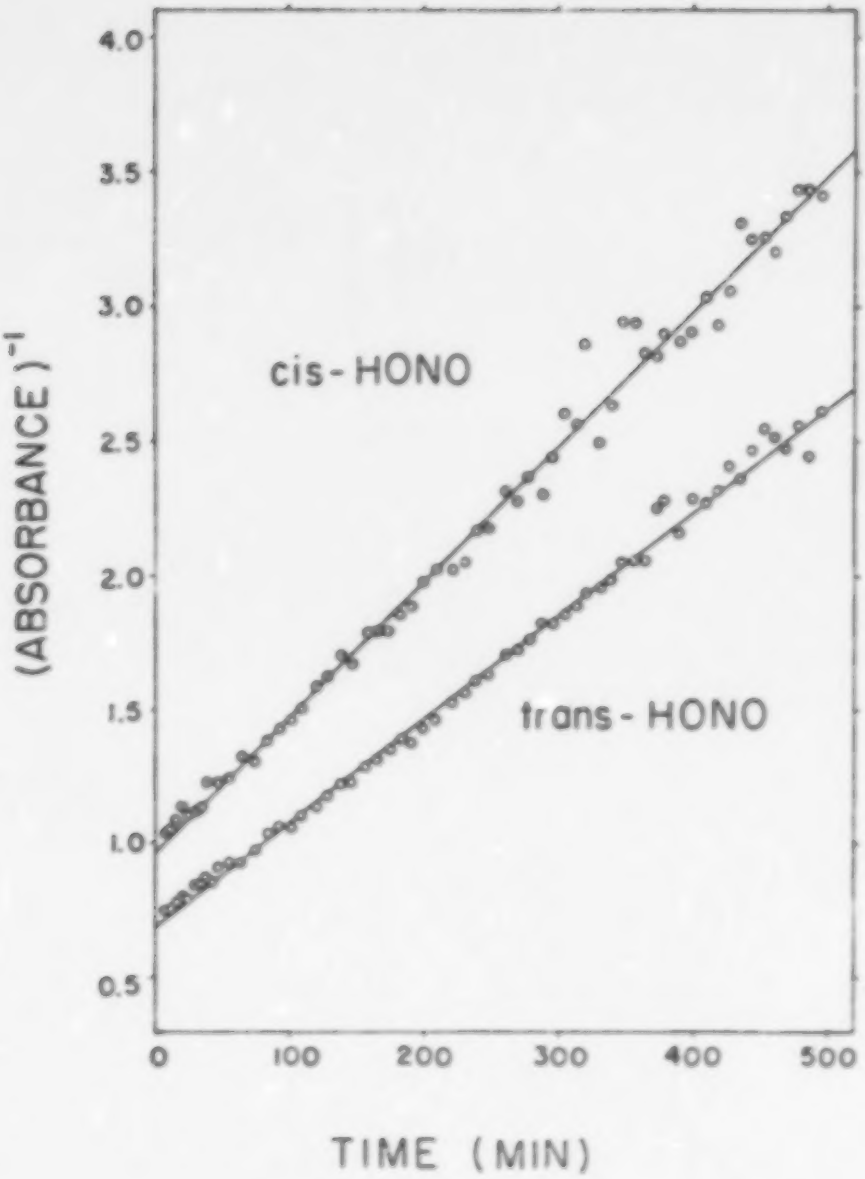


Figure 28. Plot of the reciprocal of the absorbance of trans-HONO (1264 $cm^{-1}$) and cis-HONO (853 $cm^{-1}$) versus time for a HONO-NO-$NO_2$-$H_2O$ mixture originally rich in HONO

$$k_2 = \left(\frac{k_{cis}}{R} + k_{trans}\right)\left(\frac{R}{1+R}\right)^2$$

Here $k_{cis}$ and $k_{trans}$ refer to the apparent second order rate constants observed from the slopes of the cis- and trans-HONO decays, respectively, and R is the equilibrium ratio of [trans-HONO]/[cis-HONO] ≅ 2.29 (23°C). From this procedure we estimate $k_2 = (1.28 \pm 0.06) \times 10^{-3}$ $ppm^{-1}min^{-1}$.

As the reaction proceeds to much longer times the rate of nitrous acid loss decreases until equilibrium levels of HONO, $NO_2$, NO, and $H_2O$ are achieved. This may be noted in the extended run shown in Fig. 29. The total nitrous acid concentration is plotted for a run which extended for over 28 hours. Obviously a nitrous acid forming reaction becomes important at long times. It is reasonable to assume this effect to be the result of the occurrence of reaction 1, the reverse of reaction 2.

$$NO + NO_2 + H_2O \rightarrow 2HONO \qquad (1)$$

If reactions 1 and 2 are the only reactions involving HONO in our system, then the simple rate law which should describe HONO decay over the entire time scale is Eq. (47):

$$-\frac{dP_{HONO}}{dt} = (P_{HONO})^2 2k_2 - P_{NO}P_{NO_2}P_{H_2O}2k_1 \qquad (47)$$

For the conditions employed in our study there is a large excess of water vapor present so that $P_{H_2O}$ remains essentially constant throughout the run. The integrated form of the rate Eq. (47) for the conditions employed may be given by Eq. (48).

$$(P_{HONO})_t = (P_{HONO})_o - \frac{(b+\sqrt{-q})\left(1 - e^{t\sqrt{-q}}\right)}{2c\left\{e^{t\sqrt{-q}} - \frac{b+\sqrt{-q}}{b-\sqrt{-q}}\right\}} \qquad (48)$$

where

$$a = (P_{HONO})_o^2\, 2k_2 - (P_{H_2O})_o(P_{NO_2})_o(P_{NO})_o 2k_1$$

$$b = -\left\{4k_2(P_{HONO})_o + (P_{H_2O})_o\left[(P_{NO_2})_o + (P_{NO})_o\right]k_1\right\}$$

$$c = 2k_2 - (P_{H_2O})_o k_1/2$$

$$q = 4ac - b^2$$

and $P_{HONO}$ refers to the total pressure of nitrous acid present, $P_{trans\text{-}HONO} + P_{cis\text{-}HONO}$. Subscripts of t and o on the reactant pressures refer to time t and 0, respectively. A test of the fit of the data of an extended run of 1648 min duration to the form of Eq. (48) is

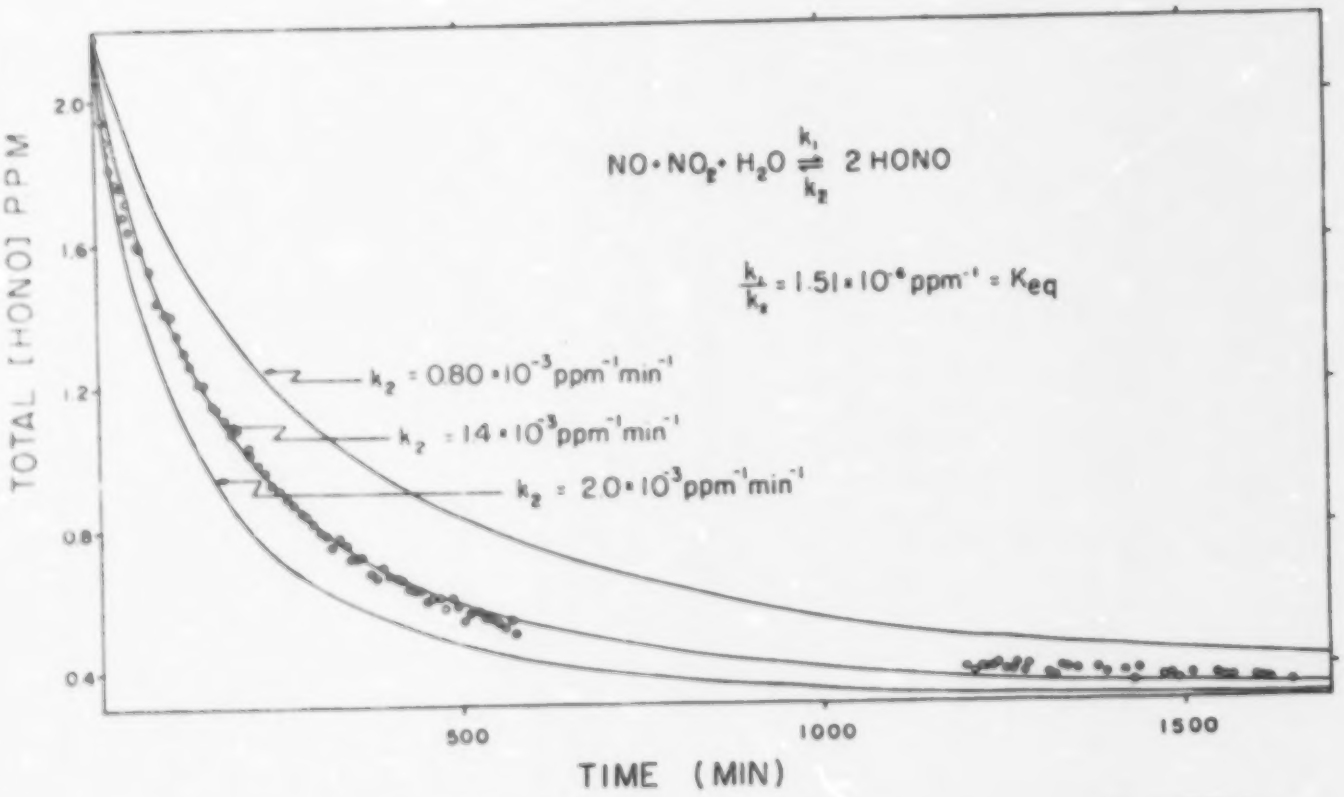


Figure 29. Plot of total HONO concentration versus time for an extended run of 1648 min duration using an initially HONO-rich mixture; initial concentrations, ppm: HONO, 2.14; NO, 2.37; $NO_2$, 3.53; $H_2O$, 4200; temperature, 23°C. Curves shown have been calculated using relation 48 and the rate constant values indicated on the figure.

shown in Fig. 29. In attempting to fit the theoretical time dependence curve to these data and derive rate constant information, we varied the value of $k_2$ chosen for the calculation, but then the choice of $k_1$ was fixed through the known equilibrium constant and its relation to $k_1$ and $k_2$: $k_1 = k_2K_1$; $K_1$ corresponds to the equilibrium: $NO + NO_2 + H_2O \rightleftharpoons 2HONO$. The sensitivity of the fit of the theoretical curve to the choice of $k_2$ may be seen in the figure. For the particular conditions employed in this run a choice of $k_2 = 1.4 \times 10^{-3}$ $ppm^{-1}min^{-1}$, and hence, $k_1 = (1.51 \times 10^{-6})(1.4 \times 10^{-3}) = 2.1 \times 10^{-3}$ $ppm^{-2}min^{-1}$, fits well the data through the Eq. (48) over the entire range of the experiment. This choice of $k_2$ also is in good accord with that derived from the $1/a_{cis}$ and $1/a_{trans}$ versus time plots of the initial rate data as outlined above: $k_2 = (1.3 \pm 0.1) \times 10^{-3}$ $ppm^{-1}min^{-1}$. Similar kinetic constants were obtained from other experiments in which the initial pressures of HONO, $NO_2$, NO, and $H_2O$ were varied and the data were fitted again as outlined. The estimates of $k_2$ and $k_1$ derived from these experiments are summarized in Table 2. There is reasonably good agreement between the estimated constants from the different experiments. Note that the rate constant estimates obtained from runs at 20 Torr and 300 Torr of added nitrogen gas pressure are, within the experimental error, the same as those found in the usual experiments which were pressurized to 700 Torr of nitrogen gas. This supports the conclusion that the rate of HONO disappearance in these runs is controlled by homogeneous reactions and is not influenced significantly by reactions which occur at the cell wall.

This study provides the first measurements of the HONO decomposition reaction. The data seem to suggest that HONO decay occurs by the stoichiometry required by the elementary reaction 2 with a rate constant $k_2 = (1.4 \pm 0.4) \times 10^{-3}$ $ppm^{-1}min^{-1}$ at $23 \pm 1°C$. The fit of these rate data to the decay at long times gives $k_1 = (2.1 \pm 0.7) \times 10^{-3}$ $ppm^{-2}min^{-1}$ at $23 \pm 1°C$.

b. <u>The kinetics of the HONO formation reaction in the gas phase</u>

Evidence of the kinetics which control reaction $H_2O + NO + NO_2 \rightarrow 2HONO$, is derived from the dependence of the rate of HONO decay over the long times during which equilibrium is approached; values of $k_1$ were obtained from the type of kinetic data in the previous section. An attempt was made to determine $k_1$ in more direct experiments in which NO, $NO_2$ and $H_2O$ were added to the cell and the rate of HONO formation was observed. This reaction proved to be much more difficult to observe quantitatively in our apparatus than the study of reaction 2. The difficulty arose primarily in making up the original $NO_2$, NO, and $H_2O$ dilute mixture in the cell without allowing the reactants to encounter one another prematurely at elevated concentrations. In general, we were successful in preparing mixtures which were only a factor of two or three from the equilibrium level of HONO, so the data are less useful than we had hoped. One set of data from an experiment of this type is shown in

Table 2. Summary of the Rate Constant Estimates[a] for the Reactions:

$$NO + NO_2 + H_2O \rightarrow 2HONO \quad (1)$$

$$2HONO \rightarrow NO + NO_2 + H_2O \quad (2)$$

| Initial concentrations, ppm[b] | | | | | | |
|---|---|---|---|---|---|---|
| [NO] | [$NO_2$] | [$H_2O$] | [HONO] | $P_{N_2}$, Torr | $k_2$, $ppm^{-1}min^{-1}$ | $k_1$, $ppm^{-2}min^{-1}$ |
| a) $2HONO \rightarrow NO + NO_2 + H_2O$ Experiments | | | | | | |
| 5.42 | 7.81 | 560 | 6.73 | 700 | $1.6 \times 10^{-3}$ | $2.4 \times 10^{-3}$ |
| 5.65 | 7.01 | 1120 | 6.04 | 700 | $1.6 \times 10^{-3}$ | $2.4 \times 10^{-3}$ |
| 4.64 | 5.60 | 2240 | 5.21 | 700 | $1.4 \times 10^{-3}$ | $2.1 \times 10^{-3}$ |
| 5.18 | 4.89 | 2800 | 3.95 | 700 | $0.90 \times 10^{-3}$ | $1.4 \times 10^{-3}$ |
| 2.37 | 3.53 | 4200 | 2.14 | 700 | $1.4 \times 10^{-3}$ | $2.1 \times 10^{-3}$ |
| 4.23 | 8.50 | 190 | 9.01 | 300 | $1.5 \times 10^{-3}$[c] | $2.3 \times 10^{-3}$[c] |
| 1.91 | 10.7 | 190 | 4.77 | 20 | $2.3 \times 10^{-3}$[c] | $3.5 \times 10^{-3}$[c] |
| b) $NO + NO_2 + H_2O \rightarrow 2HONO$ Experiments | | | | | | |
| 15.8 | 8.16 | 1400 | 0.130 | 700 | $0.80 \times 10^{-3}$ | $1.2 \times 10^{-3}$ |
| 10.6 | 9.72 | 2240 | 0.141 | 700 | $1.4 \times 10^{-3}$ | $2.1 \times 10^{-3}$ |
| | | | | Best Estimates: | $(1.4 \pm 0.4) \times 10^{-3}$ | $(2.2 \pm 0.7) \times 10^{-3}$ |

[a]Temperature in all runs, 23 ± 1°C.

[b]The unit ppm used here is defined as [pressure(Torr)/760] x $10^6$ at 23°C.

[c]Calculated assuming there is no pressure dependence in the extinction coefficient of the Q-branch of the vibrational bands used for concentration estimation; this appears to be a good approximation from a limited study of the effect of pressure on the absorbance of the species involved here.

Fig. 30. Again an attempt was made to match the concentration versus time profile for HONO formation using the rate equation given by Eq. (48). The fits using various values for $k_1$ are shown. In this case $k_2$ was adjusted so that $k_2 = k_1/K_1$. The estimated rate constants from two such runs are given in Table 2, Section B. Although our precision is low for these experiments, we conclude that the same rate constants derived in the study of reaction 2 fit the reverse reaction kinetics reasonably well; the best estimate from all of the data gives $k_1 = (2.2 \pm 0.7) \times 10^{-3}$ ppm$^{-2}$min$^{-1}$. Reaction 1 has been studied previously and the results of these studies should be reviewed here in light of our new findings.

The Graham and Tyler[15] kinetic data for reaction 1 were derived from experiments over a wide range of reactant concentrations: $P_{NO} = 4.3$-200 Torr; $P_{NO_2} = 1.7$-7.5 Torr; $P_{H_2O} = 4.7$-14 Torr. Although these results seem to show an enhanced rate of reaction for runs at $P_{H_2O} > 9$ Torr, which suggests an order for $H_2O$ higher than one, the calculated third order rate constants for the reaction 1 for $P_{H_2O} < 9$ Torr appear to be reasonable constant over the wide range of reactant concentrations employed. Indeed it is interesting to observe that the average value of the third order rate constant $k_1$ derived from the Graham and Tyler data, $k_1 = (1.2 \pm 0.6) \times 10^{-3}$ ppm$^{-2}$ min$^{-1}$, is equal, within the experimental uncertainties of the two very different measurements, to that observed here: $k_1 = (2.2 \pm 0.7) \times 10^{-3}$ ppm$^{-2}$min$^{-1}$. Since the surface-to-volume ratio of the reaction vessel in our study was much lower than that of Graham and Tyler (0.052 cm$^{-1}$ compared to 1 cm$^{-1}$) and the concentration ranges of all of the reactants were several orders of magnitude lower in our work, the degree of agreement observed from the two very different systems provides strong evidence that the rate constant observed here is indeed that for a homogeneous reaction. Apparently the data of Graham and Tyler also may apply to the homogeneous system, at least at the lower $H_2O$ pressures.

c. Mechanism of the nitrous acid formation and decay reactions

In most previous work the mechanism of the nitrous acid formation reaction has been considered to be the following:

$$NO_2 + NO \rightleftharpoons N_2O_3 \qquad (49)$$

$$N_2O_3 + H_2O \rightarrow 2HONO \qquad (50)$$

Since the equilibrium 49 is established rather rapidly,[1,22,23] the occurrence of this mechanism would be consistent with the overall kinetics of nitrous acid formation observed here and in the work of Graham and Tyler. The rate of nitrous acid formation would be given by Eq. (51)

$$-\frac{dP_{HONO}}{dt} = 2k_2K_1P_{NO}P_{NO_2}P_{H_2O} \qquad (51)$$

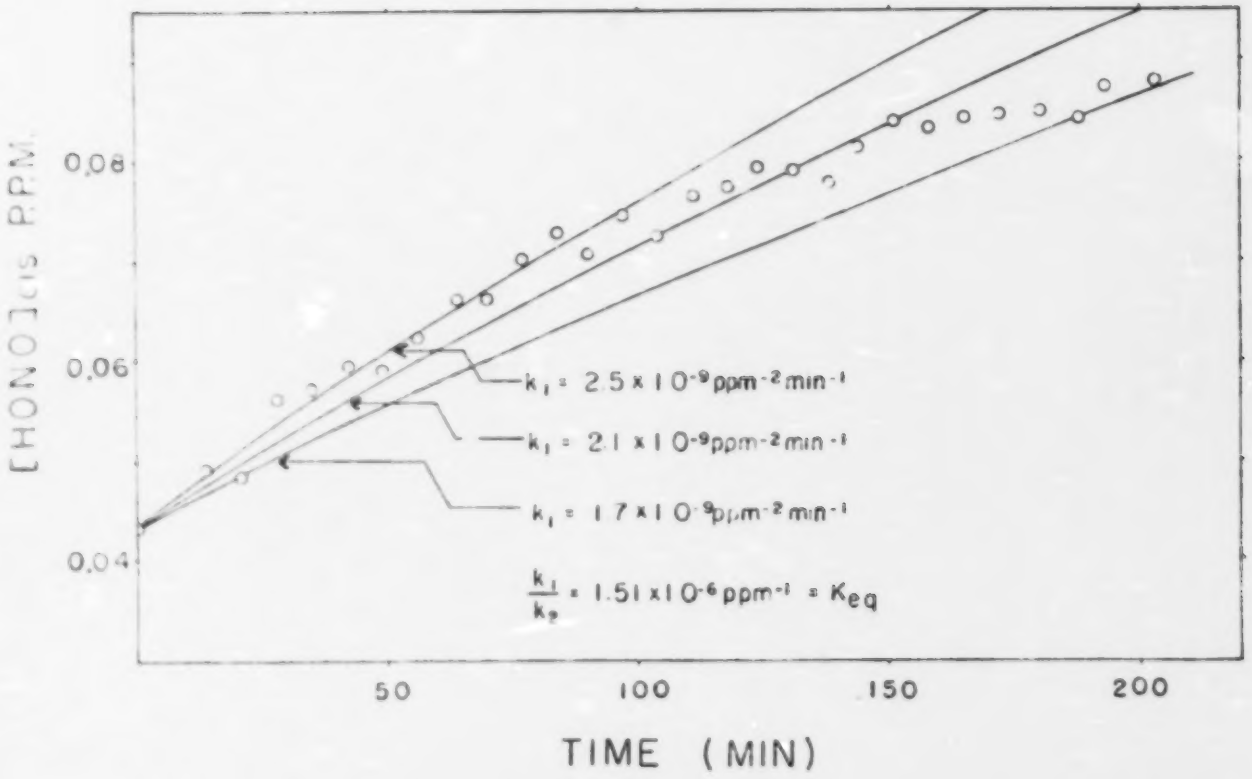


Figure 30. Plot of cis-HONO concentration versus time using an initially HONO-poor mixture; initial concentrations, ppm: HONO, 0.141; NO, 10.6; $NO_2$, 9.72; $H_2O$, 2240; temperature, 23°C. Curves shown have been calculated using relation 48 and the rate constant values indicated on the figure.

The value for $K_{21}$ is $5.2 \times 10^{-7}$ $ppm^{-1}$ at 25°C.[25] Thus in terms of the mechanism 49, 50 for HONO formation and the present value for $k_1$, $k_{22} \geq 4.2 \times 10^{-3}$ $ppm^{-1}min^{-1}$. The transition state for this hypothetical route of reaction would, in theory, involve a rather complex transition state:

$$N_2O_3 + H_2O \approx \text{[cyclic transition state]} \approx 2HONO \qquad (52)$$

The pre-exponential A-factor for such a highly ordered transition state required for the hypothetical reaction 52 should be much lower than the bimolecular collision number. If the activation energy for reaction 50 is near zero ($\Delta H_{298} \geq 0.6$ kcal), then, in a sense, the $N_2O_3$ involvement could be justified in terms of the present kinetic data. However, if one considers the reverse reaction 2 and the requirement that the same transition state be involved as in reaction 1, then the kinetic data definitely favor an alternative reaction scheme.

A seemingly more realistic mechanism for the reactions 1 and 2 involves a much simpler transition state:

$$NO + NO_2 + H_2O \approx \text{[cyclic transition state]} \approx 2HONO \qquad (53)$$

Here the transition state involves formation of only one common H-atom bond between the reactants. Note the similarity between this reaction pathway and that proposed for the ternary reaction of NO oxidation and its reverse bimolecular reaction:[26-27]

$$NO + NO + O_2 \approx \text{[cyclic transition state]} \approx 2NO_2 \qquad (54)$$

The entropy of activation for reaction 54 should be very similar to that for 53 so one might expect very similar pre-exponential factors for the two reactions. The activation energy of reaction 2 is not known so we cannot estimate directly the experimental A-factor for this reaction; $\Delta H_{298}$ for the reaction is about -9.5 kcal. The measured rate constant for the forward reaction 54, $k_{54} = 1.43 \times 10^{-1}$ $ppm^{-2}$ $min^{-1}$,[27] is very nearly equal to that observed for the reaction 1; $k_1 = (2.2 \pm 0.7) \times 10^{-1}$ $ppm^{-2}$ $min^{-1}$. The similarity in transition states of reactions 53

and 54, and hence pre-exponential factors, coupled with the similarity in rate constants, leads one to conclude that $E_4$ may be near zero as with $E_{-4}$. Thus, we may estimate $E_4 \approx 0.5$ kcal and $A_4 \approx 1.3 \times 10^{11}$ ppm$^{-1}$min$^{-1}$. This value is the approximate magnitude of the pre-exponential factor for the bimolecular reaction given by the reverse of reaction 54 which has a very similar transition state: $A_{-54} = 1.0 \times 10^{11}$ ppm$^{-1}$min$^{-1}$.[38]

All of the present data seem consistent with the simple mechanism outlined in Eq. (54) as a description of reactions 1 and 2. The involvement of $N_2O_3$ as an intermediate in the reaction seems unnecessary. The activation energy assignments made here may be tested with the limited temperature variation studies described in the following section.

d. Equilibrium studies and the temperature dependence of the nitrous acid formation and decay reactions

The effect of temperature on the rate of the HONO decay reaction could not be determined accurately with the large reaction vessel employed in this work since the tank has no special temperature control other than the air conditioning system for the laboratory in which it was housed. This air control system was used in a series of runs designed to determine the equilibrium constant and rates of [HONO] change with temperature. Typical data for one of the mixtures studied is shown in Fig. 31. The tank contained a mixture of NO, $NO_2$, $H_2O$, and HONO at equilibrium. The air conditioner was turned off in the morning hours, and the temperatures of the room and the tank housed therein were allowed to rise during the day as the outside temperature climbed. The infrared spectra of the reactants and the temperature at the center of the tank were monitored at regular intervals. Note in Fig. 31 that the nitrous acid pressure versus time plot mirrors the temperature-time variation within the cell; the nitrous acid is depleted as the temperature rises and the system attempts to reestablish equilibrium as a shift away from the exothermic direction of the equilibrium position occurs: $2HONO \rightleftharpoons NO + NO_2 + H_2O$. After the system had reached a desired temperature, the air conditioner was turned on again, and the temperatures of the room and the cell were lowered while the monitoring continued. At about 620 minutes after the start of the experiment shown in Fig. 31, the rate of change of nitrous acid became equal to zero; at this time the values of $P_{NO}$, $P_{NO_2}$, $P_{H_2O}$, $P_{cis\text{-}HONO}$, and $P_{trans\text{-}HONO}$ correspond to those for equilibrium at the particular cell temperature recorded for this time (29.8°C in Fig. 31). From a series of such temperature drift data in which the $d[HONO]/dt = 0$ was caused to occur at a series of different temperatures, we were able to estimate the equilibrium constant for the NO, $NO_2$, $H_2O$, HONO system at several temperatures. These data are given in Table 3 and refer to the equilibrium, $NO + NO_2 + H_2O \rightleftharpoons 2HONO$. The data are reasonably consistent with equilibrium data derived from previous indirect measurements in which only $NO_2$ concentrations were monitored and a mass balance assumption was made. All of the data are plotted in Fig. 32. A least squares fit of the previous equilibrium data for the HONO, $H_2O$, NO, $NO_2$ system[1, 2, 3] gives the equation,

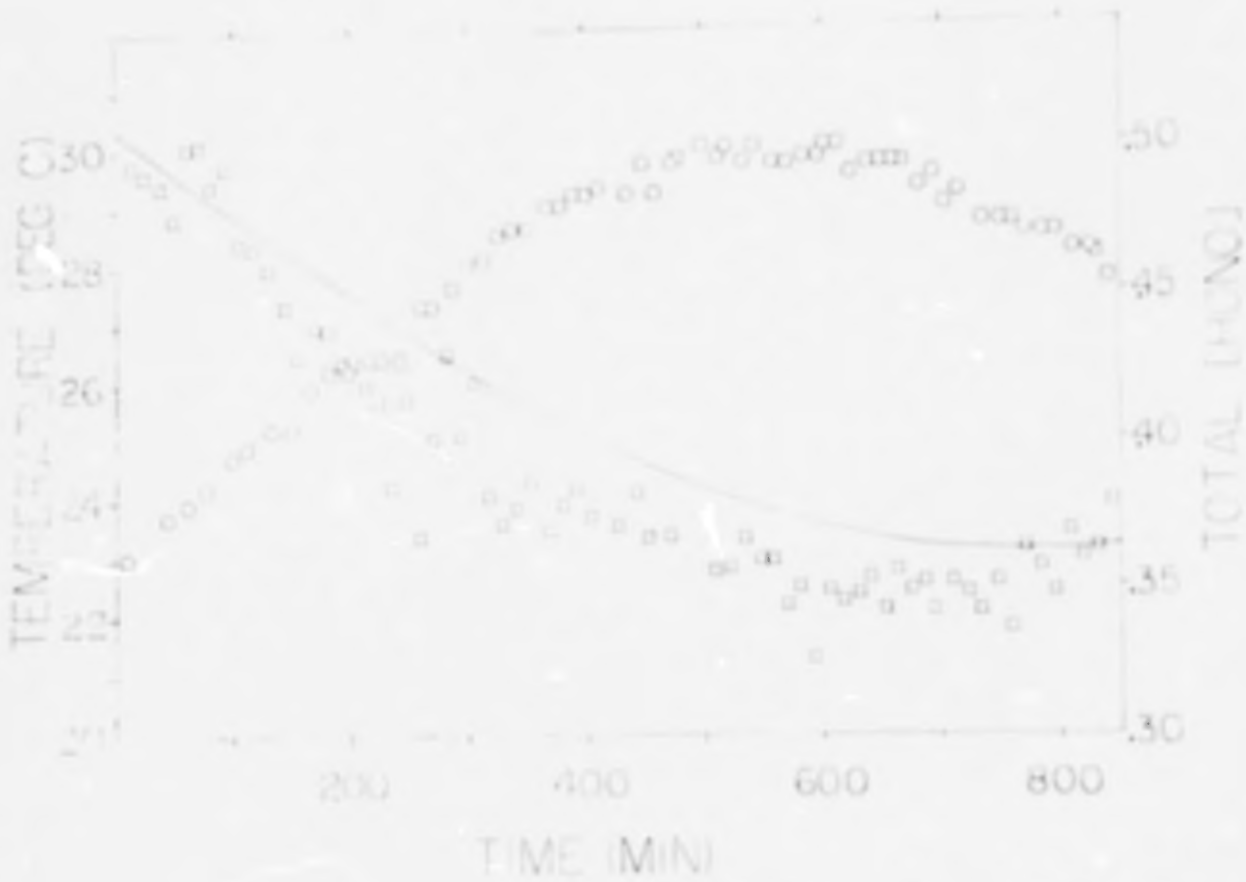


Figure 31. Plot of [HONO] and temperature within the reaction cell versus time for an HONO-NO-$NO_2$-$H_2O$ mixture near equilibrium; typical data used to determine the equilibrium constant for the reaction, NO + $NO_2$ + $H_2O$ ⇌ 2HONO, and to provide a qualitative test of the temperature dependence to the rate constants

Table 1. Equilibrium Data Derived from the Temperature Drift Experiments

$$N_2O_4 \rightleftharpoons 2NO_2 \qquad (1)$$

Conditions at 0.030 atm, 21 mmHg, 298 K

| Temp., K | $N_2O_4$ | $NO_2$ | $K_{298}$ | $K_1$, ppm | $K_1$, atm$^{-1}$ |
|---|---|---|---|---|---|
| 295.3 | 9.25 | 14.5 | 0.639 | 1321 | 1.04 |
| 295.1 | 9.27 | 14.5 | 0.642 | 1323 | 1.05 |
| 295.6 | 8.74 | 7.00 | 0.350 | 420 | 1.52 |
| 296.9 | 14.0 | 23.3 | 0.634 | 921 | 1.35 |
| 297.0 | 8.77 | 14.21 | 0.507 | 1025 | 1.41 |
| 297.9 | 9.30 | 14.54 | 0.470 | 1335 | 1.22 |
| 299.7 | 9.49 | 13.6 | 0.405 | 901 | 1.49 |
| 300.1 | 7.96 | 14.0 | 0.404 | 1301 | 1.09 |
| 303.0 | 7.40 | 10.2 | 0.347 | 1314 | 0.904 |
| 303.1 | 9.29 | 12.7 | 0.355 | 931 | 1.15 |

[a] The unit ppm used here is defined as [pressure (torr)/760] x $10^6$ at the temperature shown for the particular experiments.

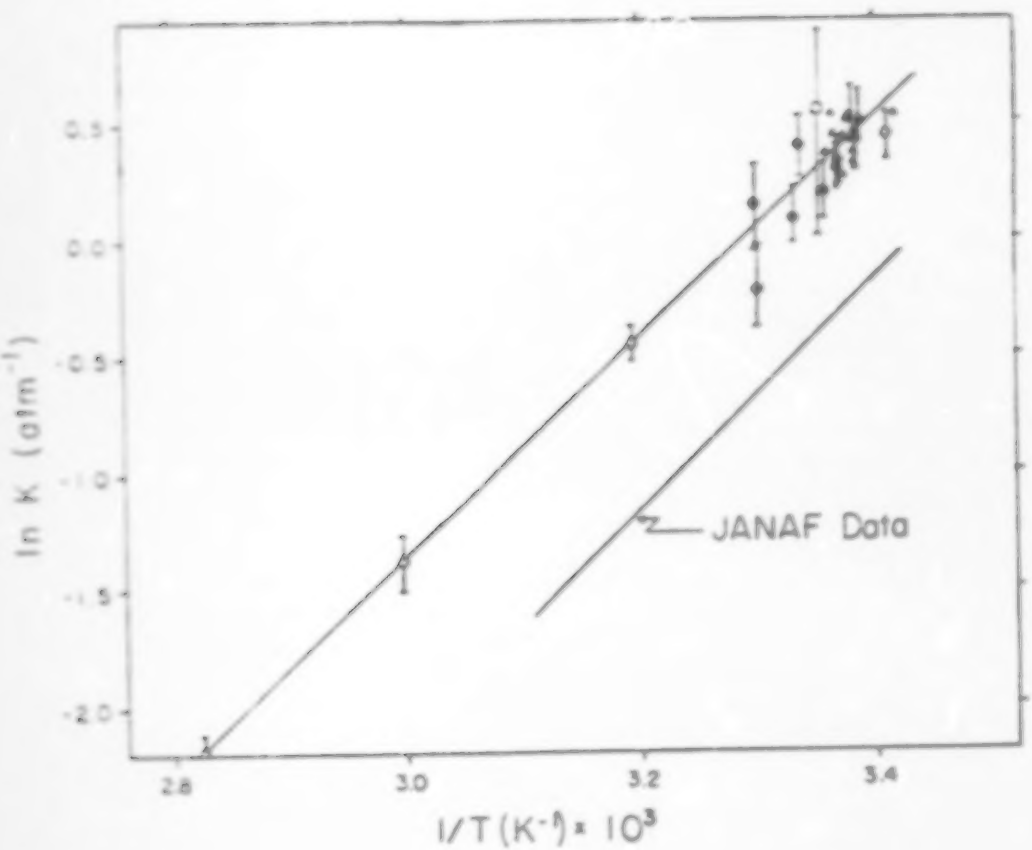


Figure 32. Plot of ln K(atm$^{-1}$) versus 1/T for literature data and present results for the equilibrium, $NO + NO_2 + H_2O \rightleftharpoons 2HONO$; open circles, Ashmore and Tyler[21]; square, average of data of Wayne and Yost[19]; triangles, Waldorf and Babb[20]; closed circles, this work. JANAF suggested values are shown along with a squares fit of published data excluding present work.

$\ln K(atm^{-1}) = -15.56 \pm 0.62 + (4.73 \pm 0.19) \times 10^3/T$ the average of the data of Wayne and Post was included only as a single point in this treatment since the scatter is greatest for this early work. From this relation we would estimate $\Delta H_{298} = 9.4 \pm 0.4$ kcal. Our present data over the very limited temperature range available to us give, $\ln K(atm^{-1}) = -15.09 \pm 3.45 + (4.59 \pm 1.03) \times 10^3/T$ and $\Delta H_{298} = 9.1 \pm 2.0$ kcal. Within the very limited accuracy of our data which extend over only a 7.8°C temperature range, the agreement of all the data is considered to be satisfactory.

The temperature drift data can be used to test, approximately, the suggested temperature dependence of the rate constants, $k_1$ and $k_2$. Here the differential Eq. (47) was employed with not only the reactant concentrations but the rate constants themselves being time dependent functions related to the temperature changes with time. For one case, shown in Fig. 31 by the dotted curve, we have tried to match well the rate of change of $P_{HONO}$ at the early times; we have taken $k_2(ppm^{-1} min^{-1}) = 3.7 \times 10^4 e^{-10(kcal/mole)/RT}$ with $k_1 = k_2 k_3$. The data appear to be qualitatively consistent with the expectations of relation 48 and $E_1 \approx 0$, $E_2 \approx 10$ kcal/mole. The temperature drift data are not good enough to attempt further refinement of values of $E_1$ and $E_2$ since the nonuniformity of the cell temperature along its length could not be avoided completely. However, we may conclude that these data are consistent with a low activation energy for reaction 1 and $E_2 \approx 10$ kcal/mole. These data gives further credence to the alternative reaction scheme 54 which supports this choice of activation energies indirectly.

e. Significance of the nitrous acid formation and decay reactions in the polluted atmosphere

The present rate data for reactions 1 and 2 provide a new basis for the evaluation of the significance of these reactions in the atmosphere. Using the present rate data we have estimated the time dependence of the HONO pressure for various levels of $NO_x$, NO, and $H_2O$ which are typical of those encountered near pollution sources and in ambient air. The results of these calculations are shown in Table 4. Note that for very high $NO_x$ levels, which correspond to those encountered near power plant stacks and automotive exhaust pipes, the rate of HONO generation is very significant. After only 10 seconds of elapsed time the $P_{HONO}$ has achieved the 1.7 ppm level for the high $NO_x$ case. Obviously dilution of the reactants occurs as the exhaust gases mix turbulently with the air, and no attempt has been made here to simulate that process. The results of Table 4 show that the generation of nitrous acid slows significantly as the $NO_x$-$H_2O$ mixture reaches ambient levels of these pollutants. Although after only five minutes of contact between reactants in a mixture of $NO_x$-$H_2O$ of composition equivalent to that of power plant stack emissions, the $P_{HONO}$ has reached 79% of its equilibrium value. However, the $NO_x$-$H_2O$ mixture at ambient levels has reached only 6% of its equilibrium levels of HONO after 60 hours. The present data

Table 4. [illegible]
for Comparative Tests of Three Gas Detectors and Ambient Conditions

| Initial Concentrations | | | | | | | | | | | | |
|---|---|---|---|---|---|---|---|---|---|---|---|---|
| $NO_2$, ppm | $SO_2$, ppm | Relative Humidity, % (25°C) | $[SO_2]/[NO_2]$ | Concentration ($cm^3/m^3$) at time shown, $cm^3$[a] | | | | | | | | |
| | | | | 1 hr | 10 hr | 20 hr | 1 day | 10 day | 1 hr | 2 hr | 20 hr | Equilibrium |
| 500 | 50 | 100 | 0.10 | 0.0574 | 0.572 | 1.70 | 14.7 | 13.4 | 24.1 | 24.1 | 24.1 | 24.1 |
| 100 | 15 | 100 | 0.15 | 0.0345 | 0.0345 | 0.103 | 1.030 | 1.30 | 7.11 | 7.11 | 7.11 | 7.11 |
| 50 | 9 | 100 | 0.18 | 0.0103 | 0.0103 | 0.0301 | 0.301 | 0.904 | 2.71 | 4.34 | 4.34 | 4.34 |
| 10 | 2 | 100 | 0.20 | $5.8 \times 10^{-4}$ | $5.8 \times 10^{-4}$ | $1.7 \times 10^{-3}$ | $2.3 \times 10^{-2}$ | $2.7 \times 10^{-2}$ | 0.240 | 0.433 | 0.962 | 0.962 |
| 5 | 1.15 | 100 | 0.23 | $1.5 \times 10^{-4}$ | $1.5 \times 10^{-4}$ | $4.3 \times 10^{-4}$ | $4.3 \times 10^{-3}$ | $7.8 \times 10^{-3}$ | $4.7 \times 10^{-2}$ | 0.243 | 0.484 | 0.484 |
| 1 | 0.25 | 100 | 0.25 | $5.8 \times 10^{-5}$ | $5.8 \times 10^{-5}$ | $1.7 \times 10^{-4}$ | $1.7 \times 10^{-3}$ | $5 \times 10^{-3}$ | $2.1 \times 10^{-2}$ | $1.7 \times 10^{-2}$ | 0.108 | 0.1083 |
| 0.5 | 0.125 | 100 | 0.25 | $2.9 \times 10^{-5}$ | $2.9 \times 10^{-5}$ | $8.3 \times 10^{-5}$ | $8.3 \times 10^{-4}$ | $2.4 \times 10^{-3}$ | $5.2 \times 10^{-3}$ | $3.4 \times 10^{-3}$ | 0.045 | 0.0539 |
| 0.1 | 0.025 | 100 | 0.25 | $5.8 \times 10^{-6}$ | $5.8 \times 10^{-6}$ | $1.7 \times 10^{-5}$ | $1.7 \times 10^{-4}$ | $5 \times 10^{-4}$ | $2.1 \times 10^{-3}$ | $1.7 \times 10^{-3}$ | $1.2 \times 10^{-2}$ | $9.7 \times 10^{-3}$ |
| 0.05 | 0.0125 | 100 | 0.25 | $1.4 \times 10^{-6}$ | $1.4 \times 10^{-6}$ | $4.1 \times 10^{-6}$ | $4.1 \times 10^{-5}$ | $1.2 \times 10^{-4}$ | $5.2 \times 10^{-4}$ | $3.1 \times 10^{-3}$ | $5.1 \times 10^{-3}$ | $4.9 \times 10^{-3}$ |
| 500 | 50 | 50 | 0.10 | 0.0287 | 0.286 | 0.774 | 7.35 | 13.3 | 22.7 | 22.7 | 22.7 | 22.7 |
| 100 | 15 | 50 | 0.15 | $1.7 \times 10^{-3}$ | $1.7 \times 10^{-3}$ | 0.0515 | 0.309 | 1.05 | 4.49 | 5.41 | 5.41 | 5.41 |
| 50 | 9 | 50 | 0.18 | $5.2 \times 10^{-4}$ | $5.2 \times 10^{-4}$ | $1.5 \times 10^{-3}$ | 0.154 | 0.87 | 1.59 | 2.90 | 2.90 | 2.90 |
| 10 | 2 | 50 | 0.20 | $2.3 \times 10^{-4}$ | $2.3 \times 10^{-4}$ | $6.9 \times 10^{-4}$ | $9.2 \times 10^{-3}$ | 0.0147 | 0.0620 | 0.408 | 0.530 | 0.530 |
| 5 | 1.15 | 50 | 0.23 | $1.5 \times 10^{-4}$ | $1.5 \times 10^{-4}$ | $4.3 \times 10^{-4}$ | $4.3 \times 10^{-3}$ | 0.0058 | 0.0435 | 0.191 | 0.341 | 0.341 |
| 1 | 0.25 | 50 | 0.25 | $2.9 \times 10^{-5}$ | $2.9 \times 10^{-5}$ | $8.3 \times 10^{-5}$ | $8.3 \times 10^{-4}$ | $2.4 \times 10^{-3}$ | 0.0103 | 0.0341 | 0.0476 | 0.0476 |
| 0.5 | 0.125 | 50 | 0.25 | $7.2 \times 10^{-5}$ | $7.2 \times 10^{-5}$ | $2.2 \times 10^{-4}$ | $2.1 \times 10^{-3}$ | $6.3 \times 10^{-3}$ | $2.4 \times 10^{-2}$ | 0.00174 | 0.0242 | 0.0242 |
| 0.1 | 0.025 | 50 | 0.25 | $2.9 \times 10^{-5}$ | $2.9 \times 10^{-5}$ | $8.3 \times 10^{-5}$ | $8.3 \times 10^{-4}$ | $2.4 \times 10^{-3}$ | $1.2 \times 10^{-2}$ | $2.8 \times 10^{-3}$ | $5.1 \times 10^{-3}$ | $5.1 \times 10^{-3}$ |
| 0.05 | 0.0125 | 50 | 0.25 | $7.2 \times 10^{-6}$ | $7.2 \times 10^{-6}$ | $2.2 \times 10^{-5}$ | $2.2 \times 10^{-4}$ | $6.3 \times 10^{-4}$ | $2.6 \times 10^{-3}$ | $1.5 \times 10^{-3}$ | $1.5 \times 10^{-3}$ | $1.5 \times 10^{-3}$ |

[a]The unit ppm used here is defined as (pressure [bars]/1.0) x $10^{-6}$.

suggest that HONO may be generated at a significant rate during the early stages of dilution of $NO_x$-rich exhaust gases, but they also point to the unimportance of reactions 1 and 2 in forming or removing HONO when ambient levels of $NO_x$ are present.

It is believed that the oxidation of about 25% of the original NO to $NO_2$ in auto exhaust gases occurs during the dilution process by reaction 54, the nearest equivalent to reaction 1 noted. Thus the significant occurrence of reaction 1 as power plant and automotive exhaust gases mix with air seems highly likely. The present data suggest that HONO vapor will be generated in the evening and the early morning hours as $NO_x$-rich exhaust gases are pumped into the air. It is reasonable to assume that HONO pressures in the early morning hours may be a significant fraction of the HONO equilibrium pressures expected from the NO, $NO_2$, $H_2O$ ambient pressures present in the morning hours. Thus it appears likely that the photolysis of HONO can provide a reasonable boost to the primary HO-radical reactant which in consort with CO and hydrocarbons drives the NO to $NO_2$ and generates the products of smog. Once this initial burst of HO-production has begun, the generation of HONO through the chain transfer reaction 46 will likely be the major source of this species and will maintain a significant level of HONO as the smog development occurs.

$$HO_2 + NO_2 \rightarrow HONO + O_2 \qquad (46)$$

In view of this work it is recommended that those atmospheric scientists concerned with the chemistry within stack plumes, include the reactions 1 and 2 in their considerations and simulations: 1 appears to be an important step in the triggering of the chemical changes which occur. The present theory appears to offer a more reasonable mechanism for HO-radical generation in power plant plumes than the sunlight photolysis of ozone:

$$O_3 + h\nu(\lambda < 3100\ \text{Å}) \rightarrow O(^1D) + O_2 \qquad (55)$$

$$O(^1D) + H_2O \rightarrow 2HO \qquad (56)$$

Ozone levels must remain quite low until considerable conversions of NO to $NO_2$ have occurred; $[O_3] = 0.02\ [NO_2]/[NO]$ ppm for a solar zenith angle of 40°. At $[NO_2]/[NO]$ ratios near unity the rates of $O(^1D)$ and HO-radical formation from the sequence 55 and 56 will be very much lower than the HO-radical formation rate from HONO photolysis.

## REFERENCES


1. R. A. McClatchey, W. S. Benedi t, S. A. Clough, D. E. Burch, R. F. Calfee, K. Fox, L. S. Rothman, and J. S. Garing, "AFCRL Atmospheric Absorption Line Parameters Compilation," AFCRL-TR-73-0096, Air Force Cambridge Research Laboratories Environmental Research Papers, No. 434 (1973).

2. J. U. White, J. Opt. Soc. Amer., 23, 285 (1942).

3. Radiation in the Atmosphere, K. Ya, Kondratzev, Academic Press, New York (1969) p. 225.

4. "Spectroscopic Methods for Air Pollution Measurement," P. L. Hanst, in Advances in Environmental Science and Technology, Vol II, J. N. Pitts and R. L. Metcalf, (Eds.) (Wiley, New York, 1971) p. 91.

5. F. H. Verhoek and F. Daniels, J. Am. Chem. Soc., 53, 1250 (1931).

6. J. C. Fontanella, A. Girard, L. Gramont, and M. Louisnard, Appl. Opt. 14, 825 (1975).

7. S. Hurlock, K. Narahari Rao, L. A. Weller, and F. K. L. Yin, J. Mol. Spectrosc. 48, 372 (1973).

8. A. J. Vosper, J. Chem. Soc. (A), 1970, 625.

9. L. Harris and K. L. Churney, J. Chem. Phys. 47, 1703 (1967).

10. M. G. Dunn, K. Wark, Jr., and J. T. Agnew, J. Chem. Phys. 37, 2445 (1962).

11. For a general review and evaluation of the potential reactions in photochemical smog formation and references to the earlier literature see: a) K. L. Demerjian, J. A Kerr, and J. G. Calvert, Adv. Environ. Sci. Technol., 4, 1 (1974); b) H. Niki, E. E. Daby, and B. Weinstock, Chapter 2 in Photochemical Smog and Ozone Reactions, F. F. Gould, (Ed.) Advances in Chemistry Series, 113, Amer. Chem. Soc., Washington, D.C., 1972, p. 16.

12. J. G. Calvert and R. D. McQuigg, Int. J. Chem. Kinet., in press.

13. L. G. Wayne and D. M Yost, J. Chem. Phys., 19, 41 (1951).

14. P. A. Leighton, Photochemistry of Air Pollution, Academic Press, N.Y., 1960.

15. R. F. Graham and B. J. Tyler, J. Chem. Soc., Faraday I, 68, 683 (1972).

16. C. England and W. H. Corcoran, Ind. Eng. Chem. Fundam., 14, 59 (1975).

17. P. L. Asquith and B. J. Tyler, Chem. Comm., 744 (1970).

18. T. Nash, Ann. Occup. Hyg., 11, 235 (1968).

19. a) R. A. Cox, J. Photochem., 3, 175 (1974); b) R. A. Cox, J. Photochem., 4, 291 (1974/75); c) D. P. Ames and R. A. Cox, Atm. Environ.,

20. D. M. Waldorf and A. L. Babb, J. Chem. Phys., 32, 432 (1963); 40, 465 (1964).

21. F. S. Ashmore and B. J. Tyler, J. Chem. Soc., (1961) 1017.

22. R. T. Hall and G. C. Pimentel, J. Chem. Phys., 38, 1889 (1963).

23. I. R. Beattie and S. W. Bell, J. Chem. Soc., (1957) 1681.

24. I. C. Hisatsune, J. Phys. Chem., 65, 2249 (1961).

25. JANAF Thermodynamic Tables, Second Edition, U. S. Dept. Commerce, N.B.S., 1971.

26. D. R. Hirschbach, H. S. Johnston, K. S. Pitzer, and R. E. Powell, J. Chem. Phys., 25, 736 (1956).

27. D. L. Baulch, D. D. Drysdale, and D. G. Horne, "High Temperature Reaction Rate Data, No. 5", Dept. Physical Chemistry, Leeds Univ., England, July, 1970, p. 42.

28. Ref. 27, p. 45.

## APPENDIX A

## OPTICAL ALIGNMENT PROCEDURE

The initial alignment of the optical system can be made by using a helium neon laser. The final adjustment involves the proper spacing of the mirrors and requires a source which gives a divergent beam and produces extended images. For preliminary adjustments, a flashlight bulb can be used but the final adjustments require a more precisely located source, S, e.g., a hole in a piece of cardboard illuminated by a light source such as a flashlight. It is assumed that such a source is used in the following discussion.

### TWENTY-ONE METER ABSORPTION CELL

The center of curvature of $M_P$ (Fig. 1) is arranged to lie between $D_1$ and $D_2$, on the line between their centers, and in the plane of $D_1$ and $D_2$. This occurs when the light reflected from $M_P$ produces an image coincident with the source, S. The center of curvature of $D_1$ and $D_2$ are arranged to lie in the plane of $M_P$ and on a horizontal line through the center of $M_P$ by placing the source at $M_P$ and examining the image formed in the plane $M_P$ after reflection by each of $D_1$ and $D_2$. The mirror $D_1$ is then rotated about a vertical axis until the first image formed on $M_P$ is immediately below the cut-out in $M_P$ (see Fig. 2). The number of images of the cell is controlled by turning $D_2$ about a vertical axis.

### SIX METER CELL

A similar alignment procedure is used for this cell. When this system is aligned the centers of curvature of the mirrors $M_a$, $M_b$, $M_c$ and $M_d$ lie at the center of the mirror system D; the center of curvature of $D_1$ falls on a horizontal line through the center of $M_c$; the centers of curvature of $D_2$ and $D_4$ lie between $M_b$ and $M_c$, and the center of curvature of $D_3$ lies in $M_b$.

### TRANSFER SYSTEM FROM THE INTERFEROMETER TO THE ABSORPTION CELL

After the cell has been aligned as described above, light from the source S is introduced into the exit window of the absorption cell and an image of the source is produced in the plane of $M_P$. The mirrors $M_8$, $M_7$, and $M_6$ in Fig. 14 are adjusted to reflect light emerging from the cell into the center of the exit window to the interferometer. The light is reflected from the beam splitter to the movable mirror $M_1$ in Fig. 13 and, by adjusting the entire interferometer, the light can be returned by $M_1$ along the incoming path. This is checked by making the

images $N_2$ (in Fig. 14), formed by the forward and returning light, coincident. When this occurs the light falling on $M_3$ is collimated and strikes $M_3$ normally.

## INTERFEROMETER AND SOURCE OPTICS

The alignment procedure described previously locates the interferometer with respect to the absorption cell and ensures that radiation leaving the movable mirror of the interferometer normally will enter the cell in the correct direction. In order to check that the source optics produces a collimated beam which strikes the movable mirror $M_3$ normally, it is necessary to remove the beam splitter and adjust $M_2$ and $M_3$ of Fig. 14 so that the light from this mirror produces an image of the source concurrent with the image already formed on $M_2$. When this is accomplished the light from $N_2$ is collimated and strikes $M_3$ normally. The beam splitter is replaced and the alignment procedure is rechecked by adjusting the beam splitter alone. The final adjustment consists of adjusting the fixed mirror of the interferometer to obtain the best interferogram.

## APPENDIX B

## FOURIER TRANSFORM SPECTROMETER

### DESCRIPTION OF OPERATION

Spectral information is obtained from the IFTS by sampling the output from the infrared detector as the mirror $M_5$ moves from a position near zero retardation through the chosen distance d. By Eq. (14) this distance depends on the desired spectral resolution which can be varied from 0.125 to 16 $cm^{-1}$. This sampling is controlled by the output from a second detector which monitors fringes produced by a helium neon laser source whose output passes through a second interferometer which includes a mirror mounted to the rear of $M_5$. The signal from the infrared detector is digitized and stored in the memory of the processing system. By co-adding signals obtained from several scans of $M_5$ the signal-to-noise ratio can be enhanced. Most of the spectra described in this report were obtained from 20 scans of $M_5$.

The data collection is performed under the control of an on-line minicomputer (Nova 1200) which receives instructions via a teletype machine. A 128k fixed head disc not only provides temporary data storage but also provides storage for the Fourier transform programs. The stored interferogram can be transferred to magnetic tape for permanent storage or processed by means of the computer program to give a spectrum. Either all or selected portions of this spectrum can be displayed on a digital plotter or stored on magnetic tape. Additional interferograms may then be obtained and processed. Other programs, stored in the disc memory unit, allow further manipulation of the spectra. One of the most commonly used programs allows two spectra to be "ratioed". In this program the output signal of one spectrum is divided by the signal from the second spectrum at each spectral frequency sampled. For example, by ratioing the spectrum of a gas sample in the absorption cell with a similar spectrum of the evacuated cell a direct measurement of the gas sample transmittance is obtained with the spectral variations of the detector sensitivity, source emittance, and optical system transmittance removed.

### UNDERSAMPLING TO OBTAIN HIGH RESOLUTION

The interferogram is obtained by sampling the output from the infrared detector as the mirror $M_5$ moves through a distance d. This distance is determined by the required spectral resolution $\Delta\nu$ where

$$\Delta\nu\ (cm^{-1}) = 1/2d\ (cm) = 1/x \qquad (57)$$

The infrared detector output is sampled at mirror positions separated by a distance $\Delta x$. This distance is controlled by the reference laser interferometer and is given by

$$\Delta x = m\lambda_L = m/\nu_L \tag{58}$$

where $\nu_L$ = 15,800 $cm^{-1}$ and $\lambda_L$ = 0.633 $\mu m$ are the laser wavenumber and wavelength, respectively, and m is an integer.

The number of sample points in the interferogram

$$n = x/\Delta x = \nu_L/m\Delta\nu \tag{59}$$

Thus, if m = 1 and $\Delta\nu$ = 0.125 $cm^{-1}$, n = 126,400. This is considerably larger than the maximum number of points, 32,000, which can be transformed into a spectrum with the IFTS system available.

It is, however, possible to collect interferograms with n < 32,000 from which spectra with a resolution of 0.125 $cm^{-1}$ can be obtained provided m > 1. This process, known as undersampling, cannot provide useful information unless the signal from the infrared detector is limited to information in the spectral interval

$$\delta\nu = \nu_{max} - \nu_{min} \tag{60}$$

Upper and lower bounds to the spectral interval sampled are required since, when an interferogram consisting of information sampled at discrete points is transformed the resulting spectrum is repeated at intervals $\delta\nu$ such that

$$\delta\nu = 1/2\Delta x \tag{61}$$

where $\Delta x$ = sampling interval of the interferogram.

If either $\delta\nu$ or $\Delta x$ is improperly chosen, information from more than one spectral region can be superposed in the resulting spectrum obtained from the interferogram; this effect is known as folding.

From Eqs. (57), (58), and (61) it follows that

$$n = \frac{2\delta\nu}{\Delta\nu} \tag{62}$$

and, hence, for the present IFTS system

$$\frac{\delta\nu}{\Delta\nu} = 15798.0112 \tag{63}$$

The entire spectral region from 0 to 8000 $cm^{-1}$ (the high frequency cutoff of the germanium beam splitter) can be observed provided $\Delta\nu \geq 0.5\ cm^{-1}$. However, to obtain a spectrum with $\Delta\nu$ = 0.125 $cm^{-1}$ then

$$\delta\nu \leq 1974.7514\ cm^{-1} \tag{64}$$

and, since in this case the interferogram must be sampled over the entire 4 cm range of the mirror travel it follows from Eq. (59) that

$$m \geq 4 .$$

It is possible to select the spectral region over which high spectral resolution is obtained and, at the same time, avoid folding by choosing $\nu_{max}$ and $\nu_{min}$, as defined by Eq. (60), such that

$$\begin{aligned} \nu &= h \delta\nu \\ &= h (\nu_{max} - \nu_{min}) \end{aligned} \tag{65}$$

where h is an integer.

The limiting values of $\nu_{max}$ and $\nu_{min}$ depend on the values chosen for m, h, and $\Delta\nu$. A sampling of these limits is given in Table 5 for an instrument using a helium neon laser to control the sampling interval $\Delta x$ and for the case where $\Delta\nu = 0.125$ cm$^{-1}$. The first three columns give the undersampling parameter m, the sampling interval $\Delta x = m\lambda_L$, and the number of points in the interferogram at which data are collected, respectively. The succeeding columns give the values of $\nu_{min}$ and $\nu_{max}$ for different values of h.

It is seen that, $m \geq 4$ for $n < 32{,}000$.

In order to make use of this instrument capability we have obtained three optical filters whose characteristics are shown in Table 6. Although the transmittances of the filters are not completely matched to the IFTS system it is possible to cover almost the entire spectral region from 400 to 3800 cm$^{-1}$ by obtaining no more than three interferograms. The number of interferograms required could be reduced by increasing the memory capability of the IFTS system to allow the value of n to exceed 32,000.